



POLITECNICO
MILANO 1863

School of Industrial and Information Engineering

Master Degree in Mechanical Engineering

**Design and control of a biomimetic
robot inspired to the manta ray**

Supervisor: Prof. Simone Cinquemani

Emilio D'Andretta 896598

Roberto Cilio 905779

Academic Year 2019/2020

Ringraziamenti

A conclusione di questo percorso, sento di dover porre i miei più sentiti ringraziamenti. Tuttavia, risulta difficile riuscire a ricordare in poche righe, tutti coloro che, a vario titolo, hanno contribuito a rendere questo giorno speciale.

Innanzitutto un ringraziamento sentito va al prof. Simone Cinquemani per la guida competente e solerte e per la grande disponibilità e pazienza mostrata durante il percorso di tesi.

All'ing. Giovanni Bianchi un immenso grazie per il supporto costante, le dritte indispensabili e la sua complicità nella realizzazione della ricerca.

Grazie ancora a Roberto Cilio, amico e compagno di avventura con cui ho avuto il piacere di lavorare fianco a fianco nel raggiungimento di questo piccolo traguardo.

Un ringraziamento speciale va ai miei genitori ed alla mia famiglia, perchè se son arrivato fin qui lo devo anche al loro continuo sostegno e vorrei che questo giorno fosse un premio per loro per la fiducia riposta in me ogni giorno.

Non possono poi mancare da questo elenco i miei colleghi, con cui ho iniziato e trascorso i miei studi avendo la fortuna di condividere momenti indimenticabili e i miei amici tutti che sono sempre al mio fianco in ogni istante della mia vita. Infine un ringraziamento a mio fratello, la stella più bella, che ogni giorno mi indica il percorso più giusto da seguire, ecco, se oggi fosse qui al mio fianco sono sicuro che sarebbe ancora più orgoglioso di me.

Abstract

Nowadays the interest in autonomous underwater vehicles is in constant increase following the emerging needs of underwater mining and fish farming. Batoid fishes produce thrust with their pectoral fins, they essentially produce a wave travelling in the direction opposite to their motion, pushing water backwards and gaining thrust as a consequence of momentum conservation. The aim of this research was to design and control a bio-inspired robot that exploits the swimming efficiency of a Myliobatiformes species that move by oscillating the pectoral fins. For the realization of the robot, inspiration was taken from a cow-nosed ray, and from the study of the biological system, the robotic one was obtained through optimization processes. From the interaction of 3D analysis programs such as Simulink and CFD, fundamental data was extracted. It was created a 3D environment capable of describing underwater interactions, helpful for the size of electrical parts: hardware, motors, external power supply and joystick. Finally, various control logics and filtering techniques have been implemented using Arduino code, in order to obtain a straight swimming motion and a high maneuverability in the turns. Main bionic characteristics extracted from the cow-nosed ray are fulfilled by the prototype and verified by experiments.

Contents

1	Introduction	3
1.1	Bio-Inspired Autonomous Underwater Vehicles	3
1.2	Classification Of Bio-Inspired Aquatic Systems	6
2	Hydrodynamics Of Fish Swimming	10
2.1	Fish Swimming Modes	14
2.2	MPF Propulsion	17
2.3	BCF propulsion	20
2.4	Undulation vs Oscillation	21
2.5	Power Requirements And Efficiency	23
3	Manta Ray Hydrodynamics	31
3.1	Biology	32
3.2	Body Structure Analysis	33
3.3	Turning Maneuvers	38
4	Mechanism Synthesis and Design	40
4.1	Shape And Coating	41
4.2	Pectoral Fin Kinematics	44
4.3	Tail	56
5	3D Analysis Of Manta Robot	58
5.1	Multibody	58
5.2	CFD	71
5.3	Results	75

6	Motors and Electrical Circuit	79
6.1	Servo Motors	80
6.2	Arduino	84
6.3	Power Supply and Breadboard	86
6.4	Joystick	88
7	Motion Control	90
7.1	Introduction	90
7.2	Filtering	91
7.3	Sinusoidal wave and Calibration	95
7.4	Type of motion	97
7.5	Control Logic	100
7.6	Testing	106
8	Conclusion	110

Chapter 1

Introduction

1.1 Bio-Inspired Autonomous Underwater Vehicles

In recent years, with the progress of bionics, robotics, mechanics, new materials science, automatic control theory and other disciplines, as well as the increased development of marine economy and military demands, there is a growing need for the adaptation of robotic systems which can autonomously perform routine tasks in aquatic environments.[Leonard et al., 1998] This need derives from the large scale unobservable volume of the oceans and other bodies of water which all present a challenge for human observation. This challenge persists due to human fragility in aqueous environments and to the underdeveloped robotic systems that are deployed [Murphy and Haroutunian, 2011]. Specifically, steady-state hydrodynamics, on which submarines and aircraft are designed, do not explain the hovering or rapid turning of coral reef fish or the high lift of fruit flies[Smallwood and Whitcomb, 2004].

In animal swimming and flying, unsteady hydrodynamics is the norm. An aquatic animal could be considered the perfect autonomous undersea platform that is optimized for a specific habitat, which is the business of survival and procreation in a certain environment. Thus, feasibility of the full system is not in doubt. The issue is bridging the gap in science and technology between nature and engineering in specific disciplines. Animal systems tend to be very robust in a range of environments; they are adaptive, closed-loop systems with redundancy; autonomous, and optimized for their environment. To solve the lack of mission capabilities of these systems, inspiration must be taken from the diverse

selection of species which inhabit the oceans, rivers, and lakes. There have already been studies where researchers used bio-inspiration and bio-mimicry to make aquatic robots, which fall in the category of aquatic unmanned vehicle (AUV). In this introduction it is presented a brief classification for biological and AUV systems. AUVs have application in a wide range of civilian and military missions for exploitation in marine or aquatic environments. These missions include environmental surveying, oil spill monitoring, internal pipe inspection, erosion monitoring, observation of animal species, beach safety, espionage, anti-espionage, and border patrol. [Blidberg, 2001] The mission of an AUV is dependent on its design and more prominently on the autonomy of the system. Fully autonomous system is necessary for the completion of many of these missions because signal transmission through water is difficult, especially at great depths or distances[Wynn et al., 2014]. The craft needs to carry out preplanned mission solely on its own and should respond to changing environment. In addition, these systems need to have long endurance and have the capability to move in close quarter environments with constantly changing fluid flow. A close quarter environment would not condone a system tethered with a control cable or that of those using propellers[Bradley et al., 2001]. Propeller thrust degrades when fluid flow is not uniform. Propellers are also inefficient in comparison with fishes where propellers are estimated efficiency of 40–50 %. In order to take inspiration from animals, a comparison between some key performance parameters such as speed, manoeuvrability, efficiency/economy and stealth, is needed:[Du et al., 2015]

- **Speed:** The highest swimming speeds in animals have been discovered for the oscillatory lift-based propellers. Swordfish and marlin can achieve the largest maximum speed of of 130 km/h for a short time intervals. This speed results faster than for fully submerged vessels, except for super-cavitation vessels. Whales and dolphins are able to cruise at speed range 40-63 km/h.
- **Manoeuvrability:** The conventional propulsive technologies use control surfaces, for instance rudders, fins, dive planes, to manoeuvre. In addition, lateral thruster and vectored thrust mechanism can produce turns, such as water jet, outboard motors. In nature, several marine species use similar mechanisms by means of a combination fo fins and vectored thrust. For instance, complex manipulation of

individual fin rays or movement or enlarged pectoral fins which act as propulsor and guarantee effective manoeuvrability in tight environments.

- **Efficiency:** Different studies show a Froude efficiency of the propeller lower than 0.7. The propeller efficiency is dependent on the kinetic energy losses due to the rotation rate and swirl induced to the fluid. Moreover, the friction drag on blades, tip leakage, rotational flow and propeller-induced axial swirl flow play important roles. Whereas, the thrust performance of fish propulsive system has been considered superior to screw propeller, e.g. body and caudal fin propulsor efficiencies range from 0.7 to 0.9.
- **Stealth:** Propulsive systems move bodies, which cause the propagation of waves through the water to create hydrodynamic sound. Much of the anthropogenic noise in the marine environment is the result of ship traffic, which is mainly produced by screw propellers. While, the hydrodynamic sounds of swimming fish are generally low frequency, and can be detected over a short range when produced at high intensity.

In conclusion, the use of bio-inspired propulsive system will probably never replace the general use of screw propeller, due to the ubiquity of this technology. However, bio-inspiration and bio-mimicry can be used in more specialized applications, which are strictly dependent on a defined application and mission. [Low, 2011] For example, systems comparable with the eel would be useful in pipe inspection where large body contortion is necessary to navigate complex bends. Furthermore, tuna are extremely efficient swimmers: such, a robot that has a high level of biomimicry could also display high speed required for specific missions.



In this thesis, the aim of a robotic fish design is to mimic nature, in order to figure out, for instance, the fluid-mechanical principles which allow an efficient, manoeuvrable, silent, fast swimming.

1.2 Classification Of Bio-Inspired Aquatic Systems

To date many bio-inspired AUVs have been developed using the skills of biological systems to overcome engineering problems. A first general classification of bio-inspired systems is based on the used materials. Generally, there are two different types of materials used to accomplish movement. These materials are either rigid or soft, where rigid means the components do not deform or change shape. Rigid materials have the benefit of using actuation mechanisms commonly found in robotics. Soft materials can flex and deform during movement. Soft materials have the benefit using newer and more experimental actuation mechanisms. Some mechanical systems have skins which are applied over the actuation mechanism to improve hydrodynamics.

Another classification, widely used, is defined by the same class of biological systems. In the following tables some examples of bio inspired robots [Salazar et al., 2018a]:

Table 1.1: Anguilliform bio-inspired systems

Anguilliform	Description	Author
Lamprey Robot 	Rigid head unit contains electronic components./ Five actuators in series gives a large body undulation./ Tail equipped with buoyancy foam.	[Ayers et al.,]
Mamba Waterproof Snake Robot 	Small overlapping modules, one type allows overlapping chain./ Each segment has on actuator./ Modules are waterproof.	[Liljebäck et al., 2014]

Amphibious Snake-like Robot



Larger tubular segment [Yu et al., 2009] modules./ Each segment has two actuators to realize 3D motion./ This system can make complex motions.

Table 1.2: Carangiform bio-inspired systems

Carangiform	Description	Author
<p>G9 Fish</p>	<p>Three-link-motor actuation mechanism./ On board sensors./ Large scales covering over tail section attached to body./ Fins are flexible.</p>	<p>[Hu et al., 2006]</p>
<p>Carp Robot</p>	<p>Mimics the Carp shape./ Onboard sensors housed in a component acrylic enclosure./ Flexible tail and pectoral fins./ Pectoral fins can rotate 180 deg.</p>	<p>[[Majeed and Ali, 2016]]</p>
<p>Hydraulic Soft Robotic Fish</p>	<p>Hydraulic peduncle actuation, soft peduncle and tail design./ Functioning control surfaces./ Rigid body./</p>	<p>[Katzschmann et al., 2016]</p>

Table 1.3: Thunniform bio-inspired systems

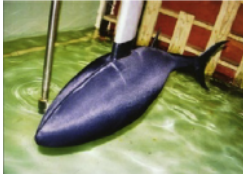

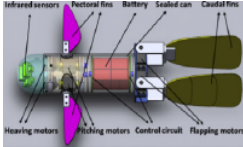

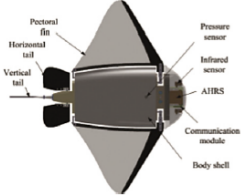
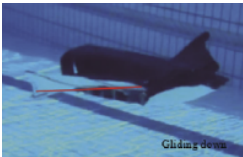
Thunniform	Description	Author
<p data-bbox="379 412 612 445">MIT RoboTuna</p> 	<p data-bbox="807 483 1187 913">A test platform in which a multi-part pulley gives actuation for tuna movement./ The RoboTuna was fixed within a water channel./ One of the first to test this kind of movement to study hydrodynamic effects</p>	<p data-bbox="1219 483 1414 517">[Tolkoff, 1999]</p>
<p data-bbox="304 943 679 976">Multi-link Robotic Dolphin</p> 	<p data-bbox="807 999 1187 1323">Multi-link design./ Movement restricted to last quarter of the body./ Pectoral fin control surfaces have 3 DOF./ Rigid main body./ Flexible body shell.</p>	<p data-bbox="1219 999 1437 1032">[Fei et al., 2011]</p>
<p data-bbox="209 1346 775 1379">Pectoral Fin and Dual Caudal Fin Robot</p> 	<p data-bbox="807 1406 1187 1731">This design uses pectoral fins for stability and thrust./ Dual caudal fins increase yaw stability (mimics Jet Propulsion)./ Waterproof rigid body</p>	<p data-bbox="1219 1406 1485 1440">[Zhang et al., 2016]</p>

Table 1.4: Mobuliform bio-inspired systems

Mobuliform	Description	Author
<p>Manta Ray Robot</p> 	<p>Larger body./ Does not have control alternative control surfaces./ Has the same rigid leading edge and support rib for the flexible fin membrane</p>	<p>[Gao et al., 2007]</p>
<p>Robo-Ray III</p> 	<p>Third generation system design./ Thinner body equipped with control flaps for stability and depth control./ Rigid leading edge of fin, along with a single support rib along length of body. / Membrane of the fin is flexible silicon rubber.</p>	<p>[Niu et al., 2012]</p>
<p>RoMan-III</p> 	<p>Multiple fin ribs give actuation to a flexible./ membrane./ Body is rigid with the action motors along the side of the body./ System can perform null speed pivot turning.</p>	<p>[Low et al., 2011]</p>

Chapter 2

Hydrodynamics Of Fish Swimming

In order to better analyze the properties and principles that aquatic bio-inspired robots must exploit for higher efficiency, the biological system is analyzed.

Incompressibility and high density are the main properties of water, as a locomotion medium, that have played an important role in the evolution of fish. Since water is an incompressible fluid, any movement performed by a fish moves the water around it and vice versa. The density of the body of marine animals is sufficiently close to that of water so that gravity and Archimede's thrust are nearly counterbalanced. This has allowed the development of a great variety of swimming propulsors, as weight support is not of primary importance. [McKenzie et al., 2007a] For the treatment of fish swimming mechanisms,

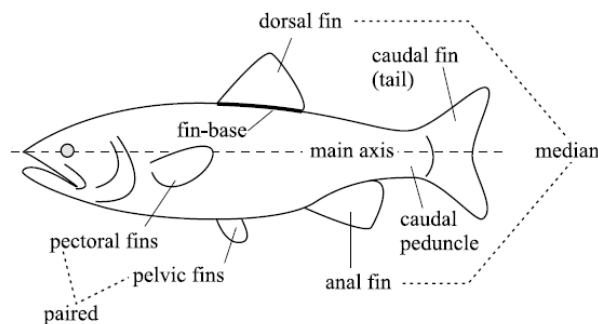


Figure 2.1: Terminology used in the text to identify the fins and other features of fish

fig. 2.1 shows the terminologies used in this research to identify morphological features of fish. [McKenzie et al., 2007b]. Median and paired fins can also be characterized as either short-based or long-based, depending on the length of their fin base relative to the overall fish length. The fin dimensions normal and parallel to the water flow are called

span and chord respectively. Swimming is a consequence of the transfer of momentum between the fish and the surrounding water (and vice versa). The main mechanisms by which the transfer of momentum takes place are via drag, lift and acceleration reaction forces. Swimming drag consists of the following components:

- skin friction between the fish and the boundary layer of water (viscous or friction drag). Friction drag arises as a result of the viscosity of water in areas of flow with large velocity gradients. Friction drag depends on the wetted area and swimming speed of the fish, as well as the nature of the boundary layer flow. [Anderson et al., 2001]
- pressure formed in pushing water aside for the fish to pass (form drag). Form drag is caused by the distortion of flow around solid bodies and depends on their shape. Most of the fast-cruising fish have well streamlined bodies to significantly reduce form drag; [Barrett et al., 1999]
- energy loss in the vortices formed by the caudal and pectoral fins as they generate lift or thrust (vortex or induced drag). Induced drag depends largely on the shape of these fins. The latter two components are jointly described as pressure drag. [Drucker and Lauder, 1999]

The latter two components are jointly described as pressure drag. Also lift forces originate from water viscosity like pressure drag, and they are caused by asymmetries in the flow. As fluid moves past an object, the pattern of the flow may be such that the pressure on one lateral side is greater than that on the opposite. Lift is then exerted on the object in a direction perpendicular to the flow direction. Acceleration reaction is an inertial force, generated by the resistance of the water surrounding a body or an appendage when the velocity of the latter relative to the water is changing. [Vogel, 1994] Inertial forces reaction is more sensitive to size than is lift or drag velocity. [Daniel, 1984] [Webb, 1988a] A swimming fish is subject to different forces such as: weight, buoyancy and hydrodynamic lift in the vertical direction and thrust and resistance in the horizontal direction(Fig 2.2). The hydrodynamic stability and direction of movement are often considered in

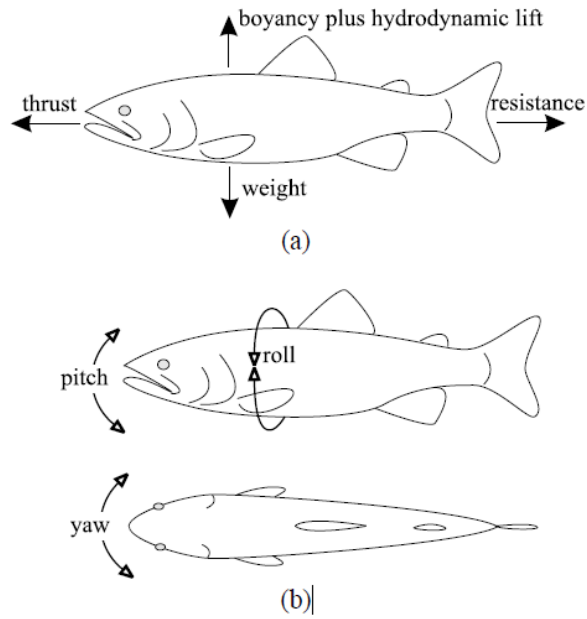


Figure 2.2: (a) The forces acting on a swimming fish. (b) Pitch, yaw and roll definitions.??

terms of pitch and roll. The swimming speed of fish is often measured in body lengths per second (BL/s). For a fish that swims with constant speed the momentum conservation principle requires that the total thrust it exerts against the water must equal the total resistance it encounters moving forward. Pressure drag, lift and acceleration reaction can all contribute to both thrust and resistance. However, since lift generation is associated with the intentional movement of propulsors by fish, it only contributes to resistance for actions such as braking and stabilization rather than for steady swimming. The most important factors determining the relative contributions of the momentum transfer mechanisms to thrust and resistance are **(i)** Reynolds number, **(ii)** reduced frequency and **(iii)** shape. [Sfakiotakis et al., 1999]

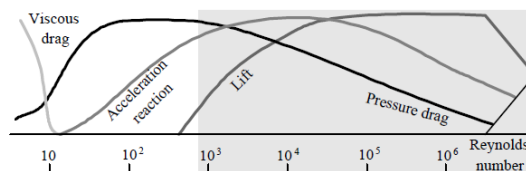


Figure 2.3: Diagram showing the relative contribution of the momentum transfer mechanisms for swimming vertebrates, as a function of Re . The shaded area corresponds to the range of adult fish swimming. [Webb, 1988b]

Reynolds number: it is an important dimensionless quantity used to predict the flow patterns: at low Reynolds number the laminar flow tends to dominate, whereas at high Reynolds number turbulence occurs, resulting from differences in fluid's speed and direction. In laminar flow the viscous forces are dominant: the flow is characterized by smooth and constant fluid motion. In turbulent flow the inertial forces dominate: chaotic eddies, vortices and other instabilities occur. Therefore, to determine the relative importance of viscous and inertial forces on the swimming of the fish, it is possible to determine the Reynolds number of the flow. Obviously the size and the swimming speed of the animal affect the Reynolds number, thus the relative importance of the viscous and inertial forces. The Reynolds number (Re) is defined as:

$$Re = \frac{LU}{v} \quad (2.1)$$

where L is a characteristic length (of either the fish body or the propulsor), U is the swimming velocity and v is the kinematic viscosity of water. In the realm of Re typical of adult fish swimming (i.e. $10^3 < Re < 5 \cdot 10^6$) inertial forces are dominant and viscous forces are usually neglected. At those Re acceleration reaction, pressure drag and lift mechanisms can all generate effective forces. [Webb, 1988b]

Reduced frequency: it points out the relevance of the unsteady effects in the flow. Pressure drag and lift are dominant in the force balance only for steady movements of the animal. Therefore, if the movements are highly time-dependent, drag and lift can be reduced: accelerations become large, and the magnitude of the acceleration reaction increases. The relative importance of the acceleration reaction compared to pressure drag and lift is pointed out by the reduced frequency which makes a comparison between the time necessary for a particle of water to traverse the length of an object with the time taken to complete one total movement cycle. It is defined as:

$$\sigma = 2\pi \frac{fL}{U} \quad (2.2)$$

where f is the oscillation frequency, L is the characteristic length and U is the swimming velocity. The reduced frequency essentially compares the time taken for a particle of water to traverse the length of an object with the time taken to complete one movement

cycle. It is used as a measure of the relative importance of acceleration reaction to pressure drag and lift forces. For $\sigma < 0.1$ the movements considered are reasonably steady and acceleration reaction forces have little effect. For $0.1 < \sigma < 0.4$ all three mechanisms of force generation are important, while for larger values of σ acceleration reaction dominates. In practice, for the great majority of swimming propulsors, the reduced frequency rarely falls below the 0.1 threshold [Webb, 1988b]. Another commonly employed non-dimensional quantity to measure the frequency for periodic flows is Strouhal number St , which is defined as:

$$St = \frac{fH}{U} \quad (2.3)$$

Finally, the **shape** of the swimming fish and the specific propulsor utilized largely affects the magnitude of the force components.

2.1 Fish Swimming Modes

Fish have different types of movements; first major distinction is between swimming or nonswimming and the second one includes specialized actions such as jumping, burrowing, flying and gliding, as well as jet propulsion. Another important distinction about swimming locomotion can be made according to the temporal features in: [Webb and Weihs, 1983]

- Periodic (or steady or sustained) swimming, characterized by a cyclic repetition of the propulsive movements. Periodic swimming is employed by fish to cover relatively large distances at a more or less constant speed.
- Transient (or unsteady) movements, that include rapid starts, escape manoeuvres and turns. Transient movements last milliseconds and are typically used for catching prey or predator avoidance.

Periodic swimming has undoubtedly captured the scientific attention of biologists and mathematicians, as the transient ones are very complex and difficult to repeat and verify. Therefore, periodic swimming will inevitably be the main focus of this research. However, given the significant aspects of locomotion associated with transient movements, which provide fish with unique abilities in the aquatic environment and the more recent interest

among scientists in describing them, reference will also be made to transient propulsion, where possible.

A classification widely used to diversify the motion of fish is proposed [Webb, 1994], relating the swimming propulsors, kinematics, locomotor behaviour and muscle fibre used to the notion of swimming gaits.

A part of fish produces thrust by bending their bodies into a backward-moving propulsive wave that extends to its caudal fin, a type of swimming classified under Body and/or Caudal Fin (BCF) locomotion. Other fish have developed alternative swimming mechanisms, that involve the use of their median and pectoral fins, termed Median and/or Paired Fin (MPF) locomotion. Although the term paired refers to both the pectoral and the pelvic fins, the latter (despite providing versatility for stabilization and steering purposes) rarely contribute to forward propulsion and no particular locomotion mode is associated with them. An estimated 15% of the fish families use non-BCF modes as their routine propulsive means, while a much greater number that typically rely on BCF modes for propulsion employ MPF modes for manoeuvring and stabilization. [Videler, 1993] A further distinction, fundamental for this research, made for both BCF and MPF propulsion, is on the basis of the movement characteristics. Undulatory motions involve the passage of a wave along the propulsive structure, while in oscillatory motions the propulsive structure swivels on its base without exhibiting a wave formation. The two types of motion are considered to be connected to each other since the passage from one motion to another is linked to the undulation wavelength. Furthermore, both types of motion result from the coupled oscillations of smaller elements that constitute the propulsor (i.e. muscle segments and fin rays). Generally, fish that routinely use the same propulsion method display similar morphology but form differences do exist and these relate to the specific mode of life of each species. [Webb, 1984] identified three basic optimum designs for fish morphology, derived from specialisations for accelerating, cruising and manoeuvring. Also, since they are largely mutually exclusive, no single fish exhibits an optimal performance in all three functions. But neither are all fish specialists in a single activity; they are rather locomotor generalists combining design elements from all three specialists in a varying degree.[Webb, 1984] Fish can also present different swimming locomotion at the same time, for example: median and paired fins are routinely used in conjunction to

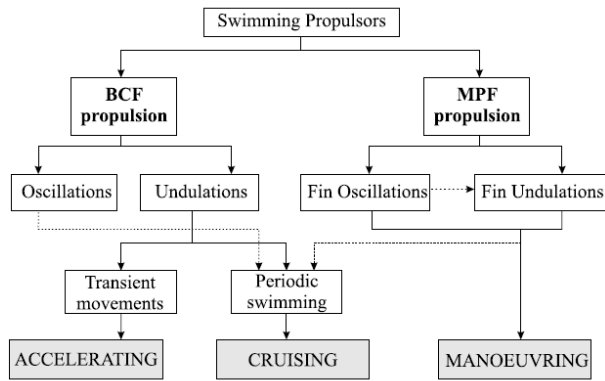


Figure 2.4: Diagram showing the relation between swimming propulsors and swimming functions [Webb, 1984].

provide thrust with varying contributions from each, achieving very smooth trajectories; many fish typically utilise MPF modes for foraging, as these offer greater manoeuvrability, switching to BCF modes at higher speeds and for high acceleration rates. All kinds of

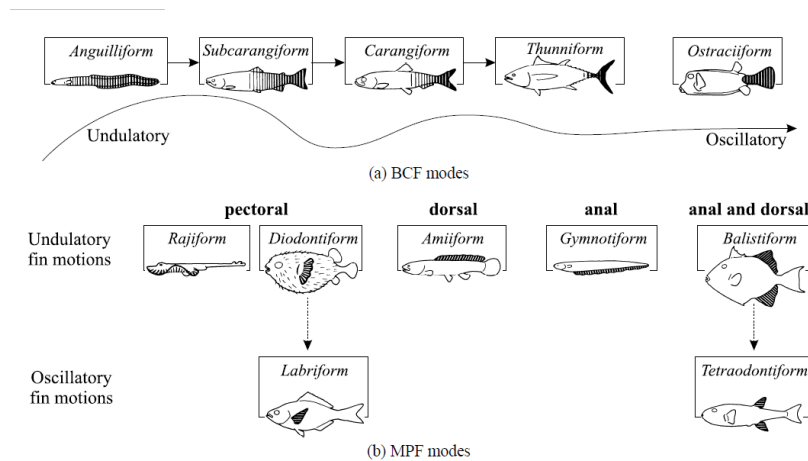


Figure 2.5: Swimming modes associated with (a) BCF propulsion and (b) MPF propulsion. Shaded areas contribute to thrust generation.

swimming mechanisms are brought together by generation of a series of vortices into their wakes that impart momentum and impulse to the fluid environment causing an equal and opposite force to drive the animal forward. In the case of pulsatile jet production, individual vortex rings are ejected in the downstream direction, which can be seen to produce a jet structure through the centre of the rings. For BCF and MPF swimmers, typically a series of connected vortex rings or pairs of laterally ejected vortex rings are shed into the wake [Lauder and Madden, 2007]. The series of connected vortex rings is seen to be a three dimensional analogue to a reverse von Kármán street also known as

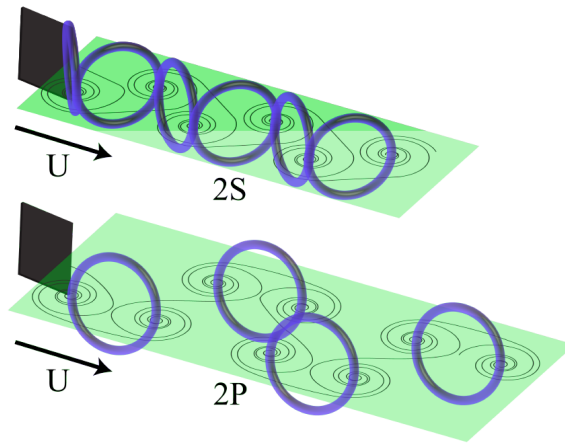


Figure 2.6: Typical three-dimensional vortex wake structures produced by swimming animals. The top is a reverse von Kármán street otherwise known as a 2S wake, where two single vortices are shed per cycle. The bottom is a 2P wake where two pairs of vortices are shed per cycle

a 2S wake structure where two single vortices are shed per oscillation cycle. Von Kármán street is responsible for the unsteady separation of flow of a fluid around blunt bodies. As can be seen in fig.2.7 Kármán vortex street is a repeating pattern of swirling vortices,



Figure 2.7: Von Kármán street

caused by a process known as vortex shedding that will form only at a certain range of flow velocities, specified by a range of Reynolds numbers

2.2 MPF Propulsion

Undulating fins are used by a lot of fishes as auxiliary propellers, as well as for motion stabilization and maneuvering. Although, median and paired fins can be employed as sole thrust source for generally slow cruising ($< 3 \text{ BL/s}$). Generally, the species of the teleostei

infraclass, the ray-finned fishes, adopt median-paired fin locomotion mode. The fins of teleost fish consist of the fin-rays which have varying span and stiffness and a flexible membrane connecting them together. This specie use individual rib excitation in their fins to create undulatory waves along the fins. [Sfakiotakis et al., 1999] Wave propagation is employed for thrust and stability control. Some of these animals are able to control the direction of the wave, giving them forward and backward swimming capabilities or null speed turns. Fins with ribs to perform undulation vary depending on the kind of the fin and also on the type of animal. Generally, the ribs allow great control of their fins. The characteristics of the teleost fins is reviewed by [Lindsey, 1978]; [Videler, 1993]. High endurance swimmers can be found in this category, but usually these species are ambush predators, hence not burst swimmer, but good maneuverability, multi-directional motion to navigate in close-quarter environments ([Albert, 2001a]; [Sfakiotakis et al., 1999]). It is possible to distinguish different classes:

- *Rajiform* the thrust generation involves the passing of the vertical undulations along the pectoral fins that are large, triangular-shaped and flexible. The amplitude of undulations increases from the anterior part to the fin tip and then tapers again towards the rear. The fins show also a flapping discipline. This mode is employed by rays, skates and mantas, whose swimming mimic the flight of birds. The fin ribs extend from the body into the pectoral fins. The ribs are excited by muscles with run through the skeleton, which can be individually controlled to create an undulatory wave along the chord of the fin. The body of these swimmers are flexible because of the presence of a cartilaginous structure, even though it is not strong as bone, the bodies are still strong.
- *Diodontiform* the propulsion is achieved by passing undulations through the broad pectoral fins. Up to two full wavelengths may be visible across the fins, while undulations are often combined with flapping oscillating motions of dorsal and anal fins for thrust generation at higher speeds. These swimmers are not migratory, they swim into shallow water reefs.
- *Amiiform* swimming is by undulations of a long-based dorsal fin, while body axis is in many cases held straight when swimming. The anal and caudal fins are missing,

while the dorsal fin extends along most of the body length and exhibits a large number of fin-rays. These swimmers are not particularly fast, a decent agility is exhibited. They are able to perform tight turning and multi-directional locomotion.

- *Gymnotiform* is considered the upside-down equivalent of amiiform mode, since propulsion is reached by undulations of long-based anal fin. The dorsal fin is not present. Thanks to many individual ribs they have the complete control of the fin on the entire length because each rib has its own set of agonist and antagonist muscles. They are not migratory swimmers, due to the small body and the vulnerability to larger predators outside hunting zones.
- *Balistiform* both the anal and dorsal fins undulate to generated the propulsion forces. The median fins are usually inclined relative to each others, while the body is usually flat and compressed laterally. The caudal fin is used to enhance endurance. These swimmers are not migratory, they swim in shallow reefs.

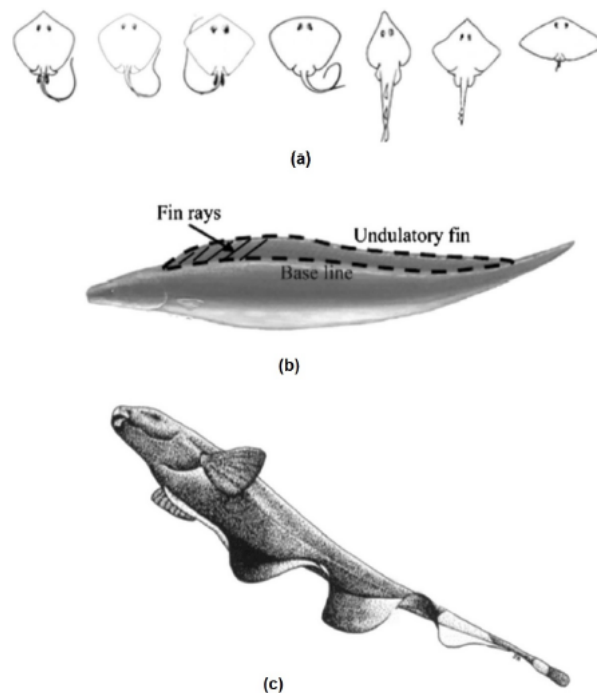


Figure 2.8: (a) Different body shapes of different species with Rajiform locomotion, from left to right: Common Stingray, Skates, Manta Cownose Ray ([Rosenberger, 2001a]); (b) Schematic of Amiiform and the fin rays along a dorsal undulatory fin [Salazar et al., 2018b]); (c) Drawing of Gymnotiform with the undulating anal fin (Ghost Knifefish) ([Albert, 2001b]).

2.3 BCF propulsion

The undulatory BCF mode is characterized by a transmission of wave through the fish body in a direction which is opposite to the forward swimming direction. The speed of the wave must be greater than the cruising speed. The differences among the locomotion modes are related to the amplitude and wavelength of the traveling wave, but also in the thrust generation mechanism. Two thrust generation mechanisms have been recognized: the added-mass method and a lift-based (vorticity) method. The added mass method is mainly employed by *anguilliform*, *subcarangiform*, *carangiform* modes. While the vorticity method is mainly used by *thunniform* mode. The BCF undulatory thrust-generation

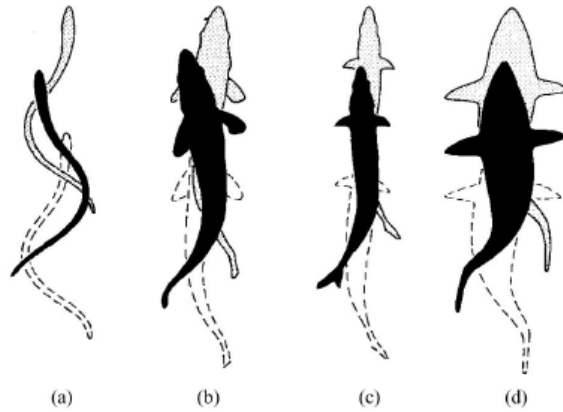


Figure 2.9: Visual diagrams to depict the body motion undulation to realize a tail oscillation. (a) Anguilliform, (b) Subcarangiform, (c) Carangiform, and (d) Thunniform (Lindsey, 1978).

mechanism can be further classified in four swimming modes adopting the terminology and the taxonomy explained by [Breder, 1926]. The Figure 2.9 depicts the four undulatory BCF locomotion modes, whose main differences among them are the amplitude of the undulation wavelength and the thrust-generating force: *anguilliform*, *sub-carangiform*, *carangiform*, *thunniform*:

- *Anguilliform* the body of the fish is bent in large-amplitude undulations. Since at least a complete wavelength is always present along the body, the moment about the yaw axis is usually neglected, i.e. no tendency to recoil is exhibited. The same features feature allow these swimmers to move backward by means of an inversion of direction of the propulsive wave.
- *Sub-carangiform* and *Carangiform* swimmers employ the same mechanism, but with

different percentage of the body involved in the undulation, i.e. one half for the former, and one third for the latter. Thus, *Carangiform* swimmers have a stiffer body, exhibiting a lower turning and accelerating capabilities.

- *Thunniform* locomotion is the most efficient BCF mode, usually described as the apex of swimming evolution. The thrust is generated thanks the caudal fin (more than 90%) through lift mechanism, the rest is produced by the added mass effect associated with the lateral undulations of the are near the peduncle. This mechanism allow the *thunniform* swimmers to keep high cruising speeds for long time. The slender, streamlined body the *thunniform* swimmers is able to minimize the drag while moving forward, while the stiff, crescent-moon shape of the caudal fin minimizes the induced drag due to lift generation ([Lighthill, 1970]).
- *Ostraciiform* locomotion it the only purely oscillatory BCF mode. The caudal fin oscillates in a pendulum-like discipline, while the body remains rather rigid. Fish using this mode are usually encased in inflexible bodies and forage their complex habitat by means of MPF propulsion.

2.4 Undulation vs Oscillation

For this research the most important distinction for pectoral-fin-based locomotion is: undulation and oscillation. Undulation of the pectoral fins, termed ‘rajiform’ locomotion [Breder, 1926], is defined by having more than one wave present on the fins at a time [Webb, 1994]. Skates and most stingrays are thought to use this mode of locomotion. Oscillation of the pectoral fins, termed ‘mobuliform’ locomotion is more similar to flapping in birds; the fins move up and down with less than half a wave on the fins. Pelagic stingrays, such as manta, cownose, eagle and bat rays, use the oscillatory mode. Many fishes, including some batoids, use modes of locomotion that do not fit into the categories of ‘undulatory’ and ‘oscillatory’ in that there is between half a wave and one wave present on the fins or body.[Rosenberger, 2001b] Although two extremes of locomotion between undulation and oscillation have been recognized, all fishes are true undulators in that waves are passed down the body or fins. The difference lies in the number of waves present. When the number of waves is small (less than half a wave), the motion appears

to look like an oscillating plate, and this mode has been called ‘oscillatory’. Alternatively, when the wave number is larger, the fin looks more undulatory. Most taxonomic groups of fishes are assigned to one category or the other and lack representatives along the continuum. Batoids are one of the few groups of fishes with representatives at each extreme of the continuum, making them ideal for comparing undulatory and oscillatory kinematics within a group of closely related fishes. Although the categories of undulation and oscillation accurately describe the fin kinematics of some species of batoids, other species appear to be intermediate between the two extremes. Undulatory pectoral locomotion

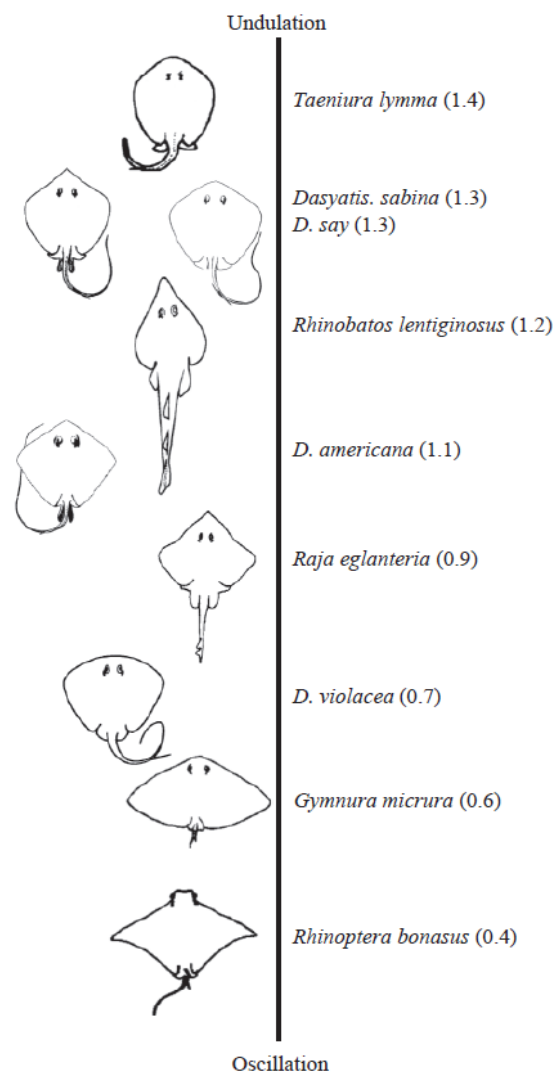


Figure 2.10: Line drawings of the eight batoid species in this study. (A) *Dasyatis sabina*, (B) *Dasyatis say*, (C) *Dasyatis americana* Hildebrand and Schroeder, (D) *Dasyatis violacea*, (E) *Rhinobatos lentiginosus*, (F) *Raja eglantheria* Bosc, (G) *Gymnura micrura* and (H) *Rhinoptera bonasus*

is the most common mode of swimming among the batoid fishes and is located at one

extreme of the undulation/oscillation continuum. Five of the nine batoid species studied, including *Taeniura lymma*, *Dasyatis sabina*, *D. say*, *D. americana* and *Rhinobatos lentiginosus*, fall within the definition of undulation because they have more than one wave present [Rosenberger and Westneat, 1999]. *Rhinoptera bonasus* is the only species that exhibits oscillatory behavior as defined as having less than half a wave present on the fin. *Rhinoptera bonasus* swims using broad up- and down-strokes with less than half a wave present on the fins, which can be considered a form of underwater flight [Heine, 1993a]. Frequency is quite low with respect to the other batoids, and amplitude is the highest among the eight species in this study. *Rhinoptera bonasus* also exhibits a unique kinematic behavior in fin amplitude compared with other stingrays. During the down-stroke, the fins do not extend below the ventral body axis, resulting in a fin amplitude that is not as large as one might expect on the basis of the extremely elongated fins. Although this species is found mostly in the water column, it is tied to the bottom for feeding on molluscs and crustaceans. A possible advantage of avoiding a ventral displacement during the down-stroke is to utilize the ventral lateral line canals fully to detect prey better in the substratum. Undulatory and oscillatory pectoral locomotion in batoids [Moored et al., 2011] is analogous to rowing (drag-based) and flapping (lift-based) pectoral locomotion in bony fishes, respectively. Undulatory and rowing-based swimmers are specialized for mechanically efficient low-speed swimming, reduced drag from the body and fins, and a high level of control or manoeuvrability. In contrast, oscillatory swimmers have a better lift performance, are good at efficient steady cruising because of their higher thrust production and are believed to be less manoeuvrable.

2.5 Power Requirements And Efficiency

Both biological and engineered systems evolve towards reducing the total energy consumption of the system when completing any activity. AUVs are inevitably equipped with a finite energy store; so reducing the energy cost per unit distance travelled the range of the vehicle may be enhanced. [Phillips et al., 2012a] To carry out any daily activity it is necessary that the amount of energy acquired by an individual through food must exceed the amount of energy spent. Based on optimal foraging theory, natural selection should

operate to maximise the ratio of energy income to energy expenditure.[Bale et al., 2014] Hence, the solutions adopted by marine animals to reduce their energetic requirements may provide inspiration to enhance the design of the next generation of free swimming AUVs. In order to evaluate the benefits of bio inspiration, it is important to have a coherent set of metrics that allows a fair comparison, for the performance of engineered and biological systems.[Pettersson and Hedenström, 2000] Propulsive efficiency is often quoted by both engineers and biologists as a measure of the ratio of the effective power to the power delivered to the propulsion system.

$$\eta_p = \frac{EffectivePower}{DeliveredPower} \quad (2.4)$$

Numerous authors have quoted high propulsive efficiencies, η_p , for marine animals operating at turbulent Reynolds numbers using carangiform and thunniform type propulsion (high speed long-distance swimmers where virtually all movement is in the caudal fin). For example, the propulsive efficiencies of pseudo killer whales at 0.9 ([Phillips et al., 2012b]), bottlenose dolphins at 0.81 and fin whale at 0.85 ([Bose and Lien, 1989]) are high compared with those of a typical propeller ([Brandt and Selig, 2011]) open water efficiency of 0.5 to 0.7. However, these results must be treated with caution due to the action of any propulsor, be it an oscillating foil, propeller or water jet, which locally modifies the flow around the individual and consequently the resistance of a self-propelled individual compared to a towed (or passive) individual is changed. For ships the increase in self-propelled resistance is included as part of the propulsive efficiency rather than as an increment on the drag. Thus the propulsive efficiency of an AUV is:

$$\eta_{engineering} = \frac{TowedResistance \cdot Velocity}{PropulsivePower} \quad (2.5)$$

While not universally accepted, in biology the influence of the propulsor on the ‘drag’ is often considered as an added resistance factor, λ , which is the ratio of the swimming thrust to passive drag:

$$\lambda = \frac{SwimmingThrust}{PassiveDrag} \quad (2.6)$$

The added resistance factor is highly dependent on propulsive mode and accounts for drag increases due to large-amplitude lateral body movements that modify the water

flow in the boundary layer and around the body, resulting in increased frictional and form drag. Experimental data highlighted by Webb, 1975 demonstrates that the drag coefficient for fish swimming at high Reynolds numbers can reach up to four times that of a rigidly gliding fish. Importantly this added resistance is typically not included in the propulsive efficiency. Hence the propulsive efficiency of a marine animal is often taken to be [Nesteruk et al., 2014]:

$$\eta_{pbiology} = \frac{SwimmingThrust \cdot Velocity}{PowerInWake} \quad (2.7)$$

Due to the lack of energetic data for aquatic animals, empirical models have been developed to improve and enhance understanding. The approach aims to provide a framework for understanding trends and general relationships, and to provide a means to explore potentially interesting areas. An equivalent spheroid efficiency is proposed to achieve a fair comparison between engineered and biological systems. For both systems typically only limited data is available, consequently this is reflected in the set of key parameters. To reduce the complexity of the model it has been assumed that the shape of the biological or engineered system corresponds to that of an equivalent spheroid, defined as a neutrally buoyant prolate spheroid with the same length and mass as the individual, the equivalent diameter can be determined from:

$$D_s = \sqrt{\frac{6m}{\rho\pi L}} \quad (2.8)$$

while the surface area is determined from:

$$A_s = 2\pi \frac{(D_s)^2}{4} \left(1 + \frac{L}{D_s \epsilon} \sin^{-1} \epsilon\right) \quad (2.9)$$

where $\epsilon = \sqrt{1 - \frac{(D_s)^2}{L^2}}$.

This assumption allows to estimate the key parameters including diameter or wetted surface area. The assumption that the individual may be represented as a prolate spheroid allows predictions to be made regarding the energetic costs of an individual. To generalize the analytical model each equivalent spheroid is defined by its mass and its slenderness

ratio, $\frac{L}{D_s}$. Thus the length is given by:

$$L = cm^{1/3} \quad (2.10)$$

where:

$$c = \left(\frac{6(\frac{L}{D_s})^2}{\rho\pi} \right)^{1/3} \quad (2.11)$$

Note c is a constant for all geometrically similar spheroids in the same fluid. The wetted surface area can be approximated by $A_s \approx dm^{2/3}$ where:

$$d = \left(\frac{1}{\rho} \right)^{2/3} \left(-0.0122 \left(\frac{L}{D_s} \right)^2 + 0.5196 \frac{L}{D_s} + 4.2732 \right) \quad (2.12)$$

Again d is a constant for geometrically similar spheroids operating in the same fluid. For $1.1 > \frac{L}{D_s} < 15$ this approximation gives an error of less than 1 % of the exact wetted surface area.

The total powering characteristics of the idealised system can be derived by modelling the in-water maintenance costs and the propulsion power requirements. The in water-maintenance cost will be represented by a power function:

$$P_H = am^b \quad (2.13)$$

where a is a constant of proportionality, m is the system mass and b is the allometric scaling exponent. This relationship is usually used to describe the connection between body mass and energy metabolism in animals.[Heusner, 1985] Dimensional analysis and engineering practice allow to determine the total propulsion power (i.e the power drawn by the entire propulsion system including actuators) of a deeply submerged individual can be determined from [Phillips et al., 2012c]:

$$P_p = \frac{\rho}{2\eta_a\eta_p} C_D A U^3 \quad (2.14)$$

where, ρ is the fluid density, C_D is the drag coefficient of a towed (or passive) system, A is the wetted surface area of the system, η_a is the actuator efficiency and η_p is the propulsive efficiency. Using a similar argument the power requirement of a 100 % efficient equivalent

spheroid, P_{PS} , may be calculated from:

$$P_{PS} = \frac{\rho}{2} C_{D_s} A_s U^3 \quad (2.15)$$

where C_{D_s} is the drag coefficient, and A_s the wetted surface area of the equivalent spheroid. Defining the equivalent spheroid efficiency, ζ , as the ratio of the power required to propel a 100% efficient equivalent spheroid to the power required by a real individual at the same speed,

$$\zeta = \frac{P_{PS}}{P_P} = \eta_a \eta_p \frac{C_{D_s} A_s}{C_D A} \quad (2.16)$$

ζ includes both hydrodynamic and actuator efficiency, in addition it takes into account the difference in drag coefficient and wetted surface area between the real and equivalent systems. Thus the propulsion power can be represented by,

$$P_P = \frac{\rho}{2\zeta} C_{D_s} A_s U^3 \quad (2.17)$$

For this research it is assumed that the equivalent spheroid efficiency does not depend on the forward speed. Supposing also that neither ρ or A_s depend on other variables. To calculate the only system specific information required are length, mass and propulsion power at a set speed. By exploiting the methodologies of Hughes developed for scaling of drag components of ships, the drag of a deeply submerged spheroid experiencing only viscous drag, C_v , may be represented by:

$$C_{D_s} = C_v = F_f(1 + k) \quad (2.18)$$

where C_f is the skin friction coefficient based on flat plate results, while the $(1 + k)$ is a form factor dependent on hull form to account for the viscous pressure resistance (Molland et al., 2011). The standard skin friction lines for laminar flow (Blasius line) and turbulent flow (von Kármán line) past a flat plate are of the form:

$$C_f = \alpha Re^\beta \quad (2.19)$$

where the constant, α , and the exponent, β , are flow regime dependent and, Re , is the length based Reynolds number. The form factor $(1 + k)$ of an spheroid can be predicted

empirically from Hoerner, 1965:

$$(1 + k) = 1 + 1.5 \left(\frac{L}{D_s} \right)^{-3/2} + 7 \left(\frac{L}{D_s} \right)^{-3} \quad (2.20)$$

The propulsion power requirement is given by:

$$P_P = \frac{e}{\zeta} \alpha m^{\frac{\beta+2}{3}} U^{3+\beta} \quad (2.21)$$

where

$$e = \frac{\rho}{2} (1 + k) \frac{c^\beta}{v^\beta} d \quad (2.22)$$

A common measure of swimming efficiency is Froude efficiency η , defined as:

$$\eta = \frac{\langle T \rangle U}{\langle P \rangle} \quad (2.23)$$

where U is the mean forward velocity of the fish, $\langle T \rangle$ is the time-averaged thrust produced and $\langle P \rangle$ is the time-averaged power required. A widely used method to compare the energetic performance of different animals is Cost of Transport, COT ([Rosen and Trites, 2002]; [Tucker et al., 1970]; [Videler and Nolet, 1990]). COT is a measure of the energy required to transport the mass m of an individual, over a unit distance at a speed U . The general formulation of cost of transport for an individual is given by:

$$COT = \frac{P_H + P_P}{mU} \quad (2.24)$$

Where P_H , is the power expended to operate or sustain the animal's non-propulsion systems, and P_P is the power associated with propulsion. For engineered systems the power expended on non-propulsion systems is often referred to as the hotel load and is associated with powering computers, hard drives and all the sensors required to provide functions equivalent to those of an animal, such as knowing orientation and position, and condition monitoring. This is equivalent to the in-water maintenance cost of a marine animal while at rest associated with blood flow, respiration etc. However, the hotel load in an underwater vehicle can be defined to include the power consumed by the instruments carried as payload, such as those to make measurements of the environment. Payload power con-

sumption can be similar to, or can exceed, the power required for maintaining the vehicle's core systems. Consequently, in this study, because there is no animal equivalent, payload power consumption is excluded. The energetic costs of propulsion, P_P , of an individual, animal or underwater vehicle, is as a direct result of generating thrust to overcome fluid dynamic drag. The energy required is influenced by a variety of environmental factors, such as water temperature and salinity, propulsion methods and associated efficiency as well as physiological and morphological characteristics of the system. Substituting Equa-

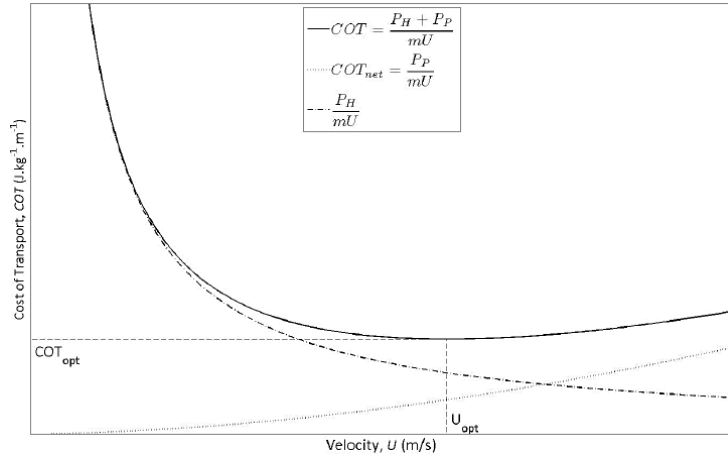


Figure 2.11: Idealised cost of transport curve. The net cost of transport, COT_{net} , is often defined as the component of the cost of transport associated with propulsion.

tions 2.13 and 2.14 into Equation 2.24 the cost of transport for an equivalent spheroid is:

$$COT = \frac{am^b + \frac{e}{\zeta}\alpha m^{\frac{\beta+2}{3}}U^{3+\beta}}{mU} \quad (2.25)$$

COT versus swimming speed results in a U shaped function, see Figure 2.11, the optimum swimming speed, U_{opt} associated with the minimum cost of transport COT_{opt} may be established by differentiating Equation 2.25 with respect to U , then setting the result equal to zero to find the global minimum and then rearranging for U_{opt} :

$$U_{opt} = \left(\frac{a\zeta}{(2 + \beta)e\alpha} \right)^{\frac{1}{3+\beta}} m^{\frac{3b-\beta-2}{9+3\beta}} \quad (2.26)$$

For aquatic animals and underwater vehicles, is important to minimize their cost of transport by swimming at their optimum speed in order to maximise their range given a finite store of energy. Marine animals with low cost of transport have developed a combined

morphology and kinematics of swimming that may lead to the design of bio-inspired long range underwater vehicles with enhanced performance [Ohlberger et al., 2006]. However, given that there are inherent difficulties when seeking to compare engineered and biological systems, there must be a rational basis for selecting which characteristics and which animals to use as the basis for inspiration.

The model incorporates the use of an equivalent spheroid efficiency as a fair metric to compare engineered and biological systems. This can be readily calculated from typically available data. To calculate equivalent spheroid efficiency the only system specific information required are length, mass and propulsion power at a set speed. Results from the model are used to provide useful insights into the scaling of common performance metrics with respect to system mass, such as cost of transport. The analysis in this work are based upon swimming speeds and energy consumption [Allen et al., 2000]. Therefore, the scaling considers a combination of drag, thrust and “hull” efficiency as a complete system. As a result it would be possible to make a judgement on the performance of a swimming system. In addition, the analytical model provides a physics-based selection tool to help with selecting candidate marine animal species for bio-inspiration, and biologists can use this approach to help understand the observed performance of marine animals.

Chapter 3

Manta Ray Hydrodynamics

For millions of years, aquatic species have utilized the principles of unsteady hydrodynamics for propulsion and manoeuvring [HüMMA, 1997a]. They have evolved high-endurance swimming that can outperform current underwater vehicle technology in the areas of stealth, manoeuvrability and control authority. Batoid fishes, including the manta ray, *Manta birostris*, the cownose ray, *Rhinoptera bonasus*, and the Atlantic stingray, *Dasyatis sabina*, have been identified as a high-performing species due to their ability to migrate long distances, manoeuvre in spaces the size of their tip-to-tip wing span, produce enough thrust to leap out of the water, populate many underwater regions, and attain sustained swimming speeds of 2.8 m/s with low flapping/undulating frequencies [Heine, 1993b]. This suggests that these species have evolved to become high endurance swimmers. Additionally, this system has the potential to transition to a fast, manoeuvrable vehicle that can operate in dynamic environments such as the littoral zone or areas with large currents and high wave action. Observations of various rays show them to be highly maneuverable and adaptable to local conditions. Their ability to control their stability via the pectoral fins, especially when compensating for challenging environments [HüMMA, 1997b], must also be considered as a desirable characteristic to emulate in an underwater vehicle. Moreover, a batoid-inspired vehicle would have a large planform surface area, making this platform an excellent candidate for flexible solar cells to extend its range. In addition, the rigid body of batoids permits space for control systems, sensory devices and increased payload. Higher efficiency and velocity are occupied by their flapping motion than fluctuating motion of other elasmobranchs, which can also be proved by their well-known

long distance migration. Gliding by holding their fins outright can also lower energy cost. Research results show that robotic fish equipped with pectoral fins exhibits high manoeuvrability and body flexibility. Noise can be reduced by their lower flapping frequency than other swimming types. Compact, efficiency, manoeuvrability and noiseless, all these outstanding features attract researchers to consider cow-nosed ray as an ideal natural sample for designing fish-like robot

3.1 Biology

Mantas (*Mobula birostris* and *Mobula alfredi*; family *Myliobatidae*) are the largest of the over 500 elasmobranch species of batoid fishes (skates and stingrays), which have relatively rigid dorsoventrally compressed bodies and expanded pectoral fins. The manta can weigh over 1580 kg and is reported to have high-aspect-ratio (3.5, ratio of span to chord) pectoral fins that can reach a span of over 9 m [Fish et al., 2018]. Mantas use oscillatory locomotion (mobuliform mode) where there is a small undulatory component and swim primarily by flapping the pectoral fins dorsoventrally, analogous to the flight of birds. Mantas are able to execute turning maneuvers. The pectoral fins exhibit a range of both symmetrical and asymmetrical motions which can assist in turning. Although capable of leaping behaviour, the most notable swimming manoeuvre by manta is a looping or backward somersault behaviour used in feeding and mating.

The cownose ray's key movement features can be summarized as follows:

- The pectoral foil flaps with frequencies varying from 0.4 to 1.2 Hz, according to

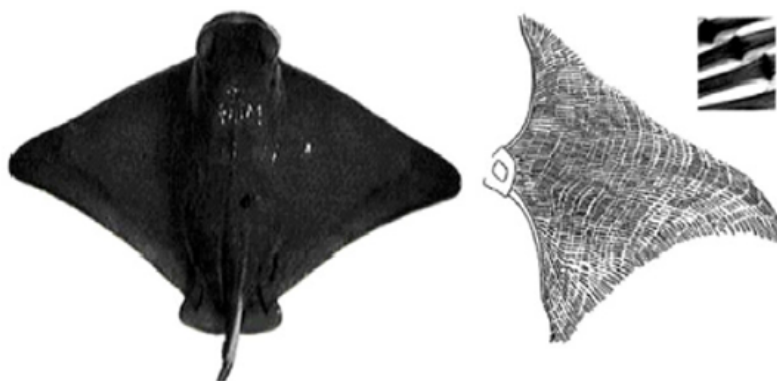


Figure 3.1: Overlook and right fin skeleton of Manta Ray

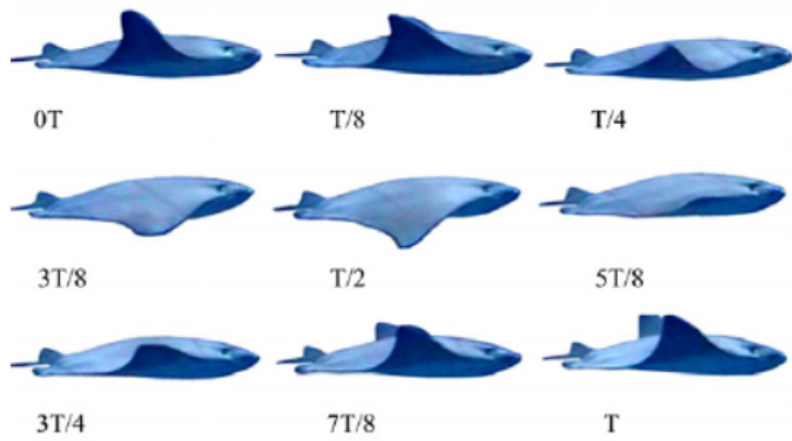


Figure 3.2: Full flapping cycle of free swimming of Manta ray

the swim conditions. Frequencies between 0.5 and 0.6 Hz are typically used in linear-forward swim modes.

- Foil deformation in flapping movements is consistent with sinusoidal discipline, especially along the chordwise direction.
- The flapping amplitude of the cownose ray's pectoral foil is as large as half of the fin-base length.
- The flapping motion of the pectoral fin is not symmetrical with respect to the horizontal plane, indeed the flapping amplitude above the horizontal plane is about twice that below it.

A typical full flapping circle of cow-nosed ray is shown in Fig.3.2. It shows that the pectoral fins flap almost above the ventral body axis and only a little extends it during the down-stroke in normal linear swimming.

3.2 Body Structure Analysis

The body shape of manta rays mainly affects its swimming performance in two aspects:

- the reduction of water resistance.
- the stability when swimming.

The water resistance is minimized by the streamlined shape which could be observed from lateral view. The flattened diamond shaped body contributes to keep the stability while swimming. As already said Mantas swim by exclusively flapping their expanded pectoral fins in the vertical plane through and upstroke and downstroke (Fig.3.2). The stroke is dorsoventrally asymmetrical with a gliding phase at the top of the stroke particularly at slow swimming speed. This asymmetry produced oscillations in swimming speed. In addition, the fin tips were abducted higher over the longitudinal axis of the body than adducted under the body [Stevens et al., 2018]. Both spanwise and chordwise flexibility were apparent as the pectoral fins were oscillated. Initiation of both upstroke and downstroke occurred at the anterior base of the fin and proceeded movement of the fin tip in the same direction. These actions resulted in a wave moving spanwise through the fin from fin base to tip with less than one full wavelength. Another wave of longer wavelength was directed chordwise through the fin. Flexibility in the fin also produced twisting toward the fin tip during the upstroke. Detailed kinematic features of the fin flapping based on a high-resolution reconstruction was presented: the frequency of oscillation of the pectoral fins increased directly with increasing swimming speed according to the equation:

$$f = 0.189 + 0.223U \quad (3.1)$$

The heave amplitude (A) did not demonstrate a statistically significant change with U and the Strouhal number (St) decreased asymptotically with increasing U as is shown in Fig.3.3 The highest propulsive efficiencies for oscillating foils are found at $St = 0.25-0.4$. St is related to how fast vortices are being shed into the wake of an oscillating foil and the space between the vortices at each half stroke. The deformation caused by the flapping could be decomposed into two waves, as the wave A and B(fig. 3.4).

The wave A is along the direction of pectoral wingspan, as the same as the perpendicular aforementioned previously. Because the calcification of the cartilage decreases from the base of the fin to the tip, the amplitude of the wave A increases accordingly. The wave B is perpendicular to the wave A, along the direction of the fin's base connecting the pectoral fin with the body. Both waves share the same frequency. F_{AL} and F_{BL} are forces generated by wave A and B on the left pectoral fin, while F_{AR} and F_{BR} are the same for the right pectoral fin. The magnitudes of the forces generated by two waves on

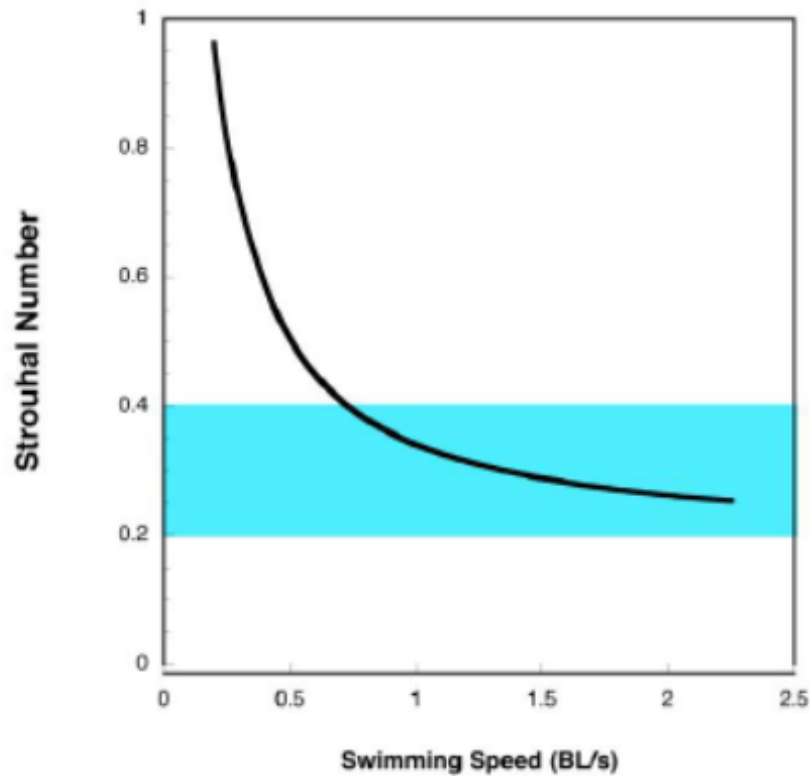


Figure 3.3: Strouhal number as a function of swimming speed. The shaded blue area indicates the region where maximum propulsive efficiency occurs.

each pectoral fin could be changed independently by adjusting the amplitudes of the two waves to form a resultant force along the swimming direction. During each downstroke or upstroke, there is a vortex ring shed from the trailing edge of the fin, leaving two sets of inter-connected vortex rings in the wake. Because the flapping motions of the left pectoral fin and the right one are symmetric, the flow induced by those fins exhibited strict symmetry with respect to the mid-plane of the body (see Figure 3.5a). Vortices generated by both the downstroke and upstroke induces strong jets (Figure 3.5d, red arrows), which have backward components and thus are responsible for the thrust production.

The velocity jets are indicative of thrust production because the force to cause a momentum change of the fluid is accompanied by an equal and opposite force acting on the body. This force was reflected in the pressure field acting over the body presented in Fig.3.6 The boundary layer flow is initially laminar starting at the stagnation point and the skin friction increased as the flow accelerates around the leading edge. Then the skin friction decreased as the flow slows down due to the adverse pressure gradient over the top of the ray.[Clark and Smits, 2006] Around halfway down the length of the ray, the

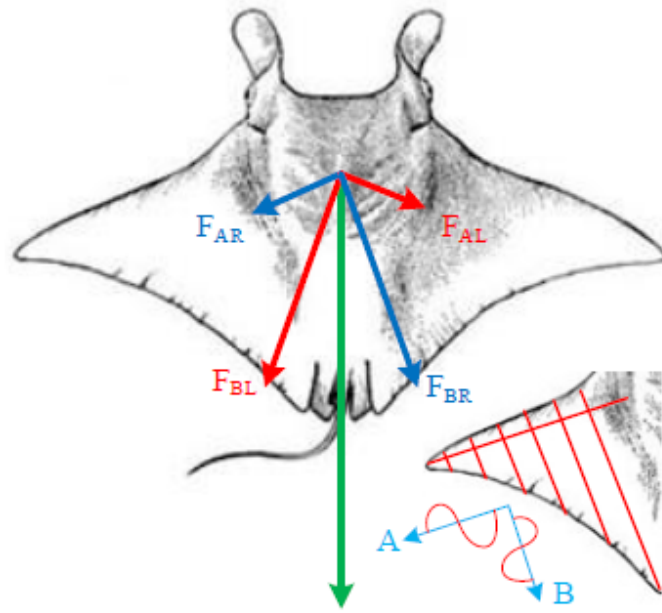


Figure 3.4: Forces generated by wave A and B

boundary layer transitions to a turbulent boundary layer. The skin friction jumps up and then continues to slowly decrease as the flow slows down approaching the trailing-edge stagnation point. The time-varying contributions to the force production are distinguished as the pressure forces acting on the fins and body and the shear forces acting on the fins and body (figure 3.6c). The estimate of the form drag pressure force was nearly zero and acts solely on the fins. The pressure force on the fin is the only contributor to thrust production. The shear force on both the fins and body is seen to incur a drag penalty.

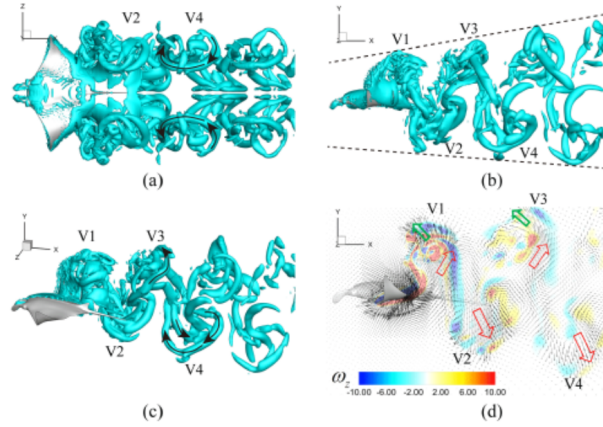


Figure 3.5: a) Ventral; b) lateral and c) perspective view of the 3D flow structures; d) vorticity and velocity field. The rotating directions of an upstroke generated vortex ring (V3) and a downstroke generated vortex ring (V4) are labeled by black arrows. Red and green arrows represent backward and forward jets.

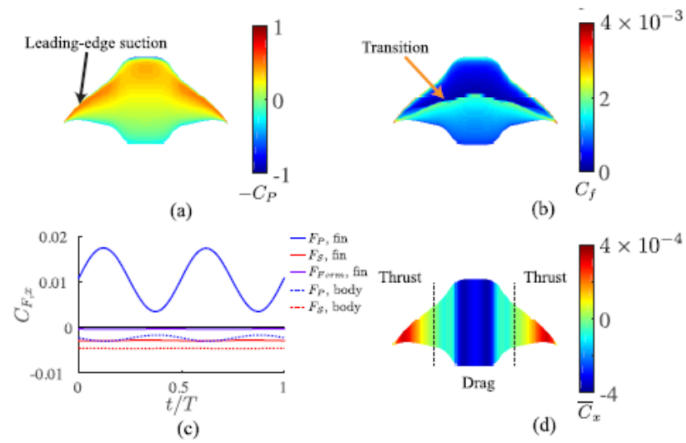


Figure 3.6: a) Time-averaged pressure coefficient distribution over the manta ray; b) Time-averaged skin friction coefficient distribution over manta ray; c) Time-varying forces decomposed into pressure forces acting on the fins and body and shear forces acting on the fins and body. The form drag (pressure force) acting on the fins is also included; d) Time-averaged net force coefficient integrated over chordwise strips.

3.3 Turning Maneuvers

Yawing turns were accompanied with banking (rolling) of the body by 3–80 deg from the vertical as it is shown in Fig. 3.7. The turns performed by mantas were produced by a combination of translational and rotational movements. As mantas have a rigid body, the turning performance measured from anterior and posterior points on the body were the same and thus reflect the turning performance of the COM. The COM would be on a line between the two points of measurement. For mantas as well as other mobuliform rays, the COM is located at 47% of body length. [Parson et al., 2011] The mantas were able to execute turns by unpowered glides and powered flapping motions. In powered turns by the manta and other myliobatid rays, propulsive motions of the pectoral fins were evident throughout the entire turn. Turning was accomplished by differential movements of the pectoral fins, with the outboard fin flapping at a higher frequency than the inboard fin. Unpowered turns would rely on banking. Banking was required to generate the centripetal force to produce a curved trajectory. Banking is a rolling manoeuvre that provides a greater projected area facing the axis of the turn. Lift is generated primarily from the pectoral fins and additionally from the cambered body. The lift vector is perpendicular to the frontal plane of the body and fins of the ray. The lift opposes a hydrodynamic force generated from the combined forces of the drag on the body and fins in the transverse plane and weight of the negatively buoyant animal. The horizontal component of the lift vector generated by the pectoral fins produces a centripetal force which turns the manta. Aside from yawing turns, mantas are able to turn by pitching to execute somersaults in a looping circular trajectory. This somersault maneuver is used by mantas for feeding on concentrations of krill. This turning performance was greater than yawing turns in terms of R/L by 1.7 times. The difference in performance for R/L represents limitations owing to flexibility of the pectoral fins versus the body that differentially affect movement about the rotation axes (pitch, yaw, roll). In yawing turns, torques can be generated from both passive and active synchronization and movements of the fins in addition to a centripetal force from banking. For pitching turns, the body is rigid in the sagittal plane resisting pitch [Fontanella et al., 2013]. However, by simultaneous movements and chordwise bending of the flexible pectoral fins, mantas can execute small radius turns in the sagittal plane. The relatively rigid body, particularly with regard to lateral bending,

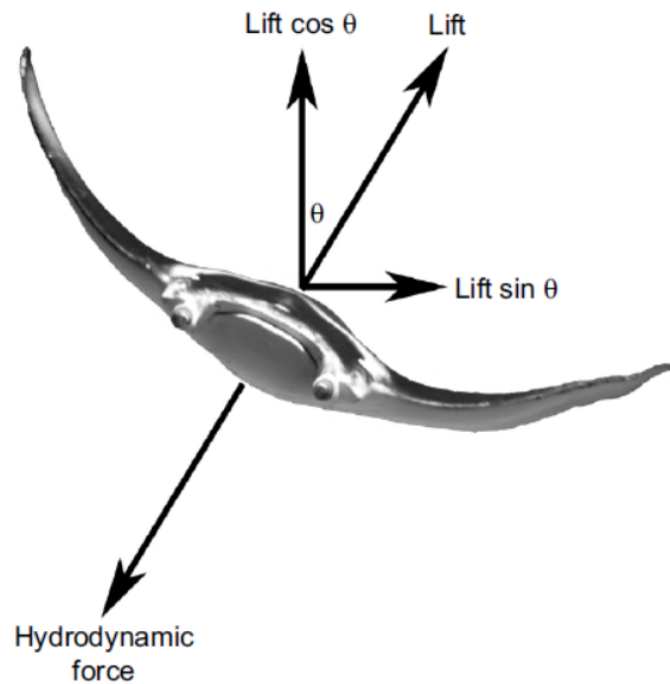


Figure 3.7: Turning maneuvers

would limit yawing turns. However, mantas can compensate for their inflexibility by using the flexible distal portions of the pectoral fins or asymmetrical fin movements, and banking maneuvers.

At this point, after defining the main mechanisms of swimming and the advantages that bio inspiration can introduce in the field of autonomous underwater vehicles, it is possible to reach the purpose of this research. The aim is to conceive, design and control a bio-inspired robot that fully emulates the main characteristics of a manta ray in order to exploit its advantages such as high motion efficiency. First of all, to obtain a motion with high efficiency, the kinematic synthesis of the mechanisms is exploited to obtain the oscillatory motion.

Chapter 4

Mechanism Synthesis and Design

After highlighting the benefits of bio inspiration, studying the properties and interactions with water that occur during swimming of a fish, listing the main advantages and characteristics of a manta ray it is possible to focus on the truth purpose of this research. The aim of this research, in fact, is to program, design and control this bio inspired robot in order to faithfully replicate all the properties and advantages described above that allow a bio inspired robot to be more advantageous than a traditional autonomous underwater vehicle.

To handle complicated underwater environments, the cownose ray has many different swim modes, including linear-forward swim, turn, up-floating, and diving. When confronted with obstacles such as reefs, seaweed, or predators, cownose rays will merge different swimming postures to realize a quick turn or a rolling swim. All the cownose ray's required swimming modes are made possible by its large, flat pectoral foils and its flexible body, which result from the complex biological structures of the ray's flexible cartilage, muscles, and body. These natural characteristics, however, are too complicated for a manufactured mechanism to replicate at this stage. As a result, the design has some simplifications and seeks to approximate the cownose ray's outstanding swim performance by reproducing its key characteristics. In order to better replicate the characteristics that make manta ray an excellent resource in the bio-inspired field, three different areas of study are distinguished:

- **Shape:** guarantees aerodynamics and reduced viscous friction
- **Fin:** guarantees the efficiency of the motion.

- **Tail:** guarantees balance in the yaw phases.

4.1 Shape And Coating

The first field of study of this project is the reproduction of the shape of the manta ray. With reference from literature the fin's longitudinal profile is obtained through the reconstruction of a curve that follows the real manta ray profile .

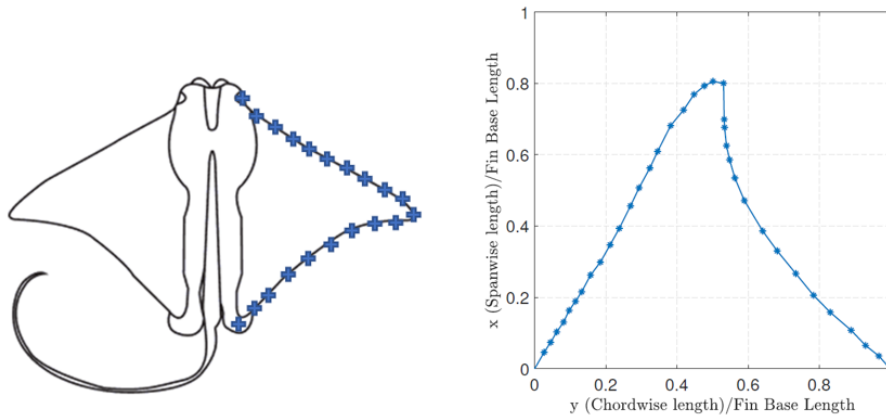


Figure 4.1: Cownose ray and the relative pectoral fin shape.

With reference to the example of a cownose ray, as seen in the figure 4.1, the profile of the pectoral fin was extracted with matlab. The spatial shape of the pectoral foil is an obvious characteristic that affects propulsion performance. Referring to cross sections along

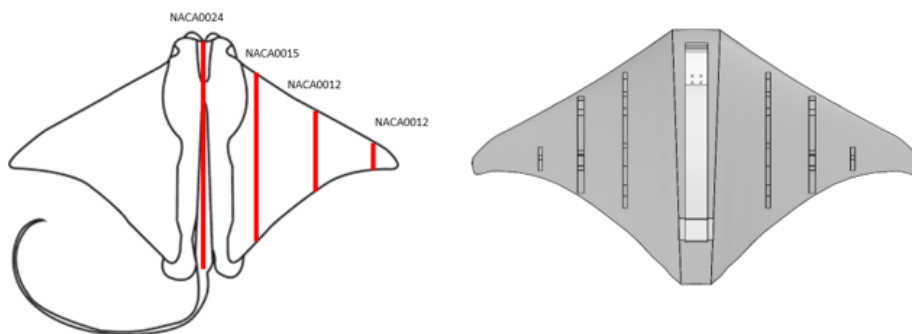


Figure 4.2: Cross section and shape of a cownose ray.

the chordwise direction(fig. 4.2) of the cownose ray's pectoral foil can be approximated to a series of airfoil shapes developed by the National Advisory Committee for Aeronautics (NACA), NACA0024, NACA0015 and NACA0012, with gradient changes from midbody

to the fin tip. The NACA are airfoil shapes for aircraft wings for Aeronautics. The shape of the airfoils is described using a series of digits following the word "NACA". The parameters in the numerical code can be entered into equations to precisely generate the cross-section of the airfoil and calculate its properties. The NACA four-digit wing sections define the profile by (fig. 4.3):

- First digit describing maximum camber as percentage of the chord.
- Second digit describing the distance of maximum camber from the airfoil leading edge in tenths of the chord.
- Last two digits describing maximum thickness of the airfoil as percent of the chord.

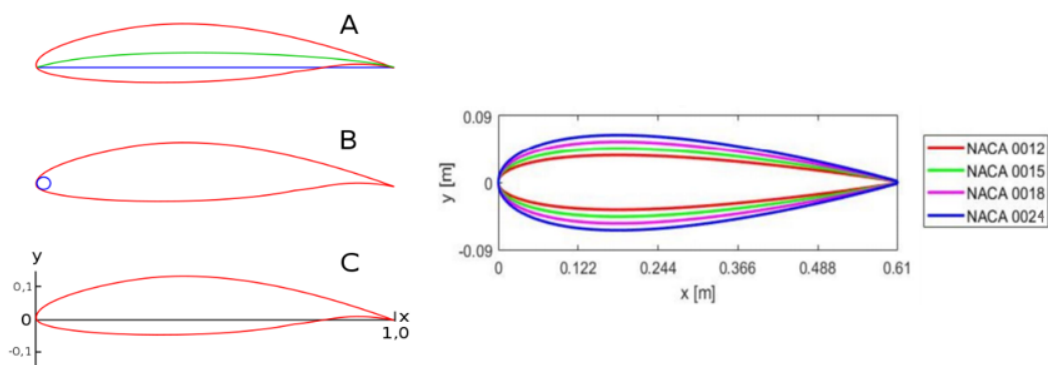


Figure 4.3: A) Blue line=the chord, green line=camber mean-line. B) Leading-edge radius, C) x,y axes

For example the NACA 0015 airfoil is symmetrical, the 00 indicating that it has no camber. The 15 indicates that the airfoil has a 15 % thickness to chord length ratio: it is 15 % as thick as it is long. The formula for the shape of a NACA 00xx foil, with "x" being replaced by the percentage of thickness to chord, is:

$$y_t = 5t[0.2969\sqrt{x} - 0.1260x - 0.3516x^2 + 0.2843x^3 - 0.1015x^4] \quad (4.1)$$

where x is the position along the chord from 0 to 1, y_t is the half thickness at a given value of x (centerline to surface) and t is the maximum thickness as a fraction of the chord (so it gives the last two digits in the NACA 4-digit denomination divided by 100). Thanks to the airfoil tool it is possible to simplify the extraction process of the desired

NACA. In fact this is a database of 1636 airfoils available, filtered by name, thickness and camber that allows to extract the coordinates of points which interpolated generate the required profile(Fig ??). The NACA0024 is used for the central body of the robot and contains the main components such as motors, supports and all the most sensitive elements (fig.4.4); it is rigid and was made with additive manufacturing technology like most components. What concerned NACA0012 and NACA0015, they must be flexible to

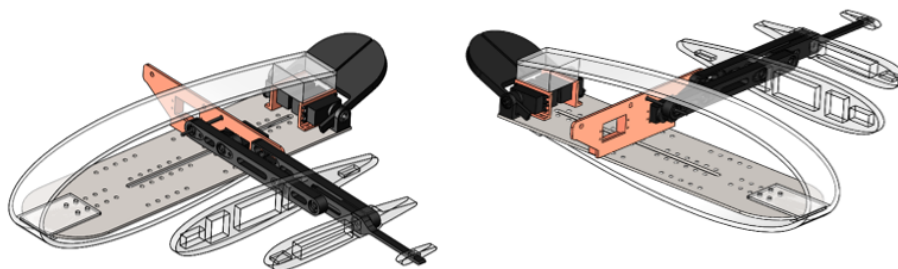


Figure 4.4: positioning of the different NACA sections along the robot prototype

guarantee the oscillatory motion and the phase shift between the three different fins but at the same time they must maintain the aerodynamic shape which gives to the robot a reduction in friction.

For these reasons the material chosen is silicone and molds have been made to physically obtain the profiles. After having generated the pectoral fin profile and having studied the cross section it is possible to obtain the final shape of the robot. The shape obtained is scaled in order to obtain a wingspan of the fins equal to 1m as can be seen in figure (fig.4.5).

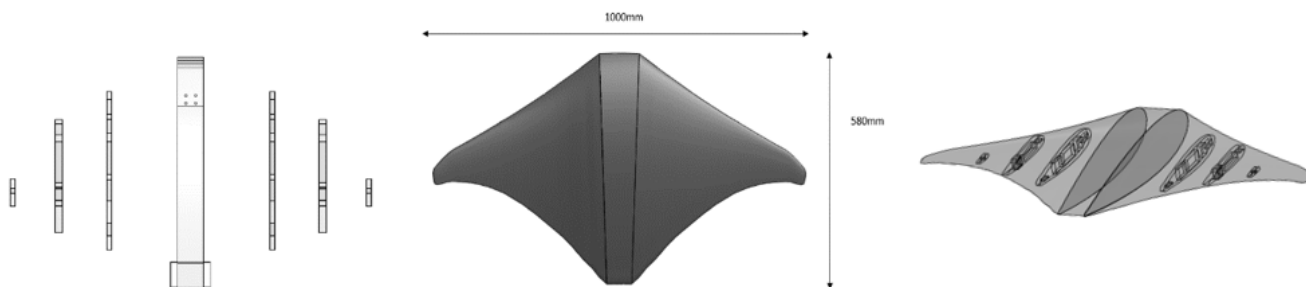


Figure 4.5: Profile, shape and final dimension of Manta ray robot.

Lastly the coating plays a fundamental role. In fact, in addition to ensuring the protection of water sensitive components, it must also guarantee the body shape throughout

the movement without obstructing the fins.

4.2 Pectoral Fin Kinematics

The main thrust source is the pectoral fin system, which is the key structure in designing a bionic fish mimicking a cownose ray. Flexibility of the fin system was found to have a large impact on the propulsion performance of pectoral foil. Indeed, the flexibility of the fin guarantees superior hydrodynamic performances in generating propulsion force during cruising, bursting and maneuvering. The biomimetic prototypes with oscillating pectoral fins can be grouped into two categories:

- **Single fin ray** with simple fin surface movement: the driving fin ray is made of rigid material and strengthened flexible material is arranged at the leading edge; the remaining part of the pectoral fin is made of flexible material. The flexible part of the fin can be easily deformed under the pressure of the hydrodynamic loads. The advantages of the single fin ray configuration are:
 - simple structure;
 - easy realization of the oscillating motion;
 - good adaptation of fin surface for water.

The drawbacks of the single fin ray configuration are:

- the transmission of waves is determined by the characteristics of the material, which must be chosen carefully. The wave transmission has a large impact on the force generations for propulsion;
 - poor maneuverability;
 - only realization of functional bionics.
- **Multiple fin rays** with complex active controllable fin surface movement. An active and controllable pectoral fin's oscillating motion can be obtained. The advantages of the multiple fin rays configuration are:
 - an active control can be employed of the fin motion, thus a complex kinematic wave passing as observed from the bionic prototype can be realized accurately;

- a combination of the functional and morphology bionics can be achieved.

The drawbacks of the multiple fin rays configuration are:

- the achievable cruising speed is lower than the single fin ray configuration;
- the control logic is complex due to the complex structure.

Another classification involves the fin rays, which are grouped according to the kinematic joints employed:

- **Single-joint fin ray**, it permits only the mimicking of the chordwise wave propagation.
- **multi-joint fin ray**, it allows both the chordwise and spanwise wave propagation, usually thanks to a more complex mechanical systems and multiactuators.

The bionic design is based on the cownose ray morphology, but some necessary simplifications were necessary:

- the dimension of the cartilage were enlarged to make possible the accommodation of the driving mechanism.
- the upstroke and downstroke flapping motions have been considered with the same oscillation amplitude, in order to simplify the deformation of the bionic pectoral fin and to simplify the future control strategy for regulating the vertical motion, thus the depth of the robot.

Several fin rays would be needed to correctly mimic the kinematic waves transmitting in the chordwise direction. Intuitively, the number of fin rays depends on the wavenumber of the kinematic wave in chordwise direction. The number of rays increases as the wavenumber gets larger. To define the minimum number of fin rays necessary to correctly reproduce the passage of the kinematic wave, it is possible to make an analogy with the sampling of a signal. Indeed, the wavenumber represents the spatial frequency of the kinematic wave, while the number of samples is the sum between the number of fin rays and the control points at the front and the back of the fin base. Since there are only 0.4 waves present, a single fin ray would be enough to roughly mimic the kinematic wave. In

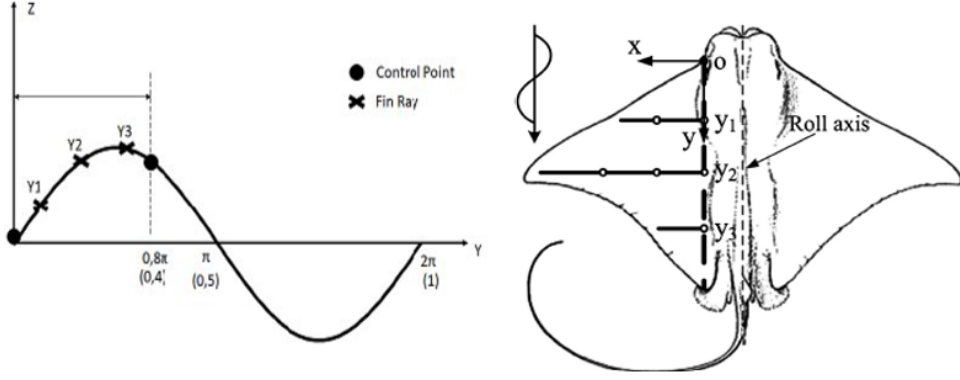


Figure 4.6: Number and distribution of the fin rays on the pectoral fin

order to guarantee a better mimicking of the chordwise wave transmission, three groups of fin rays have been chosen for the design of the bionic fin ray. Obviously, the spatial position of the three groups of fin rays affects the mimicking of the pectoral fin locomotion, especially the shape of the kinematics of the passing wave in chordwise direction. Thus, to define the spatial position of the fin rays an optimization method is employed. The goal of the optimization is to find the best position for the five control points, two on the fin base and three from the fin rays. The positions of the control points are grouped into a vector \tilde{y} :

$$\tilde{y} = (0, y_1, y_2, y_3, 1) = (\tilde{y}_1, \dots, \tilde{y}_5) \quad (4.2)$$

In order to find the optimal positions, a minimization of the residual area resulting from the superposition of the ideal target curve obtained from the cownose ray locomotion and the actual polyline curve drawn by the control points has been carried out. Let's assume that the chordwise kinematic wave is transmitted along the y-direction, from head to tail, following a sinusoidal discipline with a wavenumber N_c equal to 0.4, it can be expressed as:

$$f_{id}(y, k) = \sin\left(2\pi N_c y + \frac{2\pi, k}{N}\right) \quad (4.3)$$

where $f_{id}(y, k)$ is the sinusoidal-rule chordwise kinematic wave at the time instant k , N is the number of the samples in which the period T is discretized ($k = 1; \dots; N$), $N_c = 0.4$ is the wavenumber of the chordwise kinematic wave. Thus, the cost function e to be

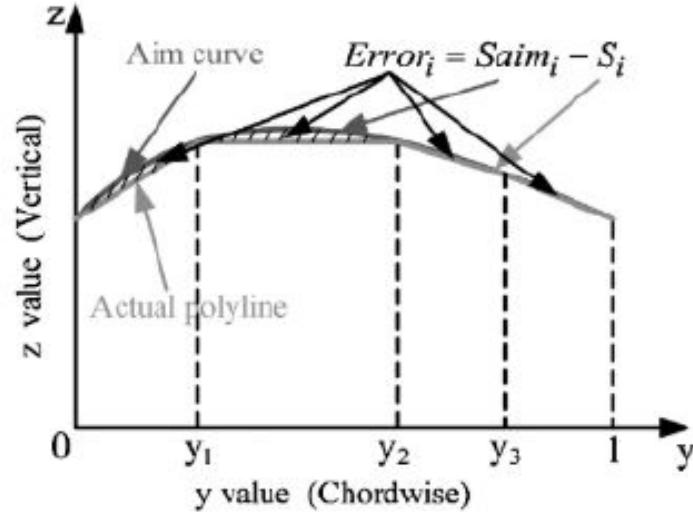


Figure 4.7: Minimum area optimization method to define the chordwise position of the fin rays

minimized is the sum of the residual area errors during a period T:

$$e = \sum_{k=1}^N |e^k| = \sum_{k=1}^N |A_{id}^k - A^k| \quad (4.4)$$

where A_{id}^k is the integral of the ideal target curve:

$$A_{id}^k = \int_0^1 f_{id}(y, k) dy \quad (4.5)$$

and A^k is the integral of the polyline curve of the control points:

$$A^k = \frac{1}{2} \sum_{i=1}^5 [f(\tilde{y}_i, k) + f(\tilde{y}_{i+1}, k)] (\tilde{y}_{i+1} - \tilde{y}_i) \quad (4.6)$$

The constraint equation of this optimization method is:

$$0 < y_1 < y_2 < y_3 < 1 \quad (\tilde{y}_1 < \tilde{y}_{i+1} \text{ for } i = 1, \dots, 5) \quad (4.7)$$

as the three fin rays are positioned on the fin base from the front to tail. The length of the fin base is set as unit 1. The result of the optimization of the fin rays position is:

$$\tilde{y} = (0, y_1, y_2, y_3, 1) = (0, 0.26, 0.5, 0.74, 1) \quad (4.8)$$

and it is shown in figure 4.8.

Three fin rays are almost uniformly distributed at the fin base along the chordwise direction (y-direction) of each side of the fish robot body.

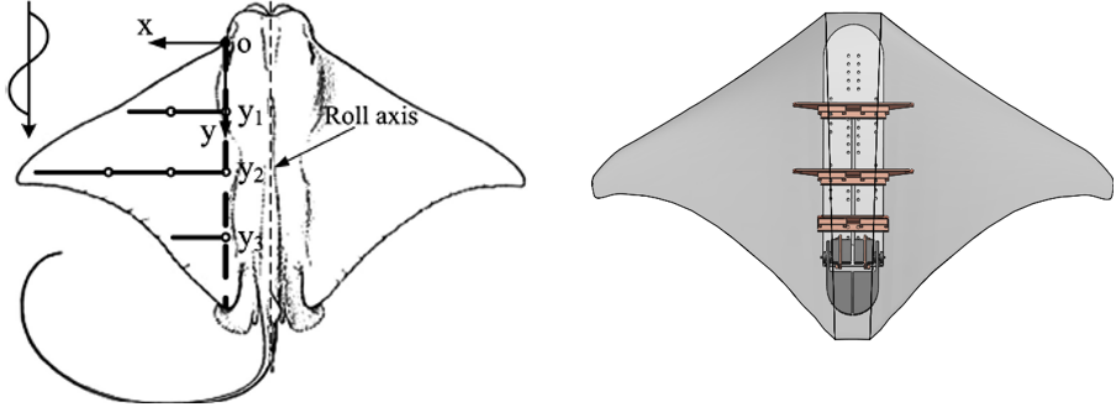


Figure 4.8: Result of the optimization of the fin rays position

The flapping motion involves a pectoral fin deformation in spanwise direction which can be mathematically expressed by:

$$h(s, t) = \frac{1 - \cos[\theta_0 \cdot s \cdot \sin(\phi r - \omega t)]}{\theta_0 \sin(\phi r - \omega t)} \quad (4.9)$$

where:

- ω is the frequency.
- ϕ is the number of waves ($\frac{2\pi}{\lambda}$),
- s is the curvilinear abscissa of the fin.
- θ_0 is the maximum angle of the tip of the fin.

The aim of the fin ray mechanism design is to mimic the flapping motion of the cownose ray up to the maximum amplitude by having as few as possible independent variables, in order to reduce the number of necessary servo-motors. Furthermore, the three designed fin rays (the front, the middle and the rear) must be driven by independent servo-motors, because the respective driven laws must account a phase time shift, which will be responsible of the chordwise kinematic wave. The kinematic synthesis can be performed

substantially in two different ways: direct synthesis and indirect synthesis. Among the direct synthesis methods, the only one that has a general application is that of *precision points*. In the design of the articulated systems, the limited number of available parameters does not allow the follower to follow the assigned motion law point by point, but it is only possible to reach a law that approximates the desired movement. The project is then carried out by imposing that the structural error remains below a certain tolerance. In the synthesis methods for precision points, the annulment of the structural error is imposed in correspondence with some predetermined configurations of the mechanism. The indirect synthesis methods, instead, require the repetition of a series of analyses with successive refinements until a satisfactory solution is reached. The refinement of the solution can be obtained with optimization techniques defining an objective function. As a rule, optimization techniques are forced when the number of design variables is high. In this case it is exploited minimization of the error between the motion of the middle bionic fin ray and the movements of the middle spanwise section of the pectoral fin of the animal. Thus, if the middle fin ray is able to reproduce the the required motion, the front fin and the rear will follow the same rule. The motions of the points on the bionic pectoral fin a compound movement characterized by a spanwise flapping and a chordwise sinusoidal wave transmission. In order to extract the time-varying spanwise deformation of the middle spanwise section of pectoral fin $(x; y_{middle})$, it is assumed a quasi-cubic behavior with time-varying coefficients. This fin deformation of the cownose ray must be mimicked by the motion of a bionic fin ray, positioned at the middle of the bionic pectoral fin. In order to design a mechanism which drives the bionic ray fin acting with quasi-cubic time-varying behavior, it is necessary to define four target points. Indeed, four points exactly fit a third degree polynomial equation. The relative distances among the target points represents the respective lengths of the links which form the mechanism. These quantities are grouped into a vector l_{links} :

$$l_{links} = (a, c, d) \quad (4.10)$$

The lengths of the links of the mechanism are depicted in Figure 4.9

Therefore, the goal is to design a driving mechanism which has only 1-DOF, which can be controlled by a servo-motor located on the central body of the fish robot. To do so, a

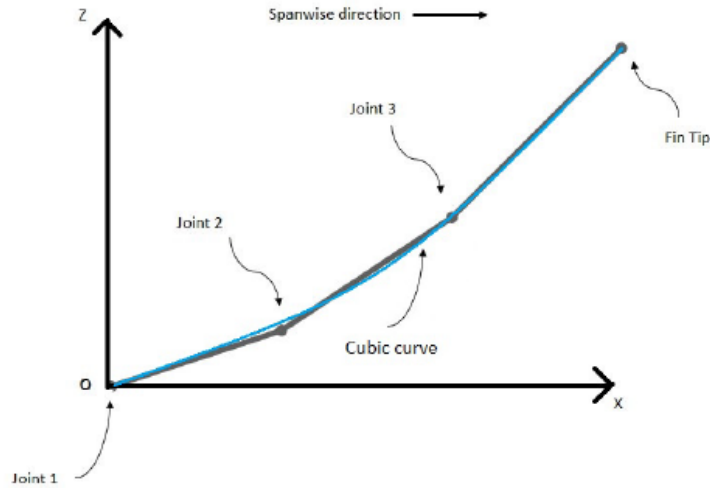


Figure 4.9: Scheme of the mechanism accountable for the motion of the bionic pectoral fins

more complex structure for the mechanism is proposed, which employ a 1-DOF two-stage slide-rocker mechanism for the middle bionic fin ray. At each time step of the pectoral fin motion, the two-stage slider-rocker mechanism of the middle fin ray has been verified to have motion law which minimize the error with the spanwise flapping quasi-cubic curves.

The structure of the three bionic fin rays is depicted in Figure 4.11:

- **Front fin ray:** one stage slider rocker mechanism
- **Middle fin ray:** two-stage slider rocker mechanism
- **Rear fin ray:** one linkage, an oscillating plate

The front and the rear fin rays dimensions have been designed in order to follow the triangular shape of the pectoral fin. To design the two-stage slider rocker three key points were taken as targets: the two rotating joints and the fin tip. The middle fin ray is composed by a two-stage slider rocker, as can be seen in Figure 4.10. The point O is the point in which the mechanism is hinged at the robot body chassis. h represents the distance between the ground hinge and the ground slider which connects the second link to the body chassis. a ; b ; c are respectively the length of the first, second and third link.

The trajectory of the first joint J1 is expressed by the time-varying position in the x-z plane of the point A, where $\alpha(t)$ is the angular coordinate of the first link. $\alpha(t)$ is the controlled coordinate of the mechanism, i.e the one driven by the servo thanks to the

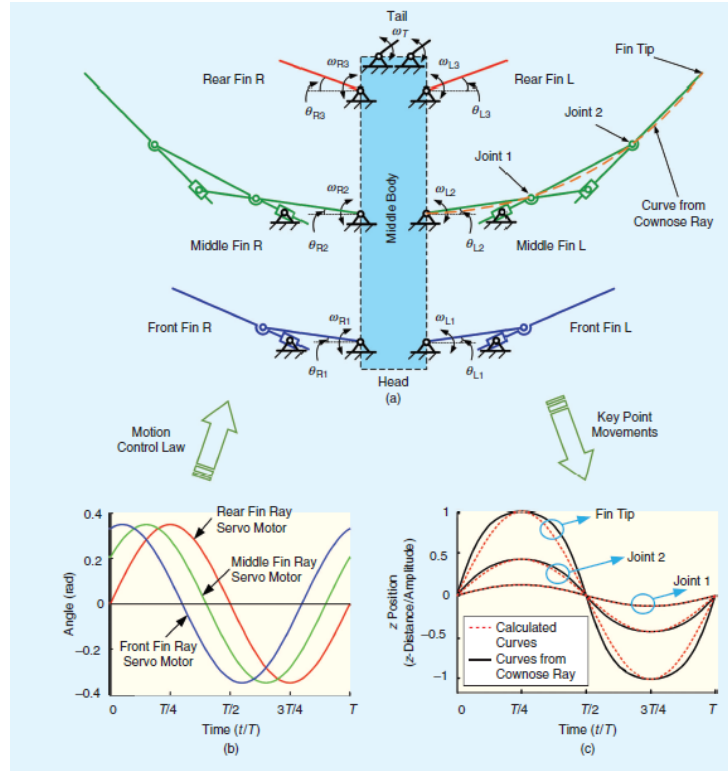


Figure 4.10: The kinematic analysis of the inside of the designed skeleton. a) The mechanism of the inside skeleton, b) the driving laws applied, and c) the movements of the key points

transmission system:

$$\begin{cases} x_A(t) = a \cos[\alpha(t)] \\ z_A(t) = a \sin[\alpha(t)] \end{cases} \quad (4.11)$$

The trajectory of the angular coordinate of the second link $\beta(t)$:

$$\beta(t) = \arctan\left(\frac{z_a(t)}{x_A(t) - h}\right) = \arctan\left(\frac{a \sin[\alpha(t)]}{a \cos[\alpha(t)] - h}\right) \quad (4.12)$$

The trajectory of the second joint J2 is expressed by the time-varying position in the x-z plane on the point B:

$$\begin{cases} x_B(t) = a \cos[\alpha(t)] + c \cos[\beta(t)] \\ z_B(t) = a \sin[\alpha(t)] + c \sin[\beta(t)] \end{cases} \quad (4.13)$$

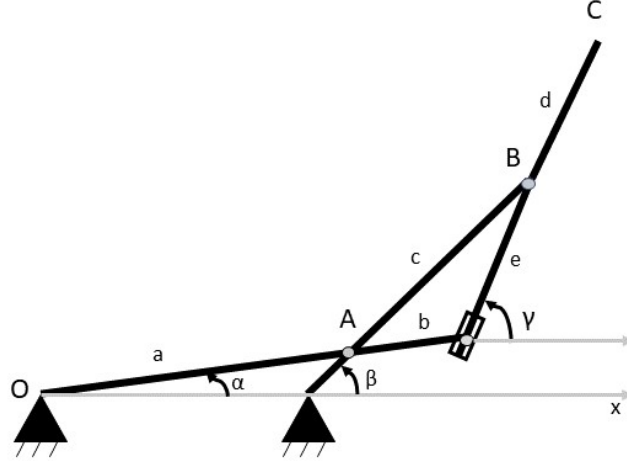


Figure 4.11: Scheme of two stage slider rocker mechanism employed as middle fin ray of the bionic pectoral fin

The trajectory of the fin tip is expressed by the time-varying position in the x-z plane:

$$\begin{cases} x_C(t) = a\cos[\alpha(t)] + c\cos[\beta(t)] + d\cos[\gamma(t)] \\ z_C(t) = a\sin[\alpha(t)] + c\sin[\beta(t)] + d\sin[\gamma(t)] \end{cases} \quad (4.14)$$

The trajectory of the angular coordinate of the third link is:

$$\gamma(t) = \arctan\left(\frac{c\sin[\beta(t)] - b\sin[\alpha(t)]}{c\cos[\beta(t)] - b\cos[\alpha(t)]}\right) \quad (4.15)$$

Since it was only possible to extract the trajectory of the target points $p_A(t) = (x_A(t), z_A(t))$ in order to define the dimension of the linkages of the mechanism and the relative position of the ground and internal constraints, an optimization method is used. The optimization is aimed at the minimization of the error between the actual and the desired trajectories of the fin.

Table 4.1: Dimensions of the linkages of the mechanism of the middle bionic fin ray

Linkage	Length[m]
a	0.158
b	0.055
c	0.11
d	0.11
e	0.68

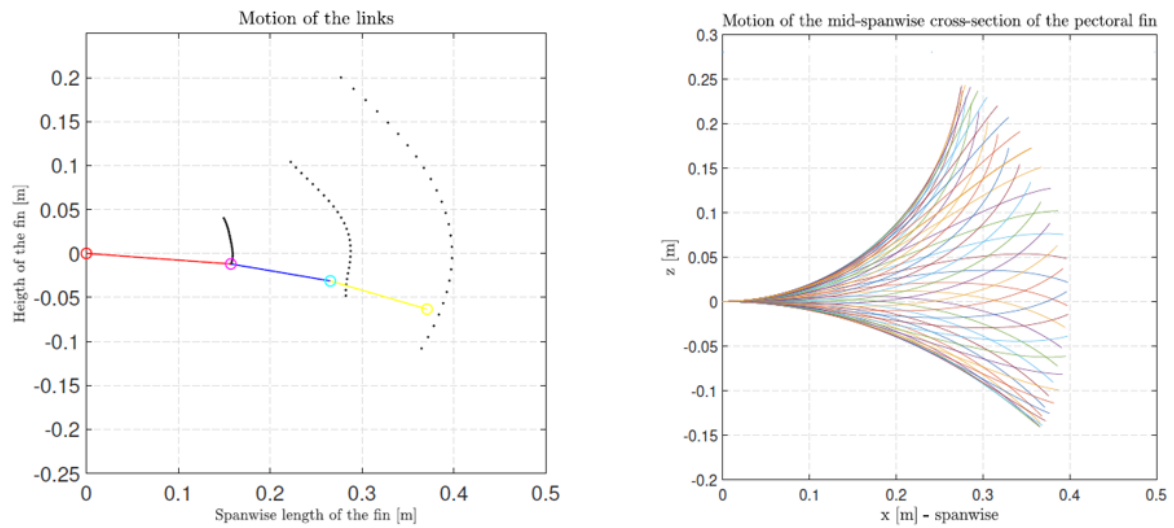


Figure 4.12: Scheme of the mechanism accountable for the motion of the bionic pectoral fins/ deformed profile of the fin spanwise cross section

With the same procedure also the front fin ray and the rear fin ray's kinematic synthesis was developed, obtaining the mechanisms shown in fig.4.13. There are different

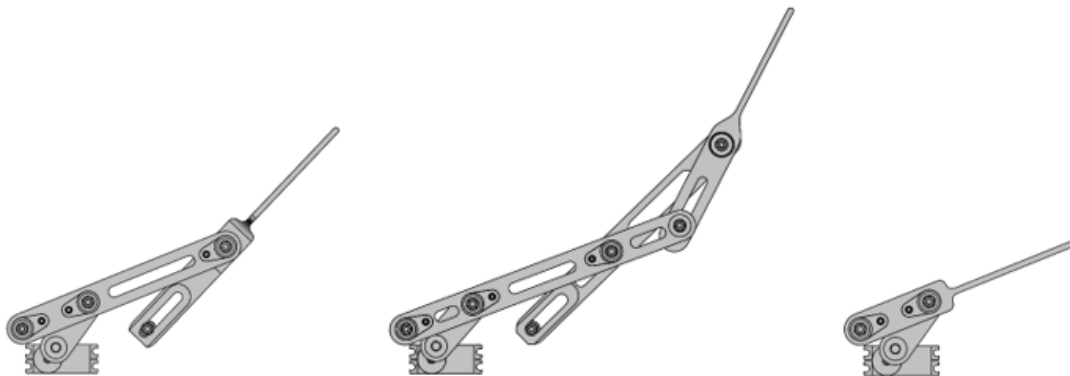


Figure 4.13: a) Scheme of the mechanism of the front fin b) Scheme of the mechanism of the middle fin c) Scheme of the mechanism of the rear fin

approaches to generate movement but the one chosen in this project is to take movement from a motor with constant angular velocity and transform it by means of a mechanical transmission. The front, the middle and the rear bionic fin rays are driven independently by three servo-motors. The servos are not directly connected to the bionic fin rays mechanisms, i.e. the power transmission is made possible thanks to a transmission system. Since the first link of the bionic fin ray mechanism must be driven by a sinusoidal law,

it is necessary to design a mechanism which transform the unidirectional rotational motion of the servo-motor $\theta_{servo}(t)$ into an sinusoidal rotational motion of the first link of the mechanism $\alpha_{des}(t)$. Thus, a systematic design of the mechanism is carried out. To identify the best kind of mechanism for the given task, the type synthesis is carried out following the table below: A four-bar linkage is thus employed to transform the unidirectional rota-

Table 4.2: The table used to perform the type synthesis

Motion transformation	Best kind of mechanism
Transmit circular motion	4 bar linkage(parallelogram)
Unidirectional rotational motion to alternate rotational motion	4 bar linkage, slider crank with yoke
Unidirectional rotational motion to alternate linear motion	Slider crank mechanism
Follow a path	4 bar linkage (1 DOF), 5 bar linkage (2 DOF)
Quick return mechanism	Slider crank, 4/6 bar linkage

tional motion of the servo into an alternate rotational motion. The dimensional synthesis

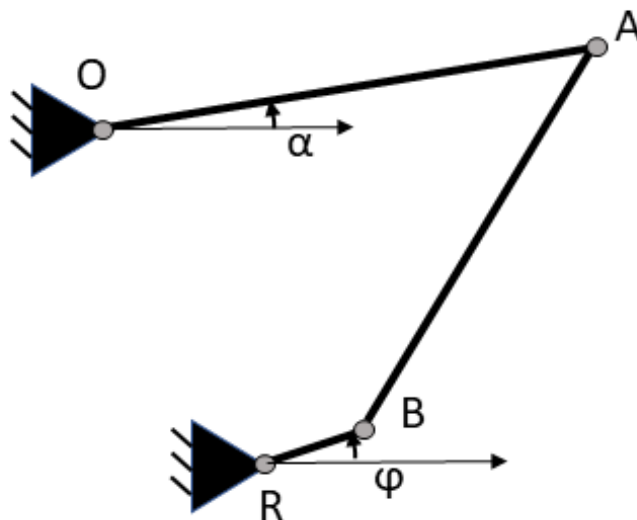


Figure 4.14: 4 bar mechanism.

defines the positions of the joints, the link lengths and the main geometrical features of the mechanism. The goal is to synthesize the four bar mechanism as a function generator: the unidirectional rotational motion of the link $R B$ driven by the servo-motor $\theta_{servo}(t)$, must be correlated to the alternate rotational motion of the first link $O A$ of the bionic ray fin γ_{des} . The desired alternate rotational motion of the first link of the bionic fin ray

$\alpha_{des}(t)$, measured in [deg], has a sinusoidal rule:

$$\alpha_{des}(t) = \phi_{max} \sin \theta_{servo}(t)$$

where ϕ_{max} is the maximum angular position of the first link of the bionic fin ray mechanism. The unknown variables of the problem the linkages dimensions a, b, c and the relative position of the two ground hinges R (servo-motor position) and O (ground hinge of the first link of the bionic fin ray). The synthesis has been obtained thanks to a numerical optimization method, which imply the assignment of precision points and the minimization of a cost function CF related to the structural error $e_i = \alpha_i - \alpha_{des,i}$ of the mechanism:

$$CF = \sum_{i=1}^N (\alpha_i - \alpha_{des,i})^2 \quad (4.16)$$

where N is the number of desired angular position $\alpha_{des,i}$ of the first link of the bionic fin ray. The cost function CF is related to the sum of the squared distances between the desired angular positions and the actual ones for every prescribed crank positions. The

Table 4.3: Dimension of the linkages of the four-bar mechanism, which drives the bionic fin rays

Linkage	Length[m]
Crank $R - B$	0.01
Connective rod $B - A$	0.04
Rocker $O - A$	0.051
Ground hinges distance $R - O$	0.049

transmission mechanism obtained from the optimization process can be seen in the figure 4.15

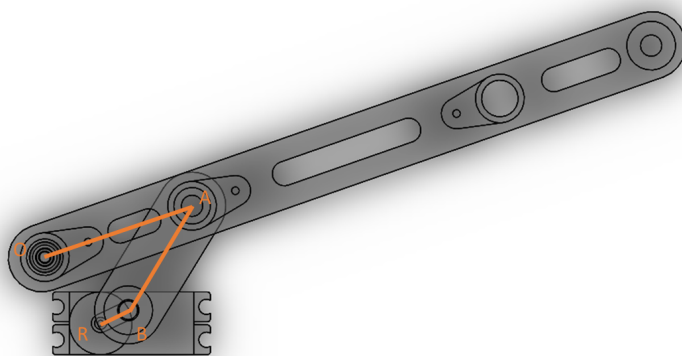


Figure 4.15: Final transmission mechanism.

and allows to transform the unidirectional motion of the motor into an alternating motion between two dead points. Every single part of the mechanism has been created using additive manufacturing, the process of joining materials to make objects from 3D model data, usually layer upon layer, as opposed to subtractive manufacturing methodologies.

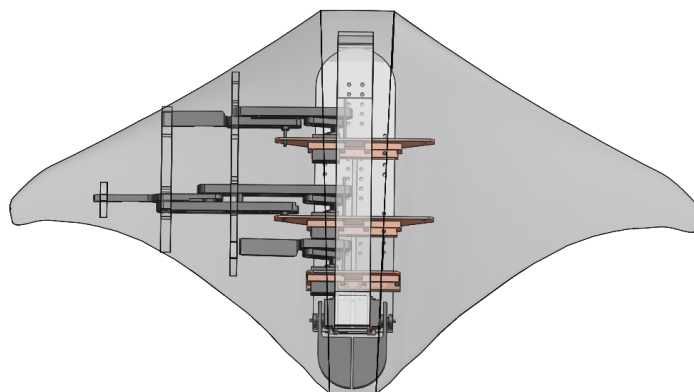


Figure 4.16: Schematic representation of the mechanisms in series .

4.3 Tail

Another important simplification introduced in the robot design is the tail. Manta Ray just like their sting ray cousins have a long whip like tail that plays no role during the swimming. Instead it is able to balance itself during complex motions thanks to the pec-

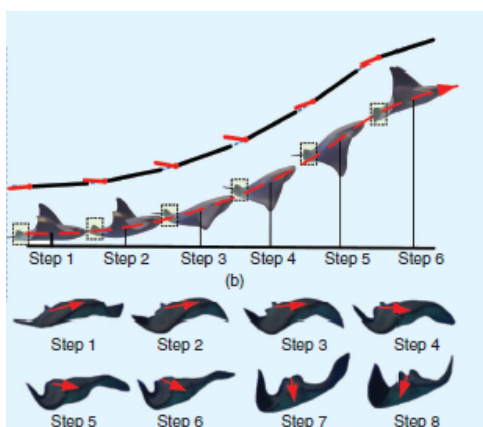


Figure 4.17: The motion discipline analysis of the cownose ray and the role of the tail during swimming.

toral fins which therefore guarantee both movement and balance. Due to the complexity

of the movements of the fin, a tail has been introduced which, properly controlled, acts like lift rudders, assisting the pectoral foils in floating and submerging ensuring balance as shown in Fig. 4.17.

The tail being formed by two rudders (Fig. 4.18) is also useful during the turning phase in the horizontal plane by reducing the radius of curvature.

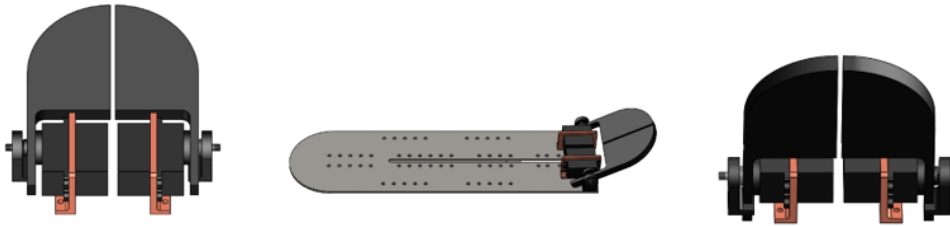


Figure 4.18: Design of the Manta's tail

Thanks to the kinematic synthesis, the shape analysis and the simplifications introduced to obtain the desired movement, the final design that best replicates the characteristics of a Manta is designed (Figure 4.19).

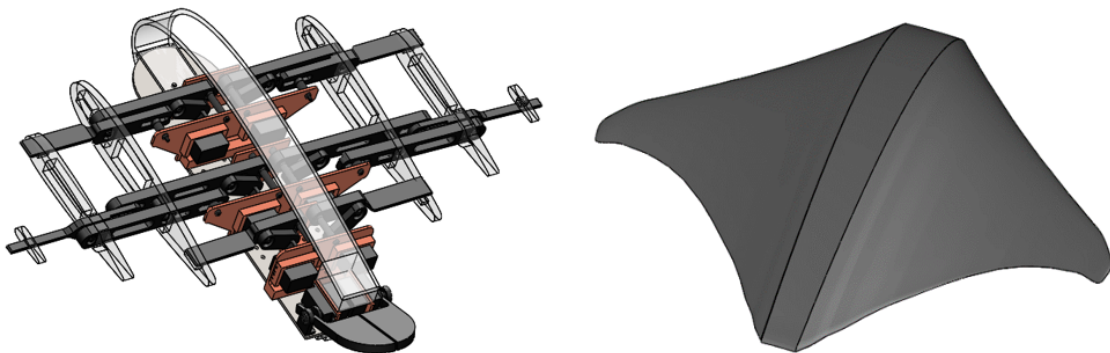


Figure 4.19: Final 3D robot design

Chapter 5

3D Analysis Of Manta Robot

5.1 Multibody

The multibody analysis was implemented in order to study the dynamic behaviour of interconnected flexible or rigid bodies, when each of them undergoes large translational and rotational displacement. For doing that, the use of an add on of Matlab called Simmechanics that works with Simulink is fundamental. After the mechanism synthesis and after the choice of dimensions and shape of the links, the system is imported from Solidworks into this new environment.

3D Kinematics:

First of all, it is of great importance the choice of the reference systems which relates different solids. Every solid needs to be properly put into the scheme with a proper reference and a proper location. In order to do so, global refence systems and local reference systems must be distinguished. Considering an unconstrained rigid body moving in 3D space, the body itself has got six degrees of freedom. With respect to a fixed (global) reference system, at any time t , the position of the body can be uniquely identified making reference to the following six independent coordinates:

- three independent coordinates $x^G y^G z^G$ to define the position of an arbitrary point O on the body with respect to the global reference(G).
- three independent coordinates to define the angular position of the body (i.e. of the local reference system rigidly linked to the body) with respect to the global reference.

As for the body angular position, different sets of coordinates are commonly adopted. As an example, it is considered Cardano angles convention: it consist of three consecutive rotations executed in given sequence: they define the angular position of the body (local) reference system with respect to the global one. Note that the sequence of rotations chosen is significant.

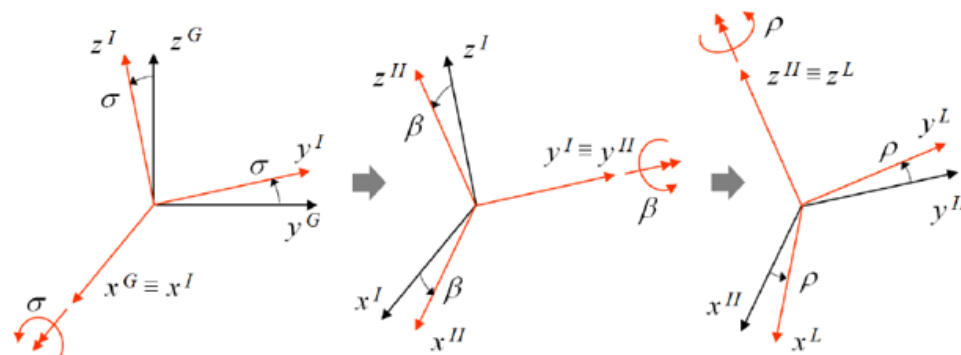


Figure 5.1: Example of subsequent rotations along x,y and z axis respectively.

Considering a generic vector 'a' whose components in the global reference system are collected in a column matrix a^G . The components a^L of the same vector in the local reference system can be related to the previous ones by introducing a proper rotation matrix $[\Lambda_{LG}]$ so that:

$$a^L = \Lambda_{LG} \cdot a^G \quad (5.1)$$

The rotation matrix Λ_{LG} depends on the orientation of L with respect to G and can be expressed as a function of Cardano angles, for example. It is obtained as the product of three matrices, each one corresponding to a single rotation in the adopted sequence.

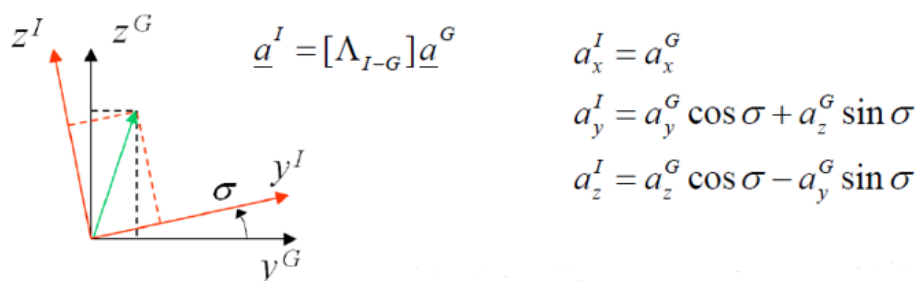


Figure 5.2: Rotation about x^G .

It is possible to define the other two subsequent rotations:

$$a^{II} = [\Lambda_{II-I}]a^I \quad [\Lambda_{II-I}] = \begin{bmatrix} \cos\beta & 0 & -\sin\beta \\ 0 & 1 & 0 \\ \sin\beta & 0 & \cos\beta \end{bmatrix} \quad (5.2)$$

$$a^L = [\Lambda_{L-II}]a^{II} \quad [\Lambda_{L-II}] = \begin{bmatrix} \cos\rho & \sin\rho & 0 \\ -\sin\rho & \cos\rho & 0 \\ 0 & 0 & 1 \end{bmatrix} \quad (5.3)$$

By combining the three equations above:

$$a^L = [\Lambda_{L-II}]a^{II} = [\Lambda_{L-II}][\Lambda_{II-I}]a^I = [\Lambda_{L-II}][\Lambda_{II-I}][\Lambda_{I-G}]a^G \quad (5.4)$$

Note that the three single planar rotation matrices are orthogonal. Actually, transposing one single planar rotation matrix corresponds to reversing the direction of the rotation itself.

Position matrix:

Let consider two coordinate systems (0) and (1) and describe the position of a point P with respect to them. Using matrix representation referred to a generic coordinate system(i):

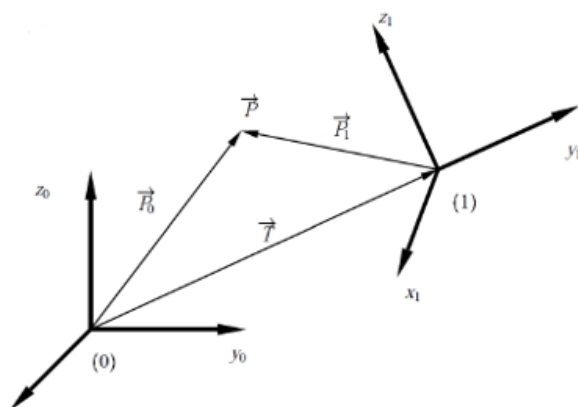


Figure 5.3: Position of point P.

$${}^3P_{0(i)} = T_{(i)} + {}^3P_{1(i)} \quad (5.5)$$

Usually P_0 and T are known in (0) whilst P_1 is known in (1):

$${}^3P_{0(0)} = {}^3T_{(0)} + {}^3P_{1(0)} = {}^3T_{(0)} + R_{01}^3 P_{1(1)} \quad (5.6)$$

Using the homogeneous coordinates, one can write the previous expression in a compact form:

$$P_{0(0)} = M_{01} P_{1(1)} \quad (5.7)$$

Where:

- M_{01} is called position matrix of the coordinate system (1) with respect to (0). This allows to convert the coordinates of a point from a coordinate system to another.
- R_{01} describes the angular position between the two coordinate systems λ_{LG} .
- T_0 is the position of origin (1) with respect to the coordinate system (0).

When considering a robot or a mechanism a coordinate system must be fixed on every element. Using the properties of the pose matrices one can combine M_{ij} in order to obtain the transformation matrix that allows one to describe the end position of a system made of n elements with respect to the base one (0).

$$M_{0n} = M_{01} M_{12} \dots M_{i-1} M_i M_{i+1} \dots M_n \quad (5.8)$$

Once the positions of the coordinate systems and the transformation matrices have been defined it is possible to calculate the robot kinematics. It is necessary to know the position of the end of each mechanism according to the joint coordinates of the motors.

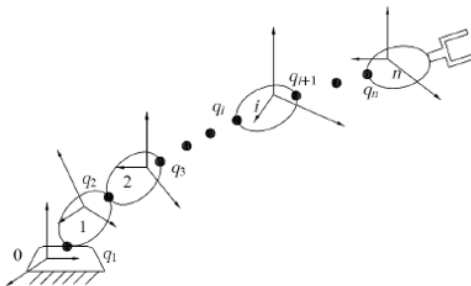


Figure 5.4: Example of transformation process in an arm robot with n reference systems.

Velocity and Acceleration matrices:

It is known that the velocity of a point of a body can be expressed as Rivals theorem:

$${}^3V_{p(i)} = {}^3V_{0(i)} + \omega_{(i)}^3 P_{(i)} \quad (5.9)$$

Developing the matrix equation as before for the position matrix M_{ij} :

$$\begin{bmatrix} v_{px} \\ v_{py} \\ v_{pz} \\ 0 \end{bmatrix} = \begin{bmatrix} 0 & -\omega_z & \omega_y & v_{0x} \\ \omega_z & 0 & -\omega_x & v_{0y} \\ -\omega_y & \omega_x & 0 & v_{0z} \\ 0 & 0 & 0 & 0 \end{bmatrix} \cdot \begin{bmatrix} x_p \\ y_p \\ z_p \\ 1 \end{bmatrix} = \dot{P}_{i(i)} = W_{(i)} P_{i(i)} \quad (5.10)$$

where:

- W is the velocity matrix of the body, because it allows one to calculate the velocity of any point of such body. It depends on the reference system and the origin of such system is the point with respect to which the velocity is evaluated.
- \dot{P} is the velocity vector.

Accordingly, a relationship that links the velocity matrices expressed in the two frames should exist:

$$W_{(i)} = M_{ij} W_{(j)} M_{ji} \quad (5.11)$$

The same is applied for the accelerations:

$${}^3A_{p(i)} = {}^3A_{0(i)} + \dot{\omega}_{(i)} \cdot {}^3P_{(i)} + \omega_{(i)}^2 \cdot {}^3P_{(i)} \quad (5.12)$$

Developing the matrix equation as before for the velocity matrix W_{ij} :

$$\ddot{P}_{i(i)} = H_{(i)} P_{i(i)} \quad (5.13)$$

where:

- H is the acceleration matrix of the body and \ddot{P} is the acceleration vector.

Kinetostatic duality:

Another important concept to be underlined is the kinetostatic duality; from theory it is known that a relationship between joint space and workspace coordinates exists:

$$\begin{array}{ccc}
 S = \begin{bmatrix} s_1 \\ s_2 \end{bmatrix} = \begin{bmatrix} x_p \\ y_p \end{bmatrix} & \begin{array}{c} \xleftarrow{\text{Forward kinematics } S = F(Q)} \\ \xrightarrow{\text{Inverse kinematics } Q = F^{-1}(S)} \end{array} & Q = \begin{bmatrix} q_1 \\ q_2 \end{bmatrix} = \begin{bmatrix} \alpha \\ \beta \end{bmatrix}
 \end{array}$$

From the study of this coordinate relationship it is possible to move to velocity and acceleration case through a derivation process, in fact:

$$S = F(Q) \rightarrow \dot{S} = \frac{\delta F}{\delta Q} \dot{Q} = J \dot{Q} \rightarrow J = \frac{\delta F}{\delta Q} \quad (5.14)$$

Where J is called Jacobian matrix and depends on the position of the fin. The same applies for the accelerations, one can derive the velocity equation obtaining:

$$\ddot{S} = \dot{J} \dot{Q} + J \ddot{Q} \quad (5.15)$$

The problem could be solved in the opposite case if the matrix J is invertible and so the inverse kinematics can be solved. Note that the matrix J could be singular so its determinant is zero, than during the inversion process J^{-1} tends to infinite. This particular property that depends on position is called "singularity configuration" and has strange effects on the mechanism. Focusing on the principle of virtual work:

$$F_s^T \delta S + F_q^T \delta Q = 0 \quad (5.16)$$

and substituting $\delta S = J \delta Q$ we get:

$$F_s^T J + F_q^T = 0 \quad (5.17)$$

The so called kinetostatic duality is obtained that is a property of a system that establish

a relationship between kinematics and dynamics of the system.

$$\begin{cases} F_q = -J^T F_s \\ \dot{S} = J\dot{Q} \end{cases} \quad (5.18)$$

In facts within a singularity configuration a small force in the workspace could produce infinite torque in the joint space and vice versa so it must be avoided. Reference systems could be used either to connect different links in a specified position like the centre of mass, the reference origin or based on a geometric figure or to apply external forces and torques; the same happens for the actuation system in correspondence of motors revolute joint. This is a powerful tool to match up data obtained from other software. Figure 5.5 shows the large number of reference systems that must be put into a multibody since it is of fundamental importance that all the link respect constraints, movement and distances with respect to others:

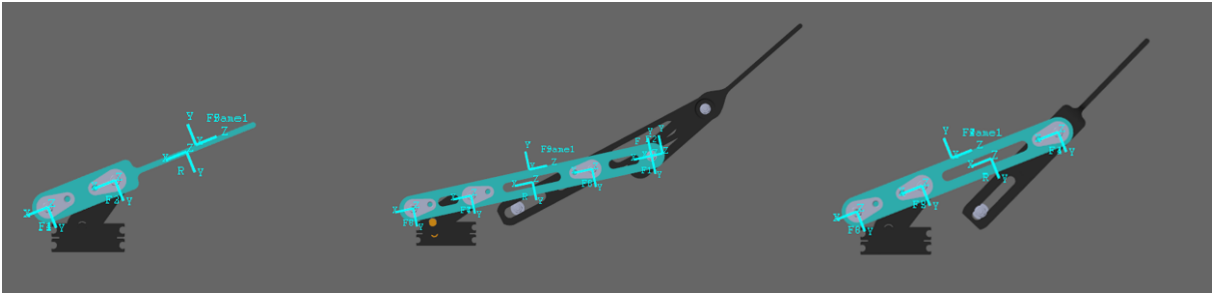


Figure 5.5: Reference systems on the Manta's mechanisms.

Joints:

Introduction of joints allows to establish the movement between two links which are called ‘base’ and ‘follower’. The ‘base’ is the reference one, the ‘follower’ is the one that follows the base. There are a lot of types of joint among which: planar, prismatic, spherical, revolute, cylindrical, bearing and universal which were used in the scheme of the multibody.

- A planar joint has two translational and one rotational degrees of freedom represented by two prismatic primitives and one revolute primitive along a set of three mutually orthogonal axes. This joint constrains the z-axes of the base and follower frames to be aligned and prohibits relative translation along that axis. It allows

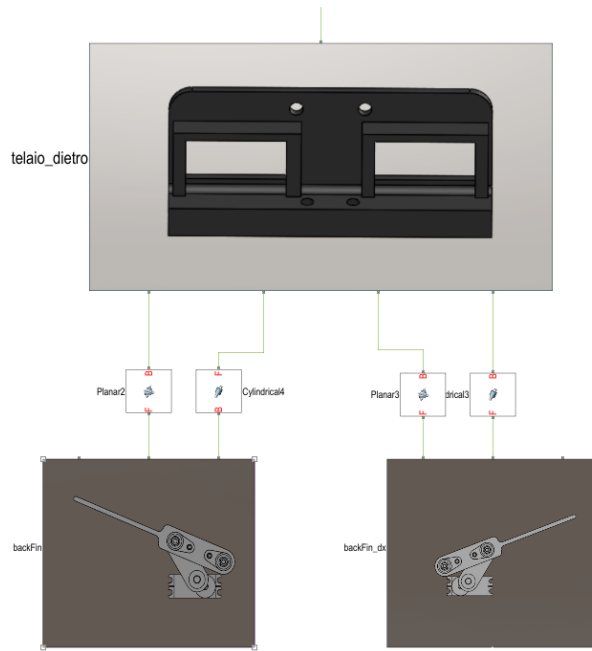


Figure 5.6: Example of joints in the rear of the robot.

translation of the follower origin in the base xy-plane and rotation of the follower frame around its z-axis.

- A revolute joint has one rotational degree of freedom represented by one revolute primitive. The joint constrains the origins of the two frames to be coincident and the z-axes of the base and follower frames to be coincident, while the follower x-axis and y-axis can rotate around the z-axis.
- A spherical one has three rotational degrees of freedom represented by one spherical primitive. The joint constrains the origins of the two frames to be coincident. The follower frame rotates freely around this common origin as the pivot.
- A cylindrical one has one translational and one rotational degree of freedom represented by one revolute primitive and one prismatic primitive coincident along the same axis. This joint allows only rotation and prohibits relative translation in the base xy-plane. The follower frame first rotates about the base z-axis and then the follower origin translates along the base z-axis.
- A cartesian one has three translational degrees of freedom represented by three prismatic primitives along a set of mutually orthogonal axes. This joint constrains the axes of these frames remain aligned, while allowing unconstrained 3-D translation.

Once that all links are set it is possible to observe the motion of mechanisms, the multi-body were used to test synthesis of mechanisms to verify that all joints have been selected properly and with proper reference systems connection. Another important check is that links motion is coherent with respect to the movement of the fish as studied in the previous chapters.



Figure 5.7: Test of proper construction idea of right central fin.

3D Dynamics:

Multibody simulation techniques have a systematic approach for deriving and solving non-linear motion equations of 3D mechanical systems made of interconnected rigid/flexible bodies which undergo large displacements and rotations. Focus of the study is now on dynamics. It is possible to divide dynamics in two categories: linear and rotational dynamics:

- Linear dynamics regards object moving in a line and involves quantities as force, mass, inertia, displacement, velocity, acceleration and momentum.
- Rotational dynamics regards object rotating or moving in a curved path and involves quantities such as torque, moment of inertia, angular displacement, angular velocity, angular acceleration and angular momentum.

The problem is to evaluate all forces involved into the system in order to create a unique system capable of describing as much as possible the real case. For doing that the dynamic study is divided into two parts:

- mechanics interactions between electric motors and structure
- fluid-dynamics interaction between robot and water.

For what concern mechanism interaction forces and torques it is made use of Simmechanics that allows to calculate, plot and process data of mechanics interactions.

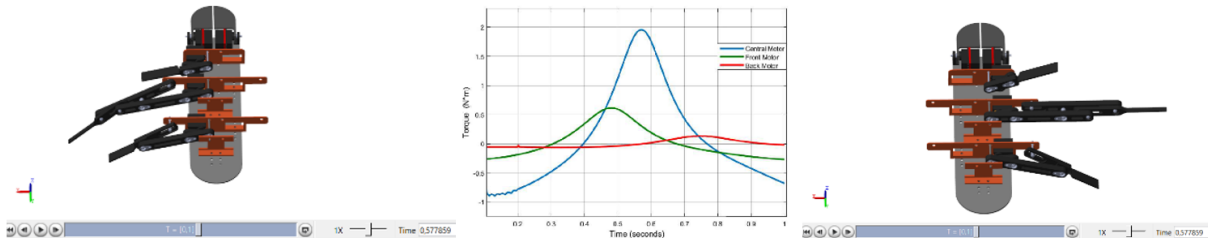


Figure 5.8: Study of mechanism interaction forces and torques.

For what concern fluid dynamics interaction forces and torques it is made use of a CFD simulation, analyzed with Paraview that allows to calculate, plot and process data of fluid interactions.

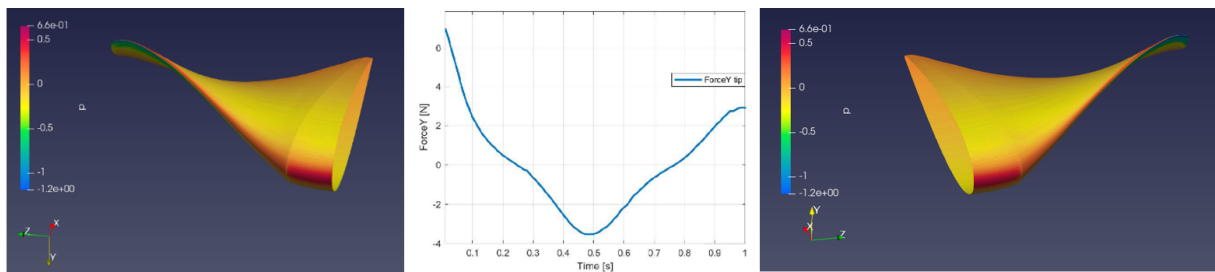


Figure 5.9: Study of fluid dynamics interaction forces and torques.

The aim of this kind of study is to match up results from CFD simulation and bring them into mechanism simulation in order to better replicate the environment in which the MantaRobot will be.

Starting with the definition of the problem, it is indicated with n the number of degrees of freedom and we collect the Manta's independent coordinates in the following column matrix:

$$x = \begin{bmatrix} x_1 \\ x_2 \\ \vdots \\ x_n \end{bmatrix} \quad (5.19)$$

note that in general the choice of the set x of independent coordinate is non-unique. The Lagrange's equations is written:

$$\frac{d}{dt} \left(\frac{\delta T}{\delta \dot{x}_k} \right) - \frac{\delta T}{\delta x_k} + \frac{\delta D}{\delta \dot{x}_k} + \frac{\delta V}{\delta x_k} = Q_k \quad k = 1, 2, \dots, n \quad (5.20)$$

where:

- T is the kinetic energy of the system.
- D is the dissipation function.
- V is the potential energy.
- Q is the generalized active force over the independent coordinate x_k , this equation represents the system's -n independent motion equations.

Considering the equation of motion of the system it is possible to notice that the inertia terms play an important role in the dynamics of a body. Looking at the equation of the kinetic energy T two contributions can be seen: a translational one related to the mass [m] and a rotational one related to the inertia [J_G]:

$$T = \frac{1}{2}v_G^{G^T} [m]v_G^G + \frac{1}{2}\omega^{L^T} [J_G]\omega^L \quad (5.21)$$

The formula above is known as the Konig theorem. It represents the kinetic energy of a rigid body in the case of 3D kinetics (the generalization of the analogous formula for in-plane motion). Note that the inertia tensor [J_G] varies with the choice of the rigid body local reference system. Whatever the shape and the mass distribution of the body itself, it is always possible to identify one preferential Cartesian coordinate system (rigidly linked to the body) which results in [J_G] being a diagonal matrix (i.e. all products of inertia are zeroes). In our case all the inertia and mass terms are taken from the 3D cad which automatically sets all the parameters related to the materials. Lagrange equations relate the active forces applied to the system's acceleration, velocity and position. The generalized force Q_k over the k-th independent coordinate is obtained as the ratio between the virtual work made by all active forces as a result of the system virtual displacement corresponding to a virtual increment of the k-th independent coordinate alone divided by dx_k . Basically, all dimensions set in the mechanism synthesis are tested in a 3D multibody environment capable of solving the equation of motion of the robot which will interact with external forces and torques. This will give a realistic estimate of magnitudes of the external forces applied on our system and the motion of the system itself. To move on, all external forces and toques can now easily be put into our system in order to solve dynamics in a very easy way and to evaluate on every reference system how much are

displacements, velocities, accelerations, forces and torques. As an example, it is known that the robot interacts with fluids so the fluid dynamic interaction must be added. Note that just forces on YZ and torques on XZ directions are considered, because they influence actively the motor's torque requested.

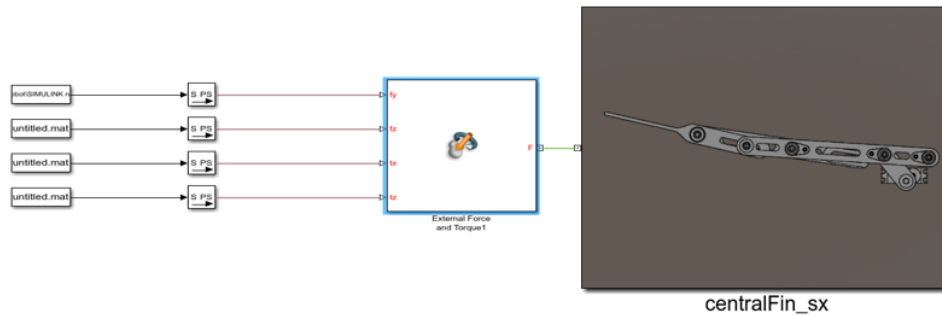


Figure 5.10: Data representing external conditions from Matlab into Simulink's Multibody.

The simulation starts with the Manta with an external constant force directed as Y (downward) of 10 N of magnitude distributed along three mechanisms. Motion of the revolute joint is imposed at 2 rad/s. Torque needed to perform it is obtained.

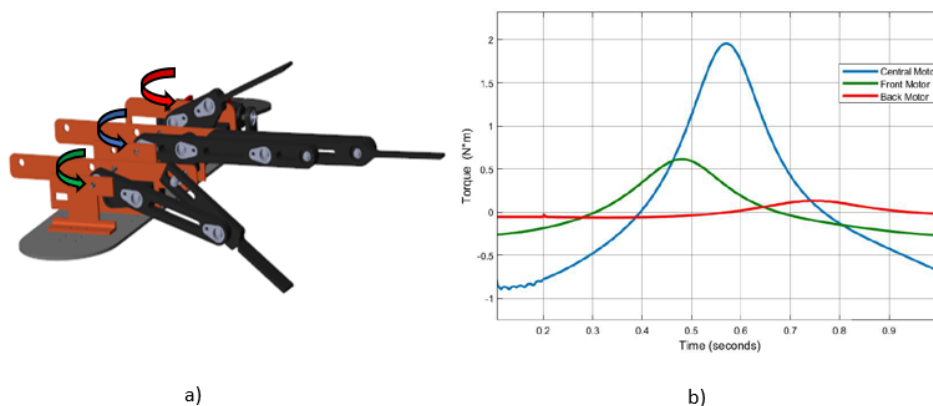


Figure 5.11: a) phase lag between fins. b) plot of motor torque needed when external constant force applied

As can be seen, with an external constant force of 10N distributed along three mechanisms the maximum torque needed by the motor for doing a complete rotation in a second is at most 2 Nm for central motor, 0.5 Nm for the front one and quite negligible for the back

one. The last step is to introduce the whole system and prepare the space for the data obtained from computational fluid dynamic research. The choice of position of external forces and external torques will be clarified in the following section. After that, a proper sizing of motors and an explanation on how external forces interact with the robot are given.

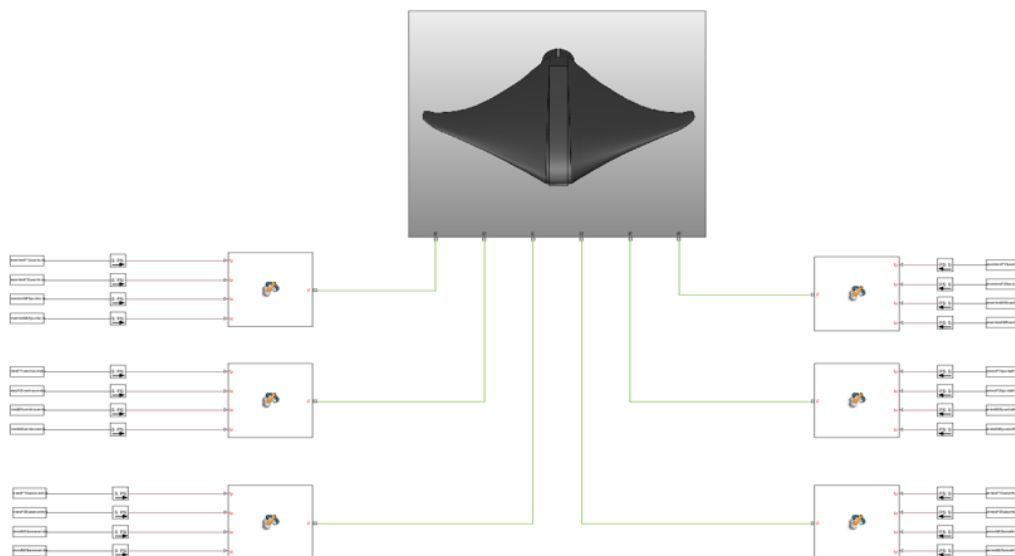


Figure 5.12: Block diagram of the whole robot system with time variant external forces to be taken from cfd.

From Figure 5.12 it could be noted that 12 forces and 12 torque have been selected to better describe the distribution of those on the surface of the Manta Robot:

- Front Fin (two parts): 4 forces and 4 torques
- Central Fin (three parts): 6 forces and 6 torques
- Back fin (single part): 2 forces and 2 torques

The selected one are those representing force in Y and Z directions and those of torques in X and Z directions.

5.2 CFD

First of all is exploited the Computational Fluid-Dynamics that uses numerical analysis to analyse and solve problems that involve fluid flows. Calculations are used to simulate the interaction between the fluid and the surface defined by boundary conditions. The CFD tools is very used nowadays in most of the engineering problem which involve aerodynamics and aerospace analysis, weather simulation, environmental engineering and industrial system analysis. To visualize the result the program "Para-View" was used ,which is an open source multi-platform data analysis and visualization application. Para-View users can quickly build visualizations to analyse data using qualitative and quantitative techniques. The data exploration can be done interactively in 3D or programmatically using data processing capabilities.

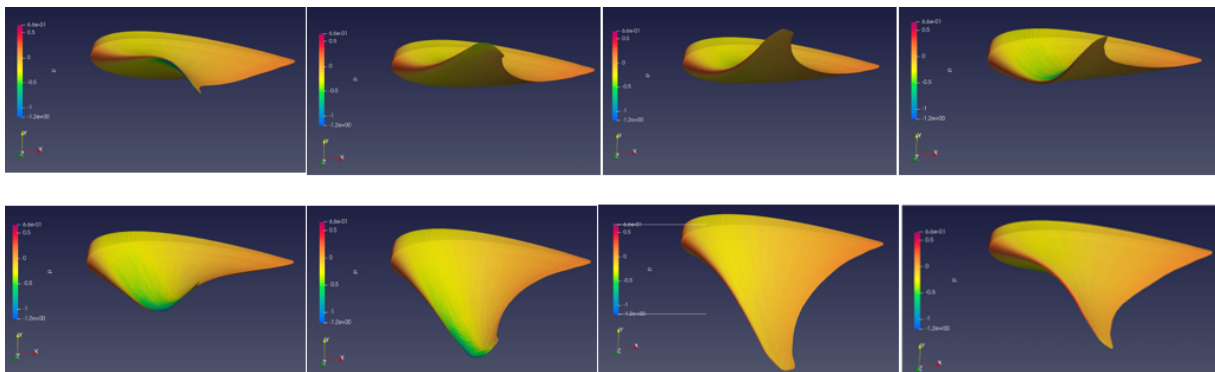


Figure 5.13: CFD study of the complete movement of the left fin of the manta.

Data Setting and parameters:

the domain of simulation is a parallelepiped of dimensions:

$$X : -3m \rightarrow 2m$$

$$Y : -2m \rightarrow 2m$$

$$Z : 0m \rightarrow 2m$$

The manta is located in the origin of the axes and its head is directed as -x. The simulation is 3D and exploits the symmetry between the two fins, only half of the manta body has been considered and on the $z = 0$ plane, boundary conditions of the type: symmetry plane have been imposed. The mesh was generated using six refinement levels around the surface of the manta ray and is made up of 1005416 cells. The simulation concerns the motion of an incompressible, turbulent, non-stationary fluid, with a moving mesh, the

solver used is pimpleFoam. The deformation of the mesh has been imposed and follows the deformation of the fin. The only movement present in this simulation is the movement of the fin, the body of the manta remains fixed, the progress of the manta is simulated by imposing a speed on the fluid in opposite direction. Therefore, to simulate the progress of the fish at 1 m/s in the $-x$ direction, an undisturbed flow speed of 1 m/s in the $+x$ direction is set. Boundary conditions are imposed as follows:

- **Speed:** 1 m/s in the $+x$ direction on the inlet surface of the domain (plane $x = -3m$), equal the speed of the fluid on the surface of the manta;
- **Pressure:** 0 $\frac{Pa}{\frac{Kg}{m^3}}$ on the outlet surface of the domain (plane $x = +2m$). (The pressure unit of measurement is given by the fact that all equations are divided by density since the fluid is incompressible, it is the same reason why we multiply all the forces we calculate by 1000 $\frac{Kg}{m^3}$).

The model used to simulate turbulence is k- ω SST, with the following parameters:

- $K = 0.0015 \frac{m^2}{s^2}$
- $\omega = 2.55 s^{-1}$

The kinematic viscosity is that of water at room temperature, i.e. $1e^{-6} \frac{m^2}{s}$.

The fin motion law has the following parameters:

- $\omega = 2\pi \frac{rad}{s}$ (frequency)
- $\phi = 5.02 \frac{rad}{m}$ (number of waves)
- $\theta_0 = \frac{\pi}{3} rad$ (maximum width of the movement on the tip)

Slicing:

This kind of environment should replicate what happens in real case. The CFD study give us the total pressure distribution over the surface in contact with the fluid. The idea is to split the total surface into subparts, evaluate in each part how is the distribution of forces and torques along active directions and evaluate resultants in the barycentre of these parts. Once resultants are found they have been extracted from the simulation of a complete movement of the fin with constraints given in previous chapter.

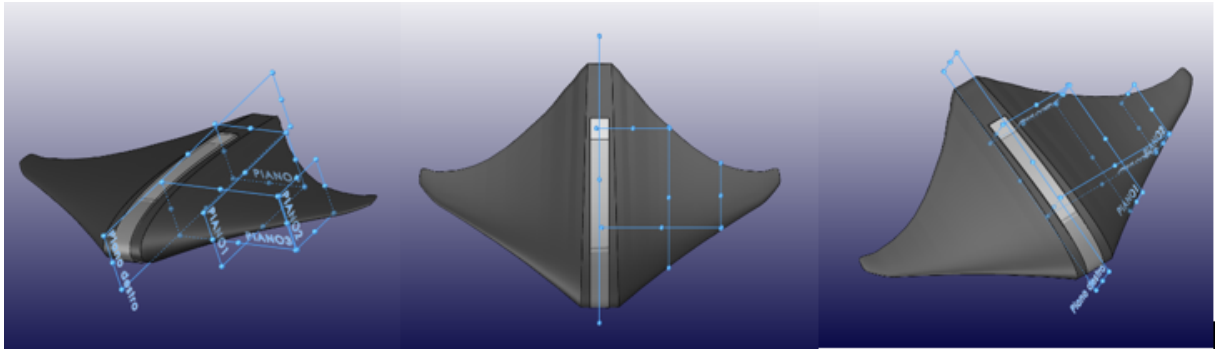


Figure 5.14: Division of six sections of the left fin of the Manta Robot. one for the back fin, two for the front fin and three for the central mechanism.

The subdivision adopted in figure 5.14 consists in replicating those surfaces in correspondence of the barycentre of all links of the robot in order to have a parallel environment in the motors domain. For each half six surfaces are taken into consideration:

- three for the central fin mechanism.
- two for the front fin mechanism.
- one for the back fin mechanism.

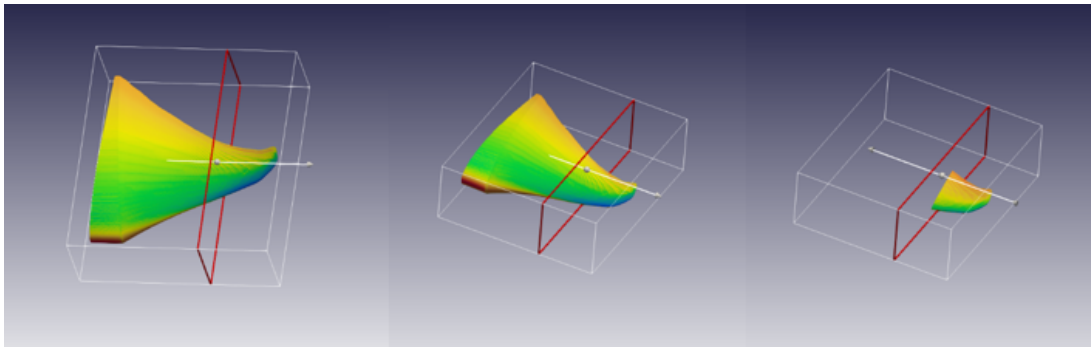


Figure 5.15: Slicing of the tip of the fin.

Lets focus on the surface represented in figure 5.15 in correspondence of the tip of the fin: From the software 'Para-View' all the forces, torque, velocity, pressure that are interacting within the fin are extracted. The simulation covers 1 period (1s) and results are provided every 0,01s.

The objective of this study is to extract forces and torque in active directions, to put them into a time vector and to simulate with simmechanics their contribution on motor's domain.

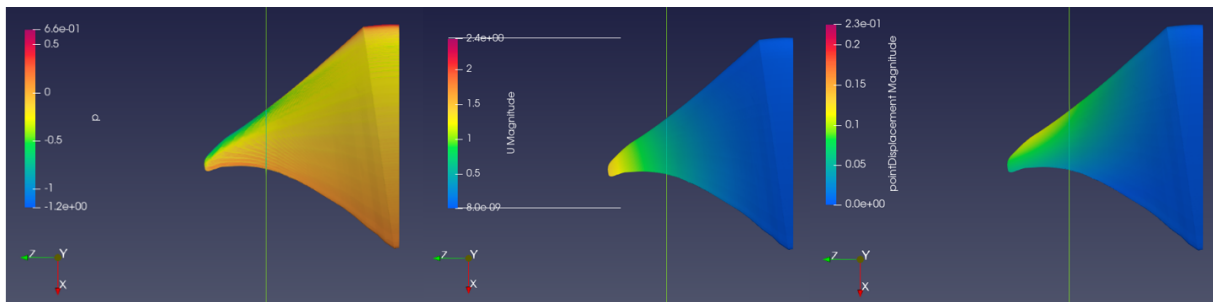


Figure 5.16: 3D visualization of pressure, velocity, displacement of the tip of the fin.

Analogously, for every other portion of the fin, a parallelism with motor's environment is set and all data regarding active directions in multibody environment are added in order to recreate the conditions that the robot will face during swimming.

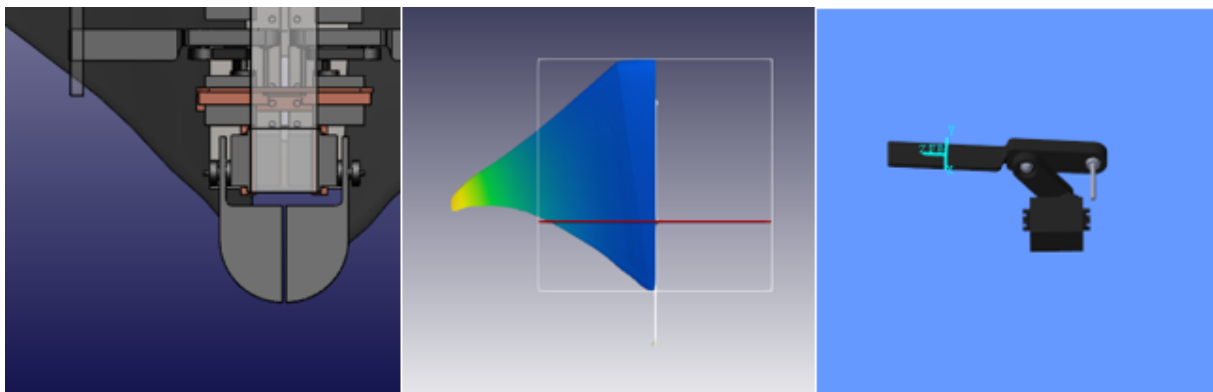


Figure 5.17: Example of back fin parallelism between CAD, CFD and Simulink

5.3 Results

From CFD analysis it was possible to extract some important information about fluid-robot interactions for sections selected in previous paragraph:

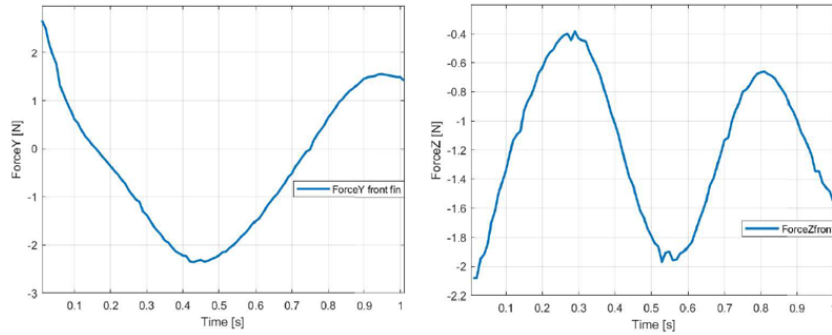


Figure 5.18: a) Force along Y front fin. b) Force along Z front fin.

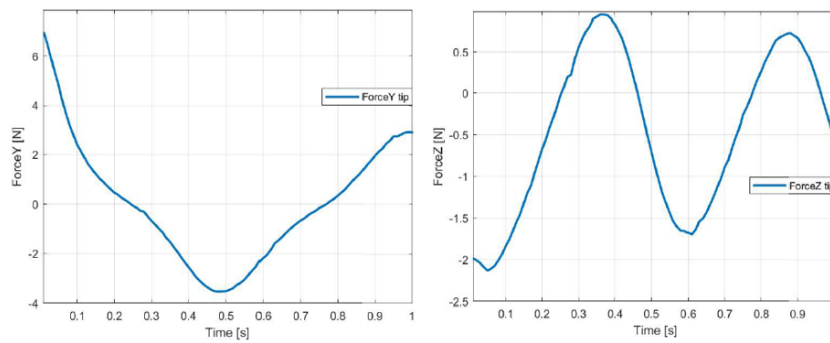


Figure 5.19: a) Force along Y central fin. b) Force along Z central fin.

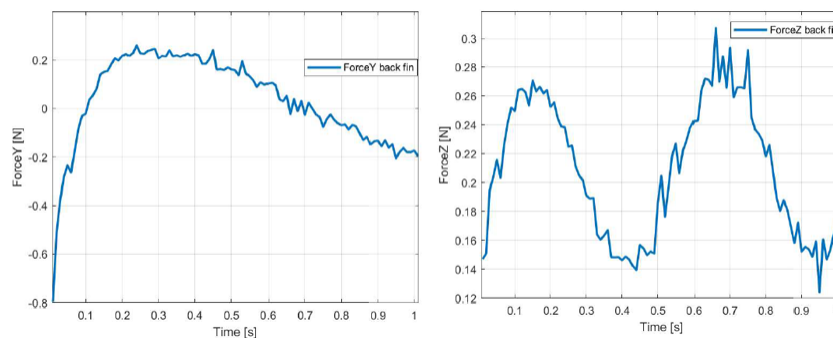


Figure 5.20: a) Force along Y back fin. b) Force along Z back fin.

In figures 5.18, 5.19, 5.20 forces along Y and Z axes are plotted in correspondence of the three principal mechanisms. As it can be clearly seen, the frequencies along Z are double compared to the others. This happens because the fin, starting from the zero position,

(fully extended fin) both when it reaches the maximum positive amplitude and when it reaches the maximum negative amplitude moves the fluid towards the central body of the robot. The fluid instead moves outward when the fin returns to zero position from both maximum amplitudes.

The most significant magnitudes are of the order of 6N so these values, quite contained, show that the biology of manta rays is very suitable in terms of force interaction so also in power consumption. It is also evident that in the rear of the robot fluid interaction is very low with respect to others and that the magnitude of the required torques along X and Z are at maximum of 0.3 N so its contribute is negligible with respect to the others. The graphs, which concern the rear fin, are characterized by disturbances, this is because in the prossimity of this fin and near the tail vortex shedding occurs as described in figure3.5. Lastly, the phase shift is quite evident between front and central mechanisms, this is due to the fact that the sinusoidal motion described above influences the time position of the peaks. This effect is evident also in back mechanism but, as said before, low magnitudes allows to consider it negligible.

Here on results of the matching between fluid-robot interaction and motors-robot interaction are shown. The extractions are in correspondence of the three motors in the right half of the manta when it moves with sinusoidal motion with a velocity of 1 m/s and a variable phase shift in time between the three mechanisms.

Below the analysis focuses on the different results obtained when the phase shift between fins varies. More in detail the result of four cases of study with different time lag, from 0 seconds to 0.2 seconds between fins and the relative power consumption are showed:

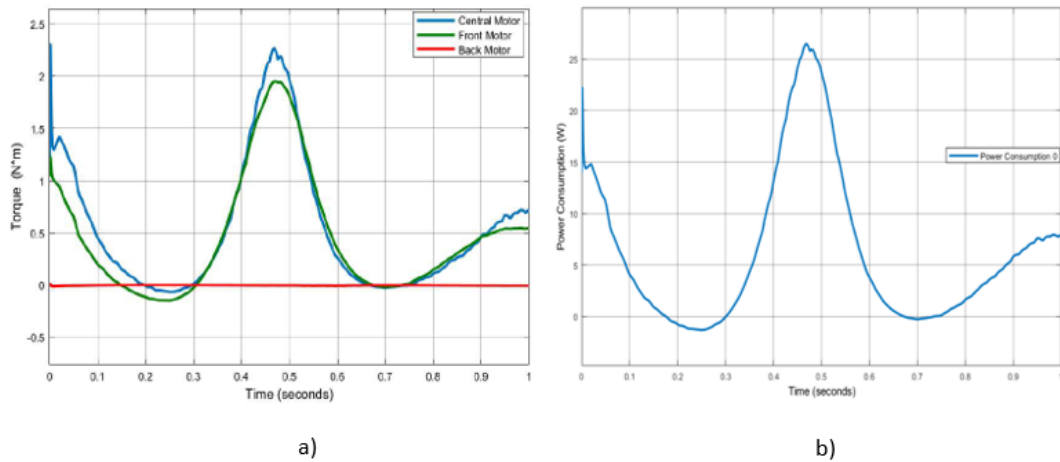


Figure 5.21: a) Torque of the three motors at 0s time lag. b) Power consumption of the system with 0 time lag.

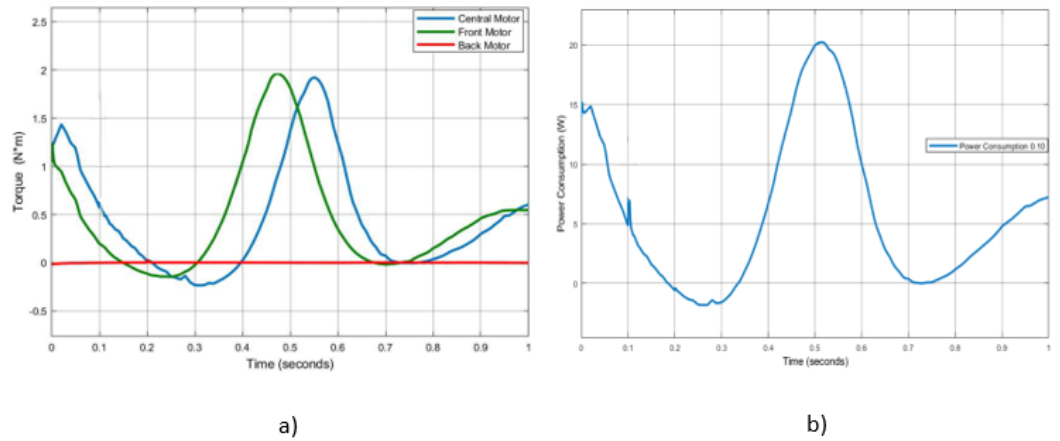


Figure 5.22: a) Torque of the three motors at 0.1s time lag. b) Power consumption of the system with 0.1 time lag.

The results in fig.5.21 fig. 5.22 fig. 5.23 and fig. 5.24 are quite evident: all the three motors have the same response shifted by the time lag that defines the sinusoidal movement. Magnitude progressively decreases from 1.9Nm of the front motor to the back one . Each of them justifies the choice of the motors for this application in the following chapter. Now the attention is moved on a fact that encourage this thesis work: the beneficial effects in terms of power and energy consumed that has the sinusoidal motion of the manta ray.

- with 0s time lag between fins, power consumption reach 25 W while the energy con-

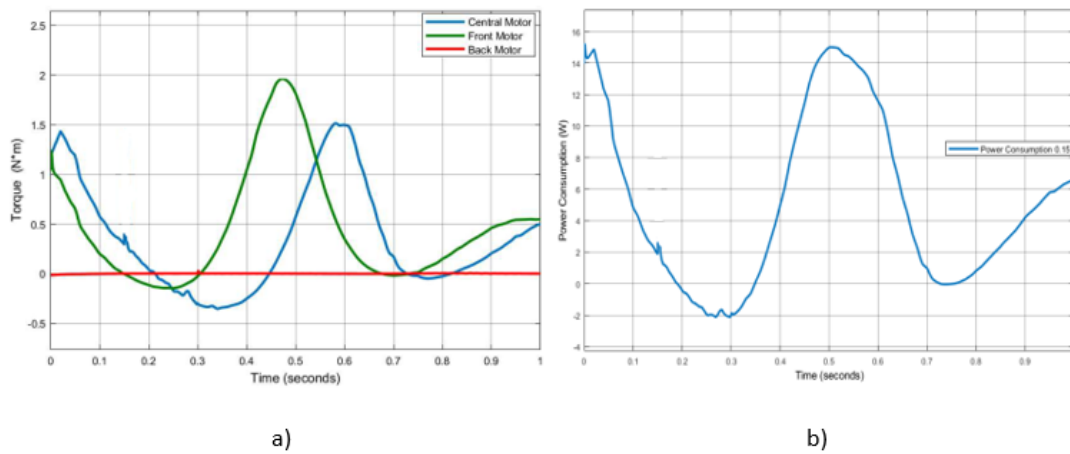


Figure 5.23: Torque of the three motors at 0.15s time lag. b) Power consumption of the system with 0.15 time lag.

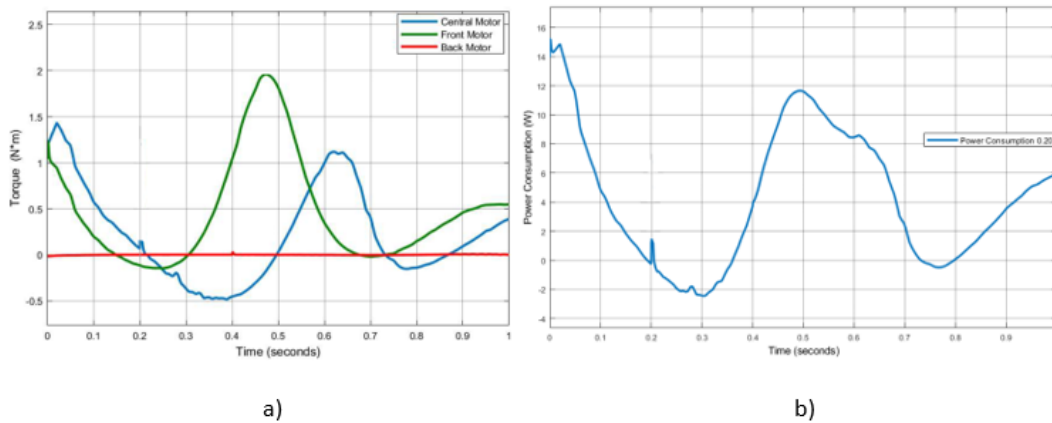


Figure 5.24: Torque of the three motors at 0.2s time lag. b) Power consumption of the system with 0.2 time lag.

suption reach 4.9 J

- with 0.1s time lag between fins, power consumption reach 20 W while the energy consumption reach 4.6 J
- with 0.15s time lag between fins, power consumption reach 15 W while the energy consumption reach 4.3 J
- with 0.2s time lag between fins, power consumption reach 11 W while the energy consumption reach 4.1 J

Chapter 6

Motors and Electrical Circuit

The figure 6.1 shows the electrical circuit for driving and controlling the motors. The circuit is composed of:

- 8 servo motors
- Arduino Mega 2560
- Breadboard
- DC power supply
- Joystick

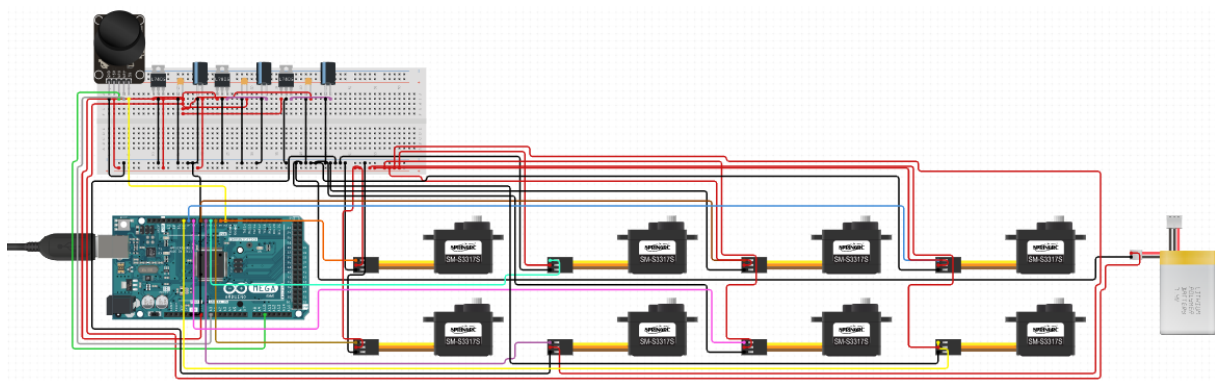


Figure 6.1: Electrical components

6.1 Servo Motors

The results obtained from 3D analysis, through the interaction between Simulink and Computational Fluid Dynamics, have allowed to obtain useful data for the choice of servomotors. Servo motors are specially designed motors to be used in control applications and robotics. They are used for precise position and speed control at high torques. It consists of a suitable motor, position sensor and a sophisticated controller(fig.6.2). Servo motors can be characterized according the motor controlled by servomechanism, thus major types of Servo motor may be - (i) DC Servo motor, (ii) AC Servo motor. Servo motors are used

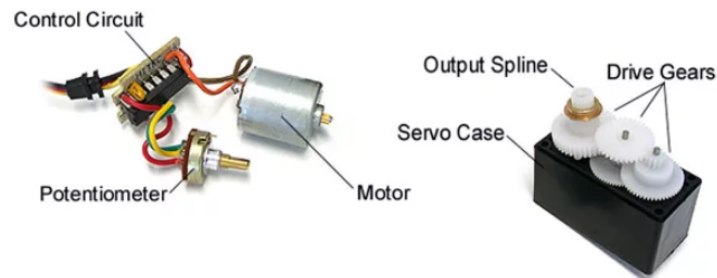


Figure 6.2: Servo motor components.

to control position and speed very precisely, but in a simple case, only position may be controlled. Mechanical position of the shaft can be sensed by using a potentiometer, which is coupled with the motor shaft through gears. The current position of the shaft is converted into electrical signal by the potentiometer, and the compared with the command input signal. In modern servo motors, electronic encoders or sensors are used to sense the position of the shaft.

From the analysis, the results show that the maximum torque required, by the front servo motor, for oscillatory swimming motion is 1.9 Nm, while the swimming speed of the manta chosen for the analysis is $1\frac{m}{s}$; on the basis of these data, the choice of the motor was a complex task, given the need for a servo motor with 360-degree rotation that at the same time provided a high torque and rotation speed, with feedback for the control system and with a small footprint and limited weight and cost. The servo motors used, supplied with all the required characteristics, are Feetech FR5311M-360FB Continuous Rotation motor. The most important features are:

- 12Bit Contactless Absolute Encoder AS5600 With 0-3v3 Analog Output

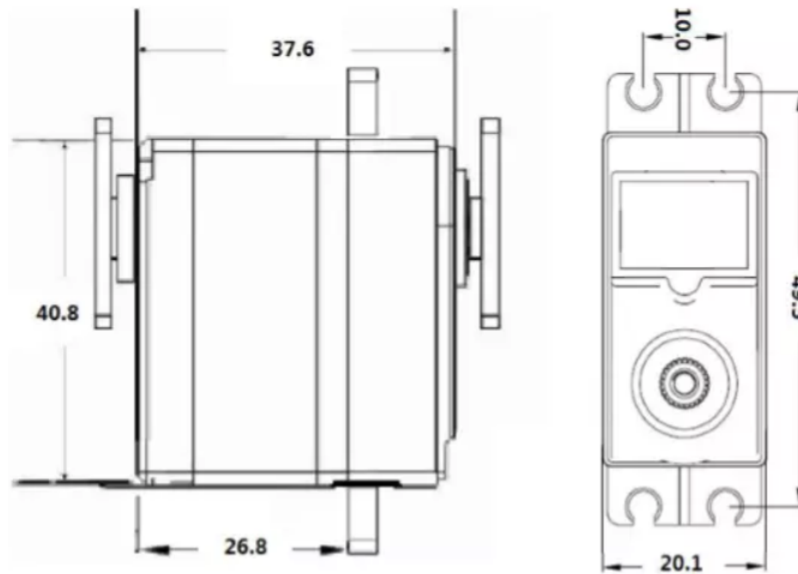


Figure 6.3: Feetech servo motor dimensions.

- Analog Feedback 360degree with 0-3.3V
- 360 Degree Continue Rotation To Be Control With RC PWM
- Standard Digital Programmable Metal Gears Servo,2BB
- High Quality Core Motor, No limits can 360 degree rotation
- Operating Voltage: 4.8V-8.4V
- Interface: (like JR)
- Size: 40.2*20.0*38.0mm
- Weight: 58g (2.05oz)
- Speed: 55RPM(4.8V) / 60RPM(6V)
- Torque: 10.1kg.cm(4.8V) 14.5kg.cm(6V) 20.0kg.cm(7.4V)

The servo motor is controlled through pulse width modulation. Rotational speed and direction are determined by the duration of a high pulse, in the $1000\mu s$ - $2000\mu s$ range. In order for smooth rotation, the servo needs a $20ms$ pause between pulses. As the length of the pulse decreases from $1500\mu s$, the servo will gradually rotate faster in the clockwise

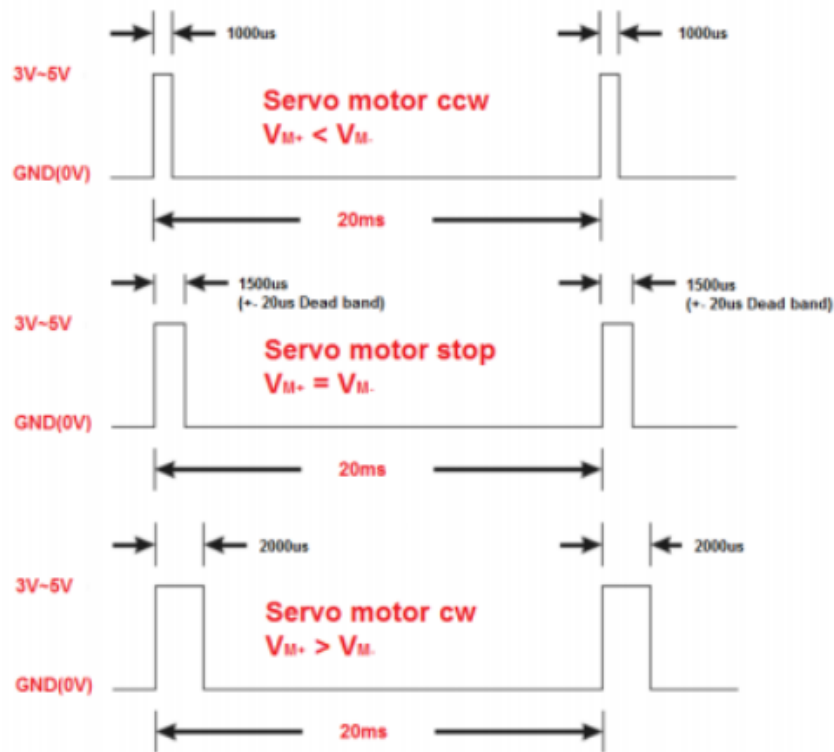


Figure 6.4: Pulse control mode.

direction, as can be seen in the figure 6.4. Therefore, summing up, the range from $1480\mu s$ to $1520\mu s$ stops the motor; the range from $1520\mu s$ to $2000\mu s$ allows to adjust the rotation speed clockwise while the range from $1480\mu s$ to $1000\mu s$ anti-clockwise (figure 6.5). The motor is equipped with 4 wires (fig 6.6); one for the ground, one for the voltage, one for the signal and one for the feedback. The position feedback is guaranteed by AS5600 absolute contactless encoder; it is a Hall-based rotary magnetic position sensor using planar sensors which converts the magnetic field component perpendicular to the surface of the chip into a voltage. The signals coming from the Hall sensors are first amplified and filtered before being converted by the analog-to-digital converter (ADC). The output of the ADC is processed by the hardwired CORDIC block (Coordinate Rotation Digital Computer) to compute the angle and magnitude of the magnetic field vector. The intensity of the magnetic field is used by the automatic gain control (AGC) to adjust the amplification level to compensate for temperature and magnetic field variations. The angle value provided by the CORDIC algorithm is used by the output stage. The user can choose between an analog output and a PWM-encoded digital output. The former provides an output voltage which represents the angle as a ratiometric linear absolute value. The latter provides

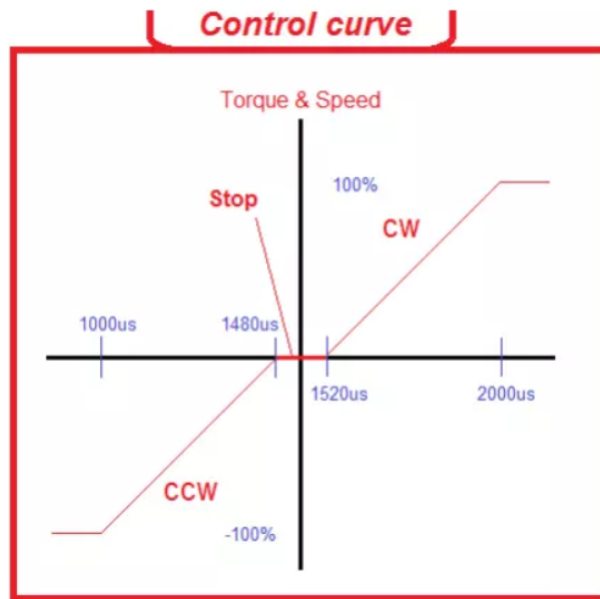


Figure 6.5: Control curve.



Figure 6.6: Feetech motor's wire.

a digital output which represents the angle as the pulse width. This contactless system measures the absolute angle of a diametric magnetized on-axis magnet. This AS5600 is designed for contactless potentiometer applications and its robust design eliminates the influence of any homogenous external stray magnetic fields. The encoder is also equipped with a smart low power mode feature to automatically reduce the power consumption. An input pin (DIR) selects the polarity of the output with regard to rotation direction. If DIR is connected to ground, the output value increases with clockwise rotation. If DIR is connected to VDD, the output value increases with counterclockwise rotation. For applications which do not use the full 0 to 360 degree angular range, the output resolution

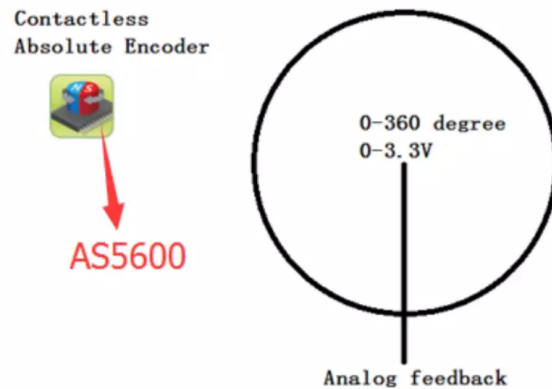


Figure 6.7: AS5600 absolute encoder.

can be enhanced by programming the range which is actually used. In this case, the full resolution of the output is automatically scaled to the programmed angular range. The angular range must be greater than 18 degrees. The range is specified by programming a start position (ZPOS) and either a stop position (MPOS) or the size of the angular range (MANG).

6.2 Arduino

Arduino is an open-source electronics platform based on easy-to-use hardware and software. It is possible to tell to the board what to do by sending a set of instructions to the microcontroller on the board. To do so it is possible to use the Arduino programming language (based on Wiring), and the Arduino Software (IDE), based on Processing. There are many other microcontrollers and microcontroller platforms available for physical computing: Parallax Basic Stamp, Netmedia's BX-24, Phidgets, MIT's Handyboard, and many others offer similar functionality. All of these tools take the messy details of microcontroller programming and wrap it up in an easy-to-use package. Arduino also simplifies the process of working with microcontrollers, but it offers some advantage over other systems:

- **Inexpensive:** Arduino boards are relatively inexpensive compared to other microcontroller platforms. The least expensive version of the Arduino module can be assembled by hand, and even the pre-assembled Arduino modules cost less than \$50.

- **Cross-platform:** The Arduino Software (IDE) runs on Windows, Macintosh OSX, and Linux operating systems. Most microcontroller systems are limited to Windows.
- **Simple, clear programming environment :** The Arduino Software (IDE) is easy-to-use for beginners, yet flexible enough for advanced users to take advantage of as well. For teachers, it's conveniently based on the Processing programming environment, so students learning to program in that environment will be familiar with how the Arduino IDE works.
- **Open source and extensible software:** The Arduino software is published as open source tools, available for extension by experienced programmers. The language can be expanded through C++ libraries, and people wanting to understand the technical details can make the leap from Arduino to the AVR C programming language on which it's based.

This project is based on the use of Arduino Mega 2560. It is a microcontroller board



Figure 6.8: Arduino Mega 2560.

based on the ATmega2560. It has 54 digital input/output pins (of which 15 can be used as PWM outputs), 16 analog inputs, 4 UARTs (hardware serial ports), a 16 MHz crystal oscillator, a USB connection, a power jack, an ICSP header, and a reset button. It contains everything needed to support the microcontroller; simply connect it to a computer with a USB cable or power it with a AC-to-DC adapter or battery to get started. The most important characteristics are summarized below:

- **Microcontroller:** ATmega1280
- **Operating Voltage:** 5V
- **Input Voltage (Recommended):** 7-12V
- **Input Voltage (limits):** 6-20V
- **Digital I/O Pins:** 54(of which 15 provide PWM output)
- **Analog Input Pins:** 16
- **DC Current per I/O Pin:** 40 *mA*
- **DC Current for 3.3V Pin:** 50 *mA*
- **Flash Memory:** 128KB of which 4KB used by bootloader
- **Clock Speed:** 16MHz

The Arduino Mega can be powered via the USB connection or with an external power supply. The power source is selected automatically. External (non-USB) power can come either from an AC-to-DC adapter (wall-wart) or battery. The adapter can be connected by plugging a 2.1mm center-pos plug into the board's power jack. Leads from a battery can be inserted in the Gnd and Vin pin headers of the POWER connector.

The board can operate on an external supply of 6 to 20 volts. If supplied with less than 7V, however, the 5V pin may supply less than five volts and the board be unstable. If using more than 12V, the voltage regulator may overheat and damage the board. The recommended range is 7 to 12 volts.

Each of the 54 digital pins on the Mega can be used as an input or output, using `pinMode()`, `digitalWrite()`, and `digitalRead()` functions. They operate at 5 volt pin can provide or receive a maximum of 40 mA and has an internal pull-up resistor (disconnected by default) of 20-50 kOhms.

6.3 Power Supply and Breadboard

To take full advantage of the properties of the servo-motors, the 5V supplied by Arduino Mega is not sufficient. For this reason, an external power supply is used to reach the

torque and speed values necessary for the project. The battery used is the Full Power Lipo 2S 5200 mAh 50C Gold V2, shown in figure 6.9, capable of delivering 7.4V and way more than 2A. The table 6.1 lists all the useful information.



Figure 6.9: External power supply.

Table 6.1: Power supply features

Cell type	LiPo
Dimensions	50x163x30 mm
N. of cells	2S
Voltage	7.4V
Capacity	5200 mAh
Weight	265g
Balancer connector type	JST-XH
Plug type	DEANS
Discharge Rate	50C
Max Burst discharge Rate	80C(416 Ampere)
Charge Rate	1-5C

As previously mentioned Arduino Mega only delivers 5V and in addition it has a limited number of V_{out} pins that do not allow to connect all the motors. It is therefore necessary to use a breadboard to connect the external battery to the 8 servo motors and to arduino in order to power and control the system.

Simplicity, speed of use and good reliability make it an indispensable instrument when developing and studying a project in order to test the correct functioning of a circuits. A breadboard (fig.6.10a) is a tool used to create prototypes of electric circuit. Unlike other

similar devices, on which the components and connections that make up the prototype are welded, the breadboard does not require welding and is completely reusable. It consists of a base provided with one median groove and a series of holes arranged in rows and columns. The upper and lower holes are electrically connected horizontally and are normally used for the power supply. The central holes are electrically connected vertically as is shown in figure 6.10b. The dimensions of the holes are suitable for inserting the leads (terminals) of the most common components.

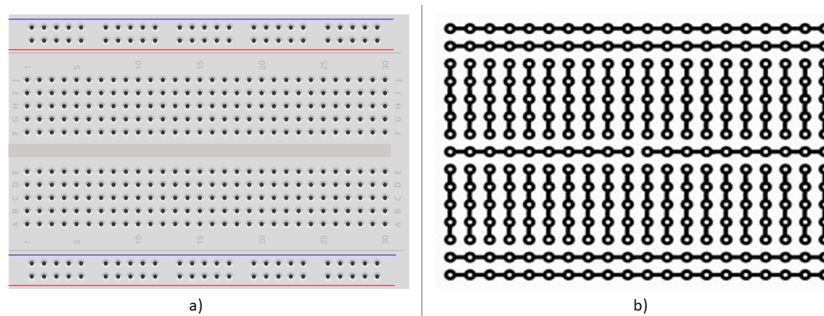


Figure 6.10: a) Breadboard used in this project b) Electrical connection lines in the breadboard.

6.4 Joystick

Finally the last component used is the joystick (figure 6.11). The joystick is similar to two

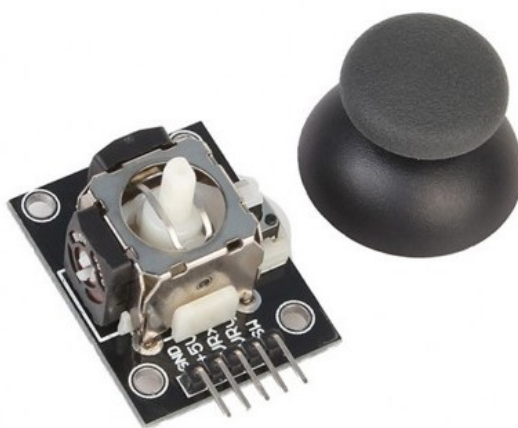


Figure 6.11: Joystick.

potentiometers connected together, one for the vertical movement (Y-axis) and another for the horizontal movement (X-axis). The potentiometers are variable resistances and,

in a way, they act as sensors that provide the with varying voltage depending on their rotation. The basic idea of a joystick is to translate the stick's position on two axes — the X-axis (left to right) and the Y-axis (up and down) into a signal an Arduino can process. This can be little tricky, but thanks to the design of the joystick consisting of two potentiometers and a Gimbal Mechanism. In order to read the joystick's physical position, we need to measure the change in resistance of a potentiometer. This change can be read by an Arduino analog pin using ADC. As the Arduino board has an ADC resolution of 10 bits, the values on each analog channel (axis) can vary from 0 to 1023. So, if the stick is moved on X axis from one end to the other, the X values will change from 0 to 1023 and similar thing happens when moved along the Y axis. When the joystick stays in its center position the value is around 512. The graphic below (figure 6.12) shows the X and Y directions and also gives an indication of how the outputs will respond when the joystick is pushed in various directions. The use of the joystick therefore made possible

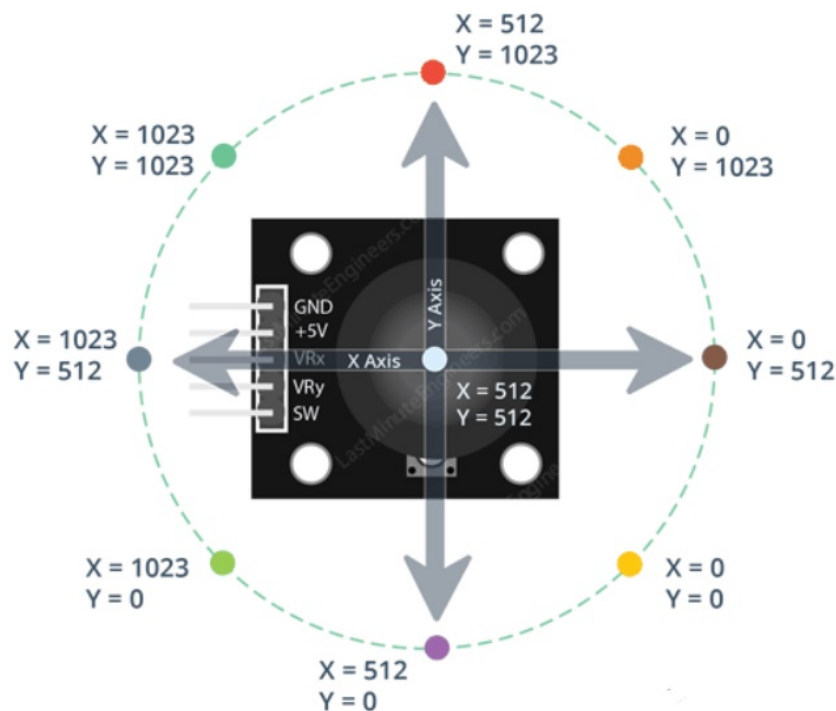


Figure 6.12: Joystick.

to coordinate various types of control systems analyzed in the next chapter.

Chapter 7

Motion Control

7.1 Introduction

Motion control is a widely used practice in the engineering field because it allows to make changes to a system in order to benefit from a desired condition. In the case study, obtaining the desired motion is of fundamental importance in order to replicate fin conditions of the manta ray. What happens inside motors in continuous motion presented in previous chapter is what determines the progression of six mechanisms and is therefore subject to control action. Therefore it is necessary to understand how to extract information about instantaneous positions held by electric motors, check their progress and establish which is the desired target for each of them. Once the feedback from 360 degrees motor's encoder is obtained, it can be used to change input conditions on the robot and thus to maintain the desired motion.

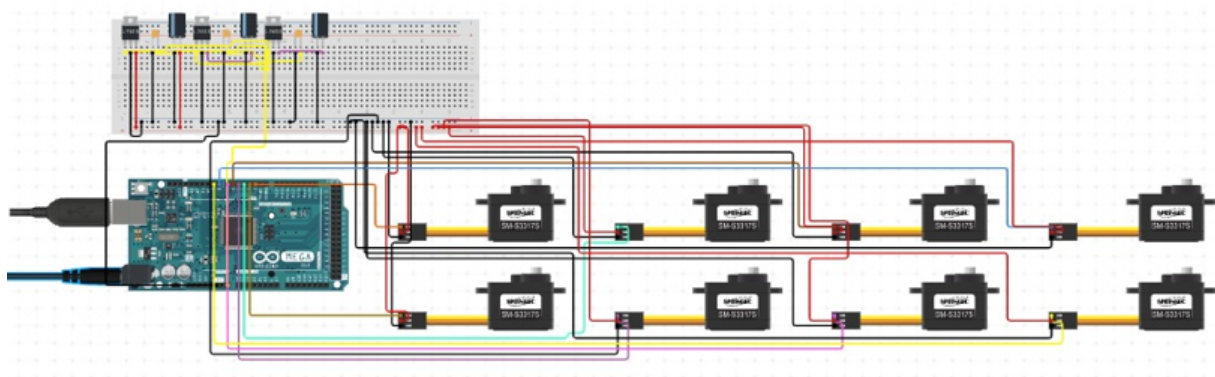


Figure 7.1: main motor's connections with Arduino mega board and breadboard

A further task is to exploit the high maneuverability of the robot to make turns with the minimum radius of curvature. Then the robot can turn right or left as well as move forward, maintaining the oscillatory motion that characterizes it, using high efficiencies and performance values of bio inspired robotics. In fig. 7.1 it is shown the circuit of the system in order to give an immediate perspective on the problem and to help understand the large amount of information that simultaneously is processed by the robot controller. All this information is fundamental in motion reconstruction process and in balancing the torque to be supplied to motors during operations.

7.2 Filtering

Before analyzing the lag between the fins and the motions reproduced, it is important to study the connection and interface between the motors and Arduino; in fact in order to set parameters for the control logic, it is useful to understand what happens inside motors, in particular is useful to find which type of input can be controlled and which output can be extracted from motors. Classical control logics were implemented and the first choice is based on the state target: the choice could be either the position or the velocity of the rotor of electric motors. Starting in a control means being capable of manipulate a feedback signal that refers to a state. In doing such it is useful the magnetic encoder that is inside motors. The encoder signal is a PWM signal (Pulse Width Modulation) that consist in an on/off quadratic wave. Plotting it is possible to recognize an upper part (3.3V) and a lower part (0V). The duration of either on or off mode represents the angular position of the rotor. If the motor is kept at constant velocity the duration of the on 'time' continuously increases till a value of 1024, then it will restart from 0.

Red feedback cable passes the PWM signal to the microcontroller of Arduino Mega board, the same happens for all the other motors. PWM signals are recognized by the clock that runs at a frequency of 16MHz. Mathematical equivalence between PWM and position angle allows the processor to understand the position of the encoder. The feedback signal contains very high disturbances and it must be filtered to evaluate the actual velocity of the shaft. The encoder essentially acts as a quantizer of the position

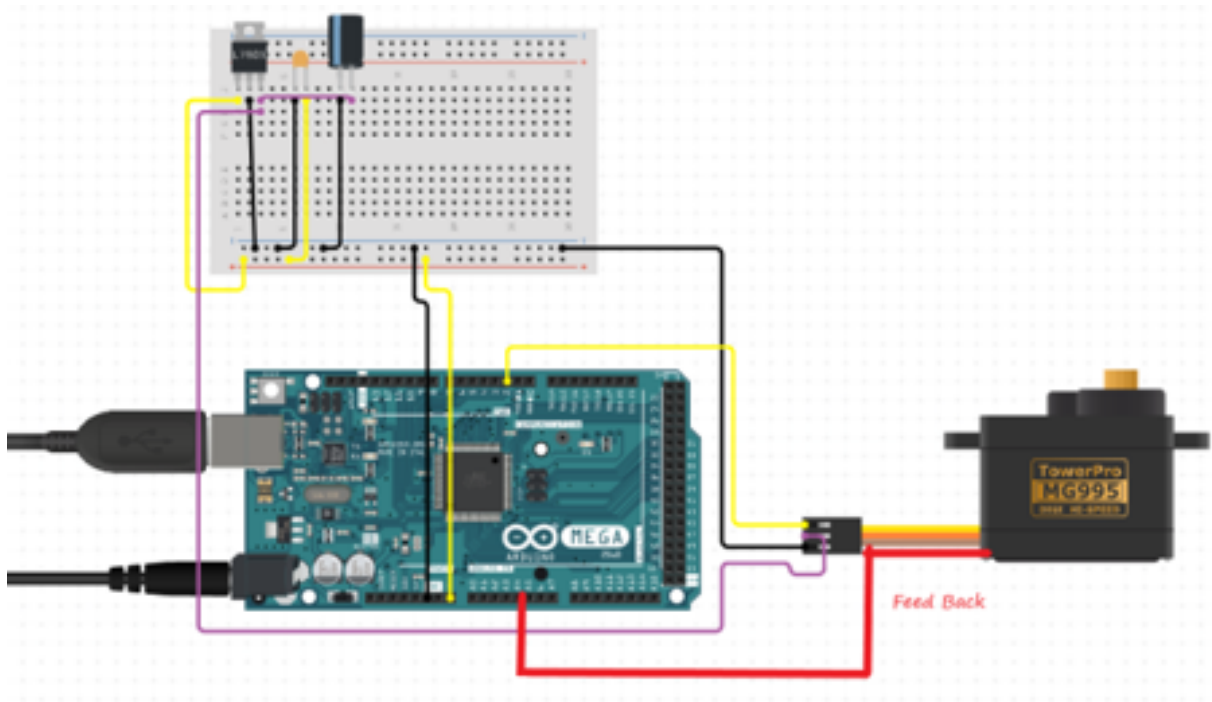


Figure 7.2: Feedback signal circuit representation of a single motor

signal. The resolution depends on the number of bits N .

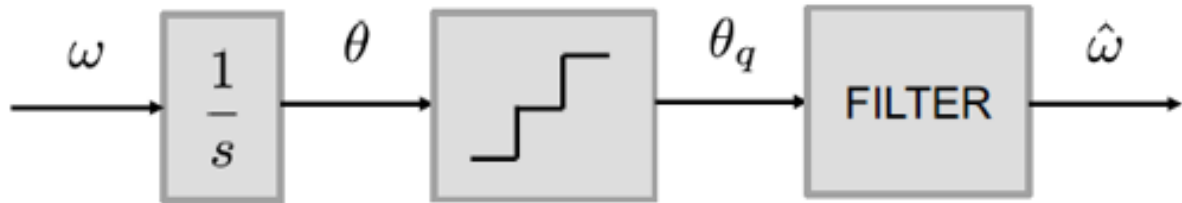


Figure 7.3: Block diagram of encoder's signal.

A straightforward solution for the estimation of the shaft velocity would be to compute the difference of the current and the previous position every discrete time step, i.e:

$$\hat{\omega}(k) = \frac{\theta_e - \theta_e(k-1)}{t(k) - t(k-1)} = \frac{\theta_e(k) - \theta_e(k-1)}{T_s} \quad (7.1)$$

The previous method relies on measuring the angular displacement within a fixed time interval. Another possibility is to measure the time needed to traverse a fixed angular

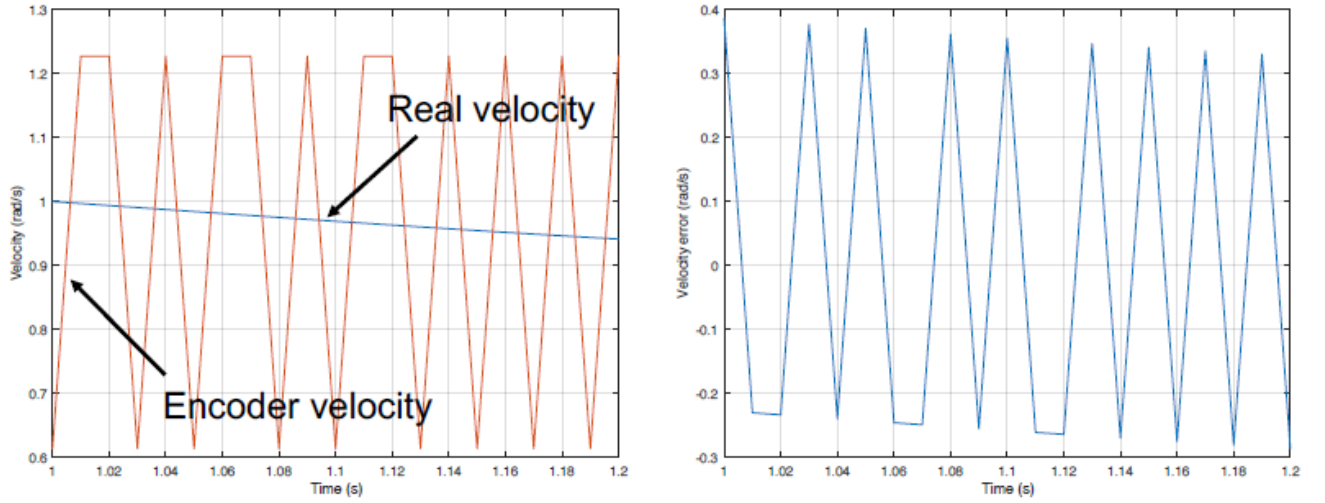


Figure 7.4: Encoder filtering process.

displacement, for example the resolution of the encoder, i.e:

$$\hat{\omega}(k) = \frac{\Delta\theta}{t(k) - t^{pre}} = \frac{2\pi/2^N}{t(k) - t^{pre}} \quad (7.2)$$

There are conditions, especially at low velocities, in which the second method is better than the first. Anyhow, the estimated velocity needs some filtering. The idea is to focus only on time instants when the encoder updates its output, as in other time instants the signal does not contain relevant information. In order to reconstruct the velocity signal, one can try to fit the measurements points with a polynomial curve. Depending on the degree D of the polynomial there are two possibilities:

- $D < M - 1$: approximation problem
- $D = M - 1$: interpolation problem

Approximation ($D < M - 1$) : determine the best fitting polynomial. As in general it does not exist a polynomial curve of degree D that passes exactly through M points, therefore it is necessary to minimise the approximation error. The polynomial can be

written as follows:

$$\hat{\theta}(t) = k_D t^D + k_{D-1} t^{D-1} + \dots + k_1 t + k_0 = [t^D \quad t^{D-1} \quad \dots \quad t \quad 1] \begin{bmatrix} k_D \\ k_{D-1} \\ \vdots \\ k_1 \\ k_0 \end{bmatrix} = t^T k \quad (7.3)$$

Interpolation ($D = M - 1$): in general the polynomial of order D passing through M-1 is unique and it can be determined requiring:

$$\forall i = 1, \dots, M : \|\theta_e(t_i) - \mathbf{t}(t_i)^T \mathbf{k}\|^2 = 0 \quad (7.4)$$

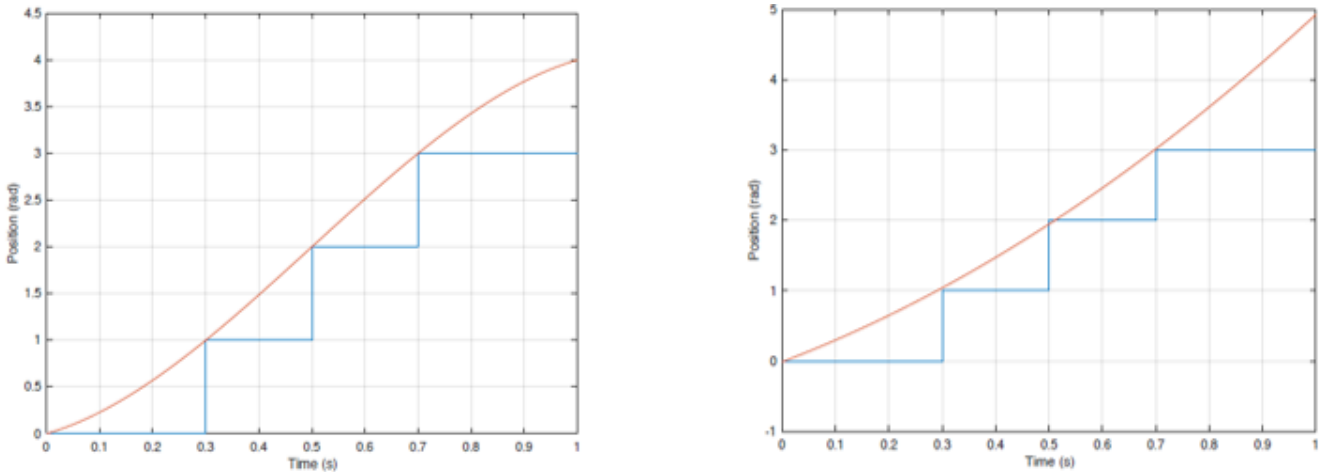


Figure 7.5: Polynomial curve vs approximation curve

Finally, one can compute the velocity by differentiating the interpolating/approximating polynomial with respect to time and evaluate it corresponding to the last time instant to obtain the most updated estimate of the shaft velocity.

The fact that signal varies in time requests a faster computation so a Moving Average filter is implemented. Moving average is a technique used in lot of applications and it consists of a windows made of a set of data, that moves in time; the number N of data collected in this window define dimensions of this window.

Motors selected responded very well to this kind of filter because of the large amount of

data that Arduino board is capable of managing. The chosen, number of sample points in each moving window along the signal is 40, this means that the first 40 data are averaged and then the first number is canceled by the next one, and so on during all operations. Here on it is shown the result of a moving average done while shaft of the motor is rotating.

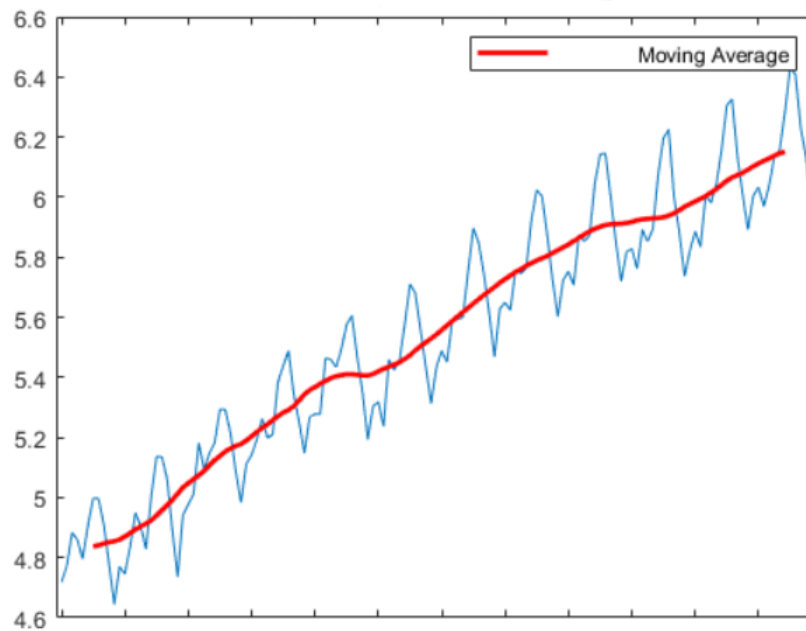


Figure 7.6: Moving average filtering on data from the encoder with N equal to 40.

7.3 Sinusoidal wave and Calibration

After filtering the feedback signal of the motors it is possible to implement various control systems useful for the purpose of this project. However, these control logics are influenced by the calibration of the motors, i.e. the position that the motors recognize as 'zero position'. Therefore the first step is to establish a control logic capable of recognize the initial position in the right way. It will be of fundamental importance to keep control on this value because it would be the reference of each motion control. The zero position is, in fact, the first position that the motors must take before they can start any other function in order to start rotating at the same time and in the right direction. The "zero position" or "zero configuration" is different for each individual motor and is influenced by the rotation angle that each servo must respect in order to guarantee the sinusoidal

profile.

In fact another fundamental characteristic that influences all the movements, which will be described later, is the sine wave shape described by the pectoral fin. In order to replicate the correct wavenumber of the chordwise kinematic wave, which distinguishes the oscillatory motion, a phase shift between the three fins is introduced. Focusing the attention on the servos' rotor at the starting of the motion, front motor, central motor and back motor must have a specific position that must be kept at the beginning of every cycle.

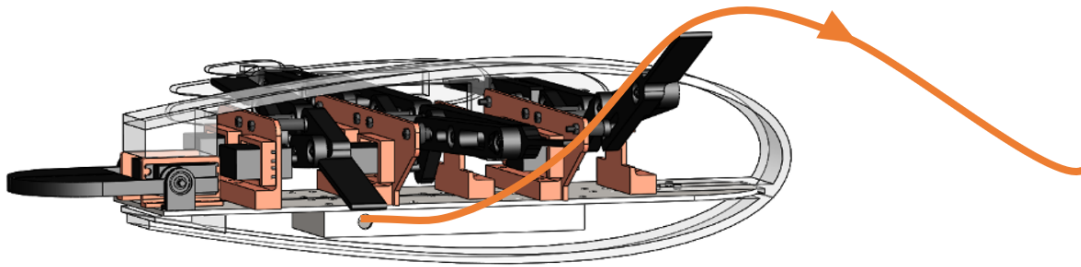


Figure 7.7: Sinusoid of the fins during forward motion

As can be seen in figure 7.7 the six motor have an angle lag of between 20 degrees to 40 degrees in order to replicate the sinusoidal wave. Furthermore, as already mentioned above and as can be seen in the figure, the three fins recreate the sinusoidal discipline with a wavenumber equal to 0.4 which distinguishes the oscillatory swimming motion from the undulatory one. Once the "zero configuration" and the phase shift between the fins are fixed, the control system for each swimming motion is implemented and analyzed in detail. In the following paragraphs three type of movement are described:

- the straight water motion;
- the right turn;
- the left turn;

7.4 Type of motion

Each of the motions is obtained by the continuous rotation of the 8 motors and in order to identify each type of motion it is possible to look at forces and how they propagate. To obtain the advancement of the robot it is necessary to generate a wave propagation from the head to the tail as can be seen in figure 7.8 in which

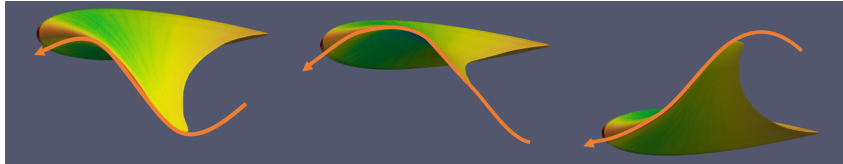


Figure 7.8: Wave propagation during forward motion

the orange line represents the motion of the robot, while the propulsion force takes shape in the opposite direction. To obtain this type of wave propagation it is necessary that the two sides of the robot rotate in the opposite direction, for example, the left column is rotating clockwise while the right column is rotating counter clockwise as shown in figure7.9

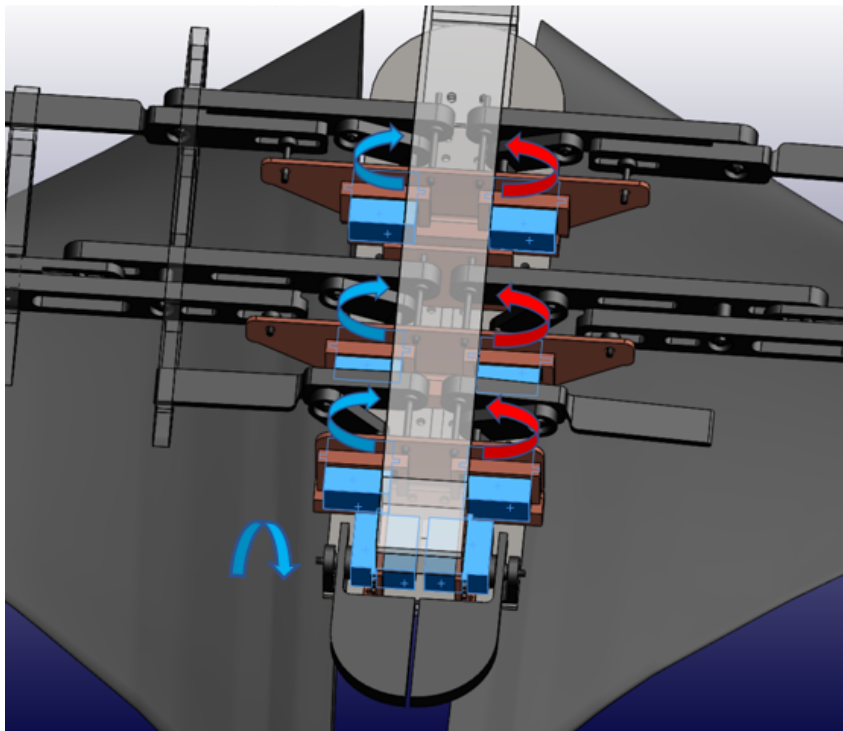


Figure 7.9: Motors torque during forward motion

Playing with the direction of propagation of the wave it is possible to obtain a high robot

maneuverability. In fact the direction of propulsion could be opposite for the two halves of the robot, so the left part could proceed front side while the right half could go backward. In the figure below there are shown the forward and backward wave propagations that are considered for the control logic.

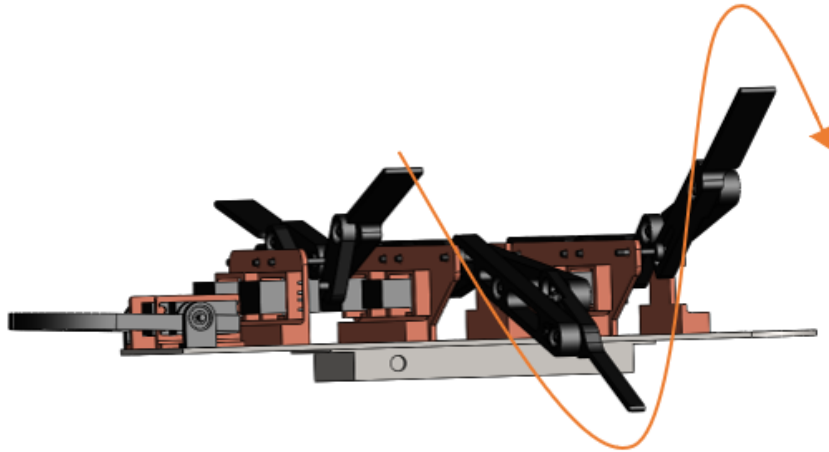


Figure 7.10: Sinusoid of the fins during forward motion

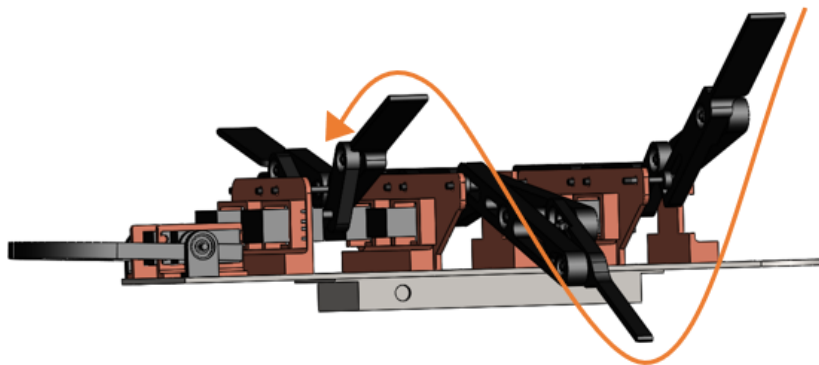


Figure 7.11: Sinusoid of the fins during backward motion

By splitting the Robot in two parts it is possible to proceed forward in a half and backward in the other half, in this way is created an opposite direction of the propulsion thrust force and so the robot will curve about its principal axis allowing the robot to make a

turn to the left or to the right with a minimum radius of curvature. It is important to notice that the backward direction of the propulsion force is caused by a sinusoidal motion that starts from the front fin and propagates till the back one. Vice versa the forward direction of the thrust force is caused by a sinusoidal motion that starts from the rear and propagates till the front. In practice, the decision of the mechanism that starts the sinusoid and let this sinusoid arrive to the opposite position defines the motion.



Figure 7.12: example of left and right rotation obtaine by split directions of motion in the two half

For what concern the tail, attention is focused on its movement. What characterises the tail is a continuous motion that makes at most 45 degrees in a direction and then another 45 degrees in the opposite direction. The frequency of the tail's movement must be the same as the six mechanism in order to recreate a continuous wave in the robot. During the straight movement of the manta the tail oscillates continuously between the two extreme positions while when the manta turns to the right or left the tail acts as a rudder. In fact during the left turn the left tail reaches the maximum negative position (the the servo motor reaches -45 degrees) and the right side reaches the maximum positive position; while during the right turn the opposite happens. It is also known that the tail put in the first one configuration make the robot go down deep while the second configuration made the robot lift

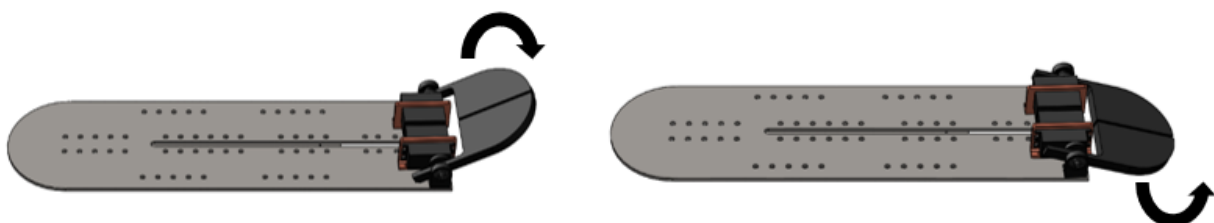


Figure 7.13: Tail movement during swimming to be implemented in control logic

7.5 Control Logic

Thanks to filtering process, it is possible to extract data from the servo's feedback useful for the development of some control logics. The control logics designed in this project concern: the zero position, the phase shift between the motors and the speed of the motors themselves. The basic idea is to choose a header that drives all the others servos. After extracting data relating to the position of the 'header' it is possible to use it for the calculation of the error on the position that 'slaves' have. Arduino code solves a system of extractions at each motor, compares them and establishes appropriate inputs to be given to slaves, so that all keep the required state target. The control logic on the zero position is important as it is the starting point for all developed motions. The figure7.14 provides a representative image of the control scheme seen from a 3D representation to the Solid

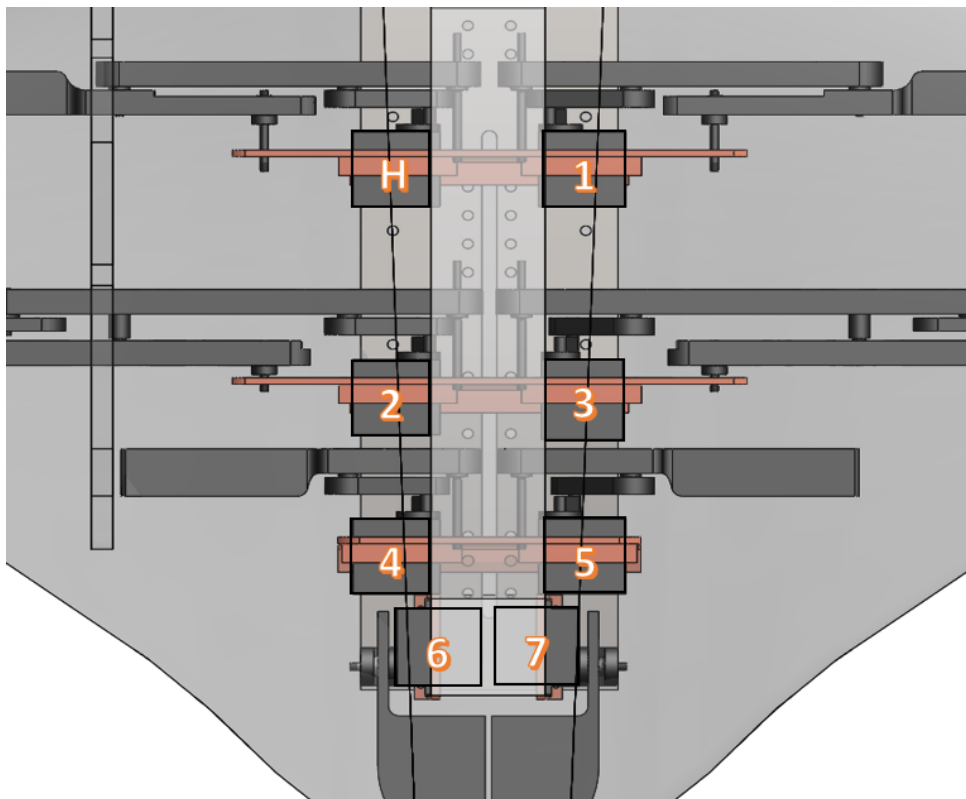


Figure 7.14: Schematic of the motor's layout, in which H is the 'header' and all others are slaves.

Works software in order to better understand the basic idea on which all the control logic systems are based. The zero position is influenced by a difference in degrees that the

eccentric of each motor must have to guarantee the phase shift. Here is a list of the main phase shifts adopted as a first attempt, later the parametric code capable of managing this phase shift based on variable parameters will be implemented. Considering in de-

Table 7.1: Zero configuration values.

Servo	Starting position	Rotation
Header	0	60 rpm CCW
1 st slave	0	60 rpm CW
2 nd slave	-20	60 rpm CCW
3 rd slave	20	60 rpm CW
4 th slave	-40	60 rpm CCW
5 th slave	40	60 rpm CW
6 th slave	0	Alternate
7 th slave	0	Alternate

tail the first 6 servos (headers and the 5 slaves), it was implemented a code in Arduino language capable of simultaneously interpreting six feedbacks and making changes in the input so that motors can reach the positions in figure7.15. This configuration is the so

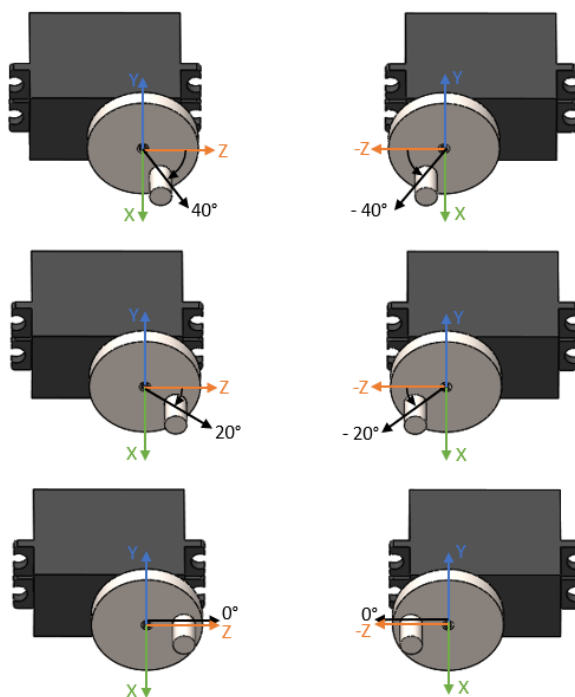


Figure 7.15: Design parameters for starting position of motors H to 5.

called 'zero configuration'. The zero configuration must be reachable at any time of the program, when something is not working the reset brings all the motors to 'zero configuration'. At this point, the first tests on the motors are observed by rotating them with a

constant pwm input to see how they react to the application of six inputs simultaneously and whether the current and voltage necessary to make them move has been calculated properly. Once this has been verified, it is noted that a control action is necessary as inputs given by the microprocessor are affected by error, moreover not all electric motors respond in the same way. Here the 'header' plays a fundamental role, as it becomes the reference to all the other engines and the difference with the header position defines the error.

As regards the control logic of the straight motion, from the zero configuration the servos start to move towards a continuous rotary motion at 60 rpm according to the directions indicated in table 7.1, i.e. the right branch will rotate counterclockwise while the left branch clockwise and at any instant of time, in parallel with the control system on the phase shift, also the speed one acts. In fact control action was made by steps, starting from the proportional branch and then adding the integrative branch and the derivative branch in order to obtain a PID useful to reach the state target on the position and nullify the error in the velocity.

The same criterion was used also to control turns and for this purpose the joystick will allow to choose which part of the code you want to access: forward, backward or turns as can be seen in figure7.16 so it is possible to indicate the type of motion you want to keep.

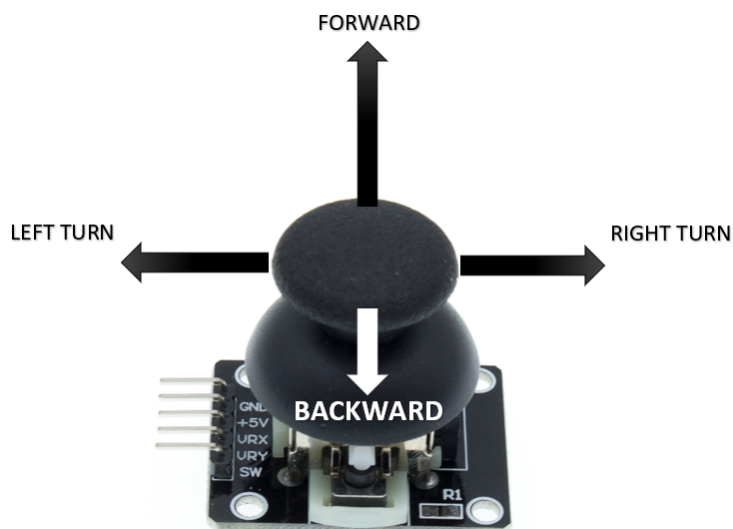


Figure 7.16: Joystick functionality.

Below are the tables of starting configurations during backward motion and during turns following the reference systems of figure.

Table 7.2: Starting condition during backward motion.

Servo	Starting position[deg]	Rotation
Header	-40	60 rpm CCW
1 st slave	40	60 rpm CW
2 nd slave	-20	60 rpm CCW
3 rd slave	20	60 rpm CW
4 th slave	0	60 rpm CCW
5 th slave	0	60 rpm CW

Table 7.3: ‘Zero configuration’ to be maintained during turn left.

Servo	Starting position[deg]	Rotation
Header	-40	60 rpm CCW
1 st slave	0	60 rpm CW
2 nd slave	-20	60 rpm CCW
3 rd slave	20	60 rpm CW
4 th slave	0	60 rpm CCW
5 th slave	40	60 rpm CW

Table 7.4: ‘Zero configuration’ to be maintained during turn right.

Servo	Starting position[deg]	Rotation
Header	-40	60 rpm CCW
1 st slave	0	60 rpm CW
2 nd slave	-20	60 rpm CCW
3 rd slave	20	60 rpm CW
4 th slave	0	60 rpm CCW
5 th slave	40	60 rpm CW

Below the block diagrams at the base of all the control logics developed (figure 7.17) for the movement of the robot are showed in order to explain and better understand the principle of operation conceived. Going into the detail of the controller, the figure 7.18 shows how a PID works for each servo motor.

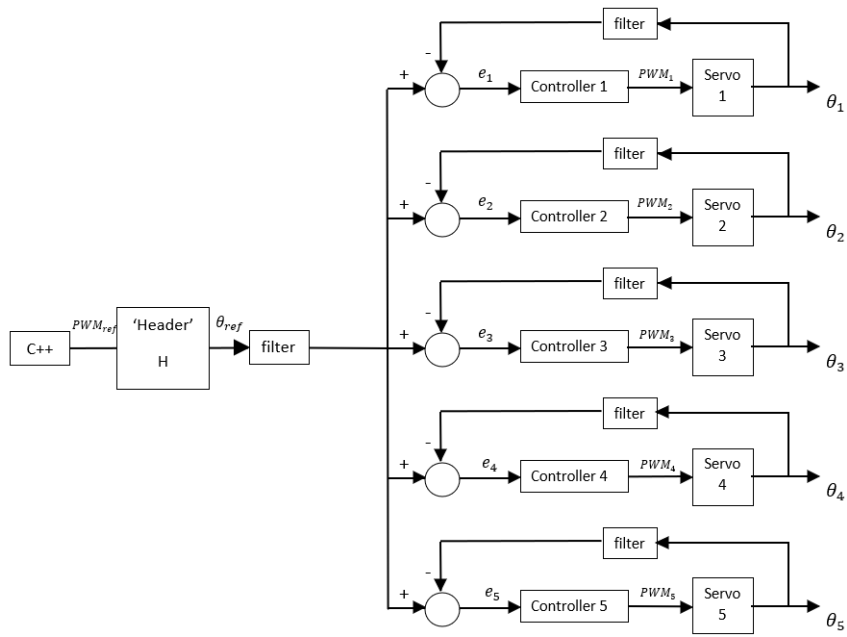


Figure 7.17: Block diagram of the control system.

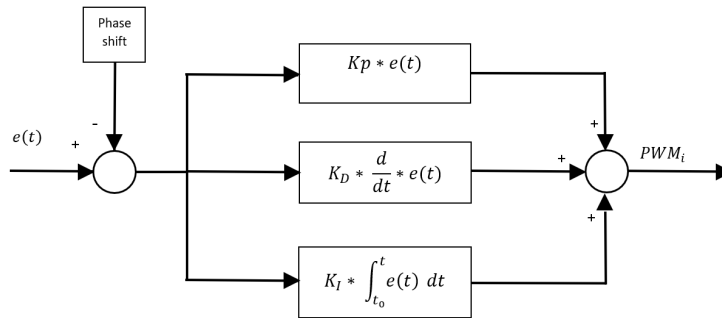


Figure 7.18: PID control system.

The gain values (K_p , K_d , K_I) were obtained through various experimental tests, and having the servo a different response to the speed variations, a greater weight was given to K_d .

Finally, the tail's code was implemented in order to take advantage of the benefits it brings. In fact, tail is fundamental in tacking and lift. Here too, the data filtering techniques are the same as described above. Tail's codes follow the "Header and Slaves" logic. Motors positioned as in the figure are respectively positioned at 0 and 180 degrees and must perform 45 degrees in one direction and 45 degrees in the other, rotating clockwise and counterclockwise respectively. During forward and backward motion the tail is used exclusively to gain or lose altitude. During turns, the movement is split by lowering only one half of the tail and thus facilitating the turn itself. Configuration of motors in the

rear of the robot is shown below, also this movement is managed externally by the use of the joystick. In this case the engine number 6 becomes the header and the engine number 7 becomes the slave. Also for the tail, the simpler control can be easily analyzed by the

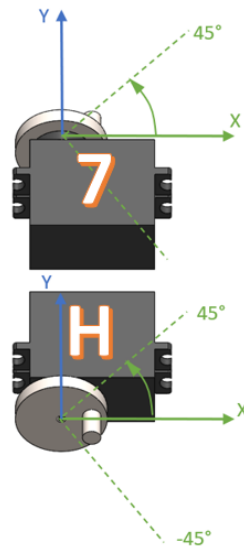


Figure 7.19: Tail control logic.

block diagram in the figure 7.20.

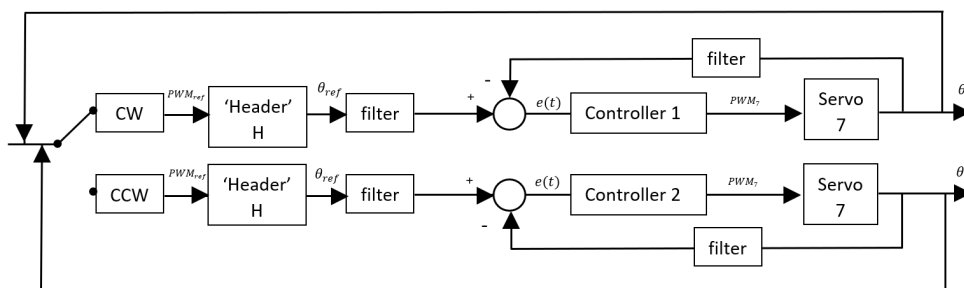


Figure 7.20: Tail block diagram.

Table 7.5: 'Tail zero configurations.

Servo	Starting position	Rotation	Type of motion
H	0	alternate	FW/BW
7	0	alternate	FW/BW
H	45	none	turn left
7	45	none	turn right

7.6 Testing

In this paragraph tests of control action are presented with a 3D printed prototype. The main focus lays on the control action which has to guarantee the perfect ‘header and slaves’ logic. The test started by analysing the couple of back fins in order to evaluate the first feasible gain values and to understand how the system would react, including verifications of the whole connecting circuit (7.2V, 3A), maximum torque reached 2.5 Nm, maximum velocity reached 80 rpm. Only after this first check, tests were done for the whole system of fins. Fundamental parameters were varied in order to guarantee a parametric execution of the code and can be defined as:

- rpm of motors
- time lag between mechanisms
- control logics

Rpm value needs to be variable because of the different conditions in which the robot could be. For this reason, it has been installed an external button which allows the user to change at will the motor’s velocity. As said before, the motors’ velocity can vary from 30 to 80 rpm and any time the user clicks the button, it increases of 1 rpm. There is no limit in time within the user can click the button allowing to test different conditions in which the robot can proceed.

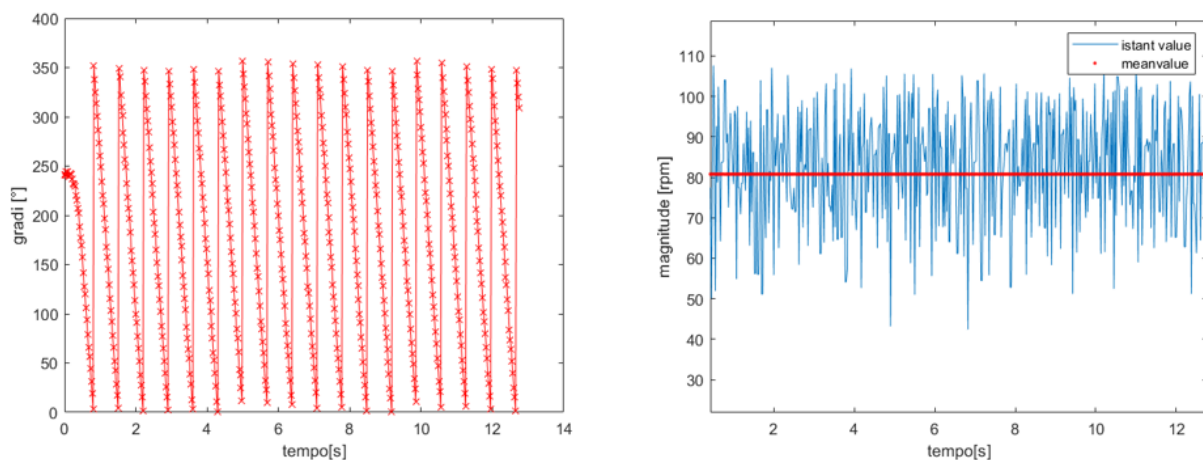


Figure 7.21: test of maximum motor’s rpm value, data processed with Matlab.

Time lag between mechanisms leads to considerations made previously in terms of energy consumption: forces increase when no lag is applied but when oscillation starts growing there is a notable decreasing in total energy consumption and forces lower their impact. As it has been done for the rpm values, an external button has been installed on the robot with which the user can vary the time lag value at will. Here also there is no limit in time within the button can be clicked allowing to test different conditions.

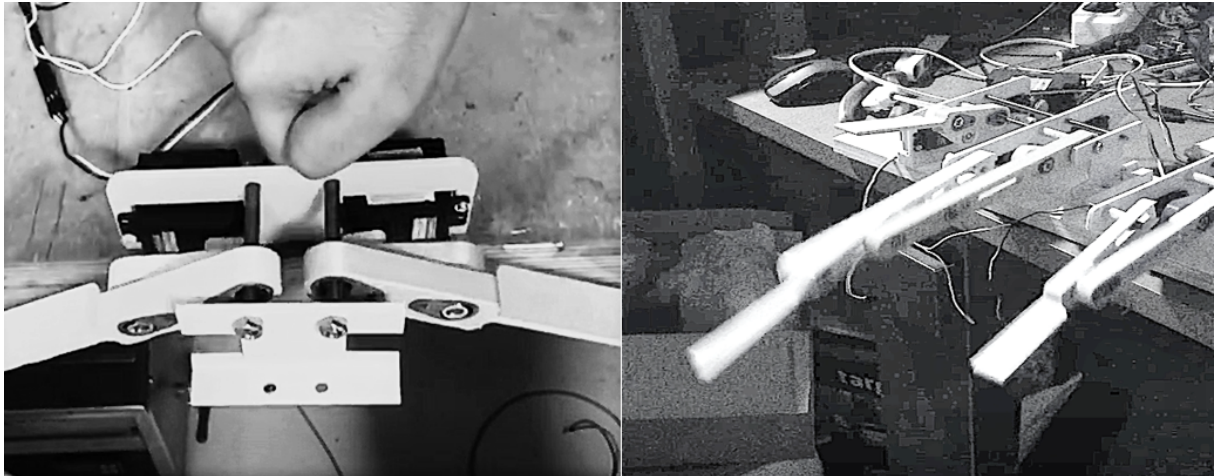


Figure 7.22: Control testing of the header and slave logic starting from the back ending up with the sinusoidal movement.

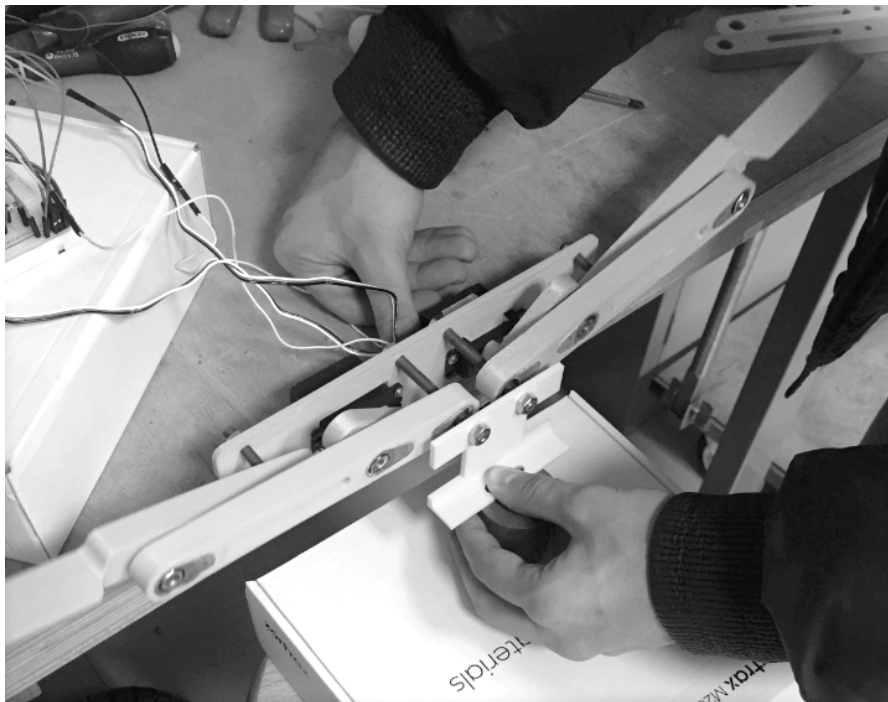


Figure 7.23: control testing of the header and slave logic for front fins couple.

Control logics have been divided into the four motions executable by the code: forward, backward, right turns and left turns were implemented and the user can move the robot in all the four directions with a joystick. Data regarding these parameters were extracted through the Arduino Serial Monitor. This monitor allows the user to keep trace instantaneously of the whole simulation parameters and their variations in time. At this point, the whole system of fins was mounted and the logic that has been used for the couple of fins was applied to six motors. Forward movement, backward movement and turns were verified in the aqueous ambient. Parameters are those of above i.e. variable rpms from 30 to 60. The torque was set at maximum 2Nm per motor. Time lag was varied from 0s to 0.2s shift between each motor. Battery delivers 7.2V and 3A.

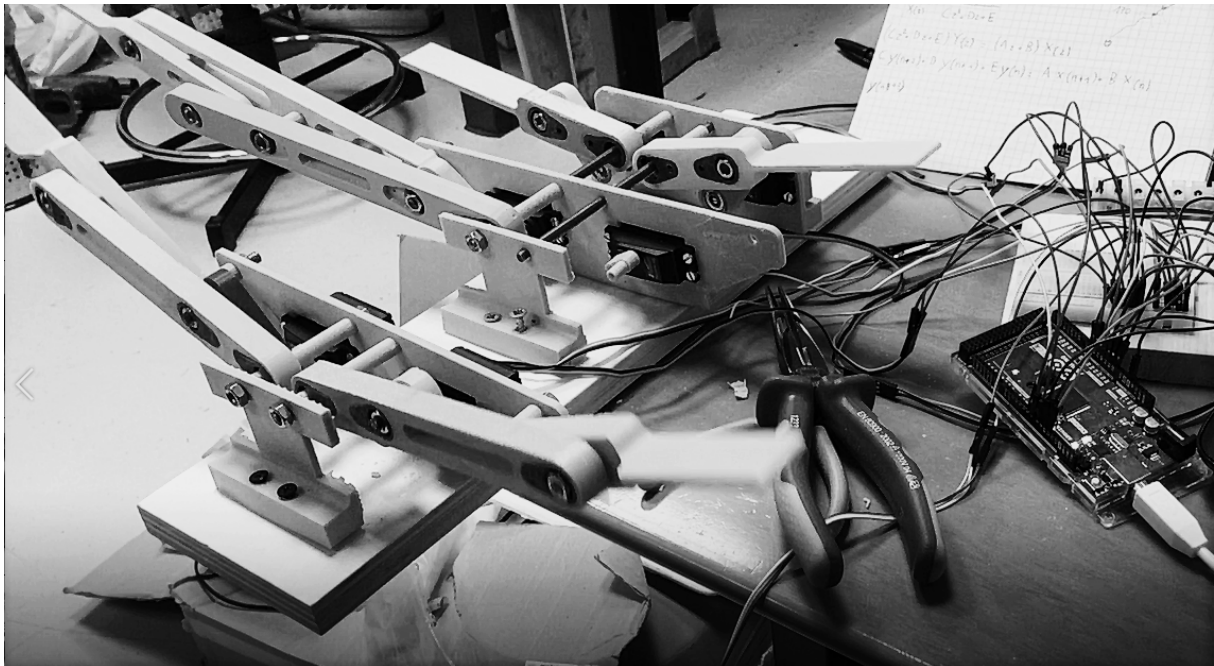


Figure 7.24: control testing of the header and slave logic for the whole system.

Last test was done in a tray full of water. The coating was made with plastic material welded in the appropriate shape. Front and central fins were tested for 5 min at rpm variable from 30 to 60. The moving mechanisms justify calculations made during the research. During these tests the fin moved smoothly in water and the torque provided by the motors resulted to be sufficient. Back fin was excluded because it was difficult to keep the total system sealed without a proper coating, and also because, as fig 5.21 suggests, it

gives a very low contribution in terms of torque. under-water test was a first step in order to start with future experiments. the control and the parametric process were of fundamental importance in order to guarantee the robot to proceed in the marine environment without difficulty, thus being able to deliver the torque necessary to move in the water. A total coverage of the robot will certainly allows the verification of what has been studied also in the marine environment with consequent considerations on the development and optimization of what is the design obtained through this work, getting closer to what will be the real robot in which design, control, 3D printing and feeding system, come together forming a robot that emulates the typical characteristics of bioinspired engineering. The advantages that can be drawn from these experiments are undoubtedly the great efficiency of the system, the simplicity with which it presents itself, and the control logic capable of intervening on the robot's motion thus making tracks or dives.

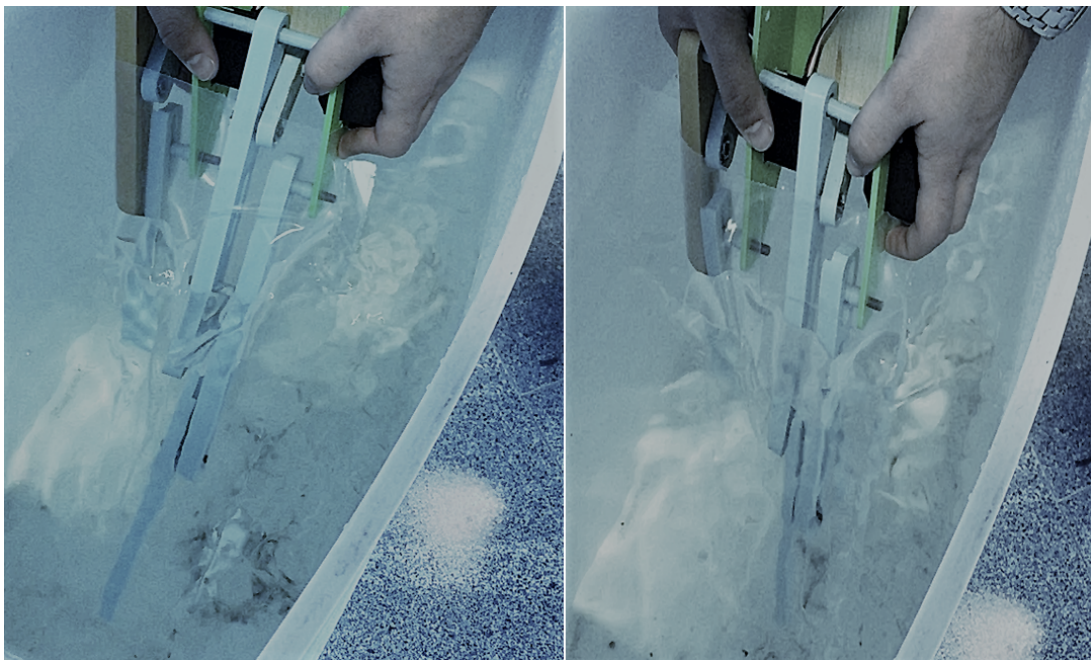


Figure 7.25: testing of the system in underwater condition to verify the maximum velocity delivered at maximum imposed torque.

Chapter 8

Conclusion

In this project has been presented how to develop a bio-inspired swimming robot from concept design to simulation and control. The choice to be inspired by a cownose-ray is due to the important qualities of this aquatic species which guarantees maneuverability, durability and high efficiency during motion. Through simplifications and the optimization processes it was possible to reproduce at best a robot very similar to the biological system. The characteristics are summarized as follows:

- Multi-fin rays are utilized to drive the flexible pectoral fin and each fin ray is actuated by an individual sealed servo. The flapping amplitude, frequency and phase lag of fin rays and the pectoral fin on each side can be adjusted independently.
- A rigid central body is the seat of all sensitive components such as motors and the electrical circuit
- An outer flexible body is poured considering the structure of the cow-nosed ray and the assembly demands.

In this way the pectoral fins can adapt to the complex under-water environment with multiplex deformation. A design check was carried out through various simulations. The 3D CAD was imported into Simulink and by assigning a rotation to the motors, the movement of the mechanisms and their phase shift were verified. The interactions of the body with the fluid were obtained with the CFD by imposing the constant movement at $1 \frac{m}{s}$. The results obtained thanks to the CFD and exploited for the simulation with Simulink have confirmed the starting hypotheses and the advantages extrapolated from

the analysis of the biological system.

The data obtained from the CFD show quite limited magnitude of forces compared to swinging plate thanks to the wavenumber of the chordwise kinematic wave. The dynamic simulation has also shown very limited values of torque and power consumption.

The control algorithm for the principal gaits of the fin have been implemented and tested. The tests performed are only preliminary because the robot was not fully submerged, but the fin managed to move a great amount of water, despite the low torque available and the small power consumed. In addition, the tests made are also influenced by the return of the wave, due to the restricted space, so the wave moved by the fin, reaching the walls of the tray returned to the fin causing an increase in forces. Although bio-inspired systems will never replace completely the traditional AUV, the results show that bio-inspired engineering allows to take advantage of all the benefits of a biological system and depending on the type of task to be performed, it is possible to choose the most suitable biologic system. In the case of the project in question the analysis confirmed the good hydrodynamics performances that the diamond shape of the cownose ray, similar to an airfoil, confers to the system, guaranteeing very low drag force. This shows the validity of the simulations carried out and it confirms that the motion of the manta ray has a high efficiency and durability also shown by the biological system during long migrations. Future works may allow to improve and optimize the control logics and verify the data also experimentally with, for example, tests in water or in a wind tunnel. Pressure sensors could be added in order to better evaluate the response of the system to external environment and to confirm the software data. It also possible to introduce an IMU for balance control and depth control or many other devices depending on the type of task to be performed. A camera could be useful for scanning environments and an infrared system could prevent from accidents in the path. Finally the coating needs to be builtd with some type of water-proof material and welded around. These obvious advantages of fish propelled by oscillating paired pectoral fins have attracted researchers worldwide to consider this kind of fish as the ideal nature sample to design a bionic fish overcoming all those limits that characterize a traditional AUV.

Bibliography

- [Albert, 2001a] Albert, J. S. (2001a). Species diversity and phylogenetic systematics of american knifefishes (gymnotiformes, teleostei).
- [Albert, 2001b] Albert, J. S. (2001b). Species diversity and phylogenetic systematics of american knifefishes (gymnotiformes, teleostei).
- [Allen et al., 2000] Allen, B., Vorus, W. S., and Prestero, T. (2000). Propulsion system performance enhancements on remus auvs. In *OCEANS 2000 MTS/IEEE Conference and Exhibition. Conference Proceedings (Cat. No. 00CH37158)*, volume 3, pages 1869–1873. IEEE.
- [Anderson et al., 2001] Anderson, E. J., McGillis, W. R., and Grosenbaugh, M. A. (2001). The boundary layer of swimming fish. *Journal of Experimental Biology*, 204(1):81–102.
- [Ayers et al.,] Ayers, J., Wilbur, C., and Olcott, C. Lamprey robots. presented at. In *Proc. Int. Symp. Aqua Biomechanisms*.
- [Bale et al., 2014] Bale, R., Hao, M., Bhalla, A. P. S., and Patankar, N. A. (2014). Energy efficiency and allometry of movement of swimming and flying animals. *Proceedings of the National Academy of Sciences*, 111(21):7517–7521.
- [Barrett et al., 1999] Barrett, D., Triantafyllou, M., Yue, D., Grosenbaugh, M., and Wolfgang, M. (1999). Drag reduction in fish-like locomotion. *Journal of Fluid Mechanics*, 392:183–212.
- [Blidberg, 2001] Blidberg, D. R. (2001). The development of autonomous underwater vehicles (auv); a brief summary. In *Ieee Icara*, volume 4, page 1.

- [Bose and Lien, 1989] Bose, N. and Lien, J. (1989). Propulsion of a fin whale (balenoptera physalus): why the fin whale is a fast swimmer. *Proceedings of the Royal Society of London. B. Biological Sciences*, 237(1287):175–200.
- [Bradley et al., 2001] Bradley, A. M., Feezor, M. D., Singh, H., and Sorrell, F. Y. (2001). Power systems for autonomous underwater vehicles. *IEEE Journal of oceanic Engineering*, 26(4):526–538.
- [Brandt and Selig, 2011] Brandt, J. and Selig, M. (2011). Propeller performance data at low reynolds numbers. In *49th AIAA Aerospace Sciences Meeting including the New Horizons Forum and Aerospace Exposition*, page 1255.
- [Breder, 1926] Breder, C. M. (1926). The locomotion of fishes. *Zoologica : scientific contributions of the New York Zoological Society.*, 4:159–297.
- [Clark and Smits, 2006] Clark, R. P. and Smits, A. J. (2006). Thrust production and wake structure of a batoid-inspired oscillating fin. *Journal of fluid mechanics*, 562:415–429.
- [Daniel, 1984] Daniel, T. L. (1984). Unsteady aspects of aquatic locomotion. *American Zoologist*, 24(1):121–134.
- [Drucker and Lauder, 1999] Drucker, E. G. and Lauder, G. V. (1999). Locomotor forces on a swimming fish: three-dimensional vortex wake dynamics quantified using digital particle image velocimetry. *Journal of Experimental Biology*, 202(18):2393–2412.
- [Du et al., 2015] Du, R., Li, Z., Youcef-Toumi, K., and y Alvarado, P. V. (2015). *Robot fish: bio-inspired fishlike underwater robots*. Springer.
- [Fei et al., 2011] Fei, S., Changming, W., Zhiqiang, C., De, X., Junzhi, Y., Chao, Z., et al. (2011). Implementation of a multi-link robotic dolphin with two 3-dof flippers.
- [Fish et al., 2018] Fish, F. E., Kolpas, A., Crossett, A., Dudas, M. A., Moored, K. W., and Bart-Smith, H. (2018). Kinematics of swimming of the manta ray: three-dimensional analysis of open-water maneuverability. *Journal of Experimental Biology*, 221(6).
- [Fontanella et al., 2013] Fontanella, J. E., Fish, F. E., Barchi, E. I., Campbell-Malone, R., Nichols, R. H., DiNenno, N. K., and Beneski, J. T. (2013). Two-and three-dimensional

- geometries of batoids in relation to locomotor mode. *Journal of experimental marine biology and ecology*, 446:273–281.
- [Gao et al., 2007] Gao, J., Bi, S., Xu, Y., and Liu, C. (2007). Development and design of a robotic manta ray featuring flexible pectoral fins. In *2007 IEEE International Conference on Robotics and Biomimetics (ROBIO)*, pages 519–523. IEEE.
- [Heine, 1993a] Heine, C. E. (1993a). Mechanics of flapping fin locomotion in the cownose ray, *rhinoptera bonasus* (elasmobranchii: Myliobatidae).
- [Heine, 1993b] Heine, C. E. (1993b). Mechanics of flapping fin locomotion in the cownose ray, *rhinoptera bonasus* (elasmobranchii: Myliobatidae).
- [Heusner, 1985] Heusner, A. A. (1985). Body size and energy metabolism. *Annual Review of Nutrition*, 5(1):267–293. PMID: 3896270.
- [Hu et al., 2006] Hu, H., Liu, J., Dukes, I., and Francis, G. (2006). Design of 3d swim patterns for autonomous robotic fish. In *2006 IEEE/RSJ International Conference on Intelligent Robots and Systems*, pages 2406–2411.
- [HüMMA, 1997a] HüMMA, K. (1997a). Biology of the manta ray, *manta birostris walbaum*, in the indo-pacific. *ishConferenCe*, page 209.
- [HüMMA, 1997b] HüMMA, K. (1997b). Biology of the manta ray, *manta birostris walbaum*, in the indo-pacific. *ishConferenCe*, page 209.
- [Katzschmann et al., 2016] Katzschmann, R. K., Marchese, A. D., and Rus, D. (2016). Hydraulic autonomous soft robotic fish for 3d swimming. In *Experimental Robotics*, pages 405–420. Springer.
- [Lauder and Madden, 2007] Lauder, G. V. and Madden, P. G. (2007). Fish locomotion: kinematics and hydrodynamics of flexible foil-like fins. *Experiments in Fluids*, 43(5):641–653.
- [Leonard et al., 1998] Leonard, J. J., Bennett, A. A., Smith, C. M., Jacob, H., and Feder, S. (1998). Autonomous underwater vehicle navigation. In *MIT Marine Robotics Laboratory Technical Memorandum*.

- [Lighthill, 1970] Lighthill, M. J. (1970). Aquatic animal propulsion of high hydromechanical efficiency. *Journal of Fluid Mechanics*, 44(2):265–301.
- [Liljebäck et al., 2014] Liljebäck, P., Stavadahl, Ø., Pettersen, K. Y., and Gravdahl, J. T. (2014). Mamba-a waterproof snake robot with tactile sensing. In *2014 IEEE/RSJ International Conference on Intelligent Robots and Systems*, pages 294–301. IEEE.
- [Lindsey, 1978] Lindsey, C. C. (1978). 1 - form, function, and locomotory habits in fish.
- [Low, 2011] Low, K. (2011). Current and future trends of biologically inspired underwater vehicles. In *2011 Defense Science Research Conference and Expo (DSR)*, pages 1–8. IEEE.
- [Low et al., 2011] Low, K., Zhou, C., Seet, G., Bi, S., and Cai, Y. (2011). Improvement and testing of a robotic manta ray (roman-iii). In *2011 IEEE International Conference on Robotics and Biomimetics*, pages 1730–1735. IEEE.
- [Majeed and Ali, 2016] Majeed, A. and Ali, A. (2016). Design and implementation of swimming robot based on carp fish biomimetic. pages 1–6.
- [McKenzie et al., 2007a] McKenzie, D., Hale, M., and Domenici, P. (2007a). Locomotion in primitive fishes. *Fish Physiology*, 26:319–380.
- [McKenzie et al., 2007b] McKenzie, D., Hale, M., and Domenici, P. (2007b). Locomotion in primitive fishes. *Fish Physiology*, 26:319–380.
- [Moored et al., 2011] Moored, K. W., Fish, F. E., Kemp, T. H., and Bart-Smith, H. (2011). Batoid fishes: inspiration for the next generation of underwater robots. *Marine Technology Society Journal*, 45(4):99–109.
- [Murphy and Haroutunian, 2011] Murphy, A. J. and Haroutunian, M. (2011). Using bio-inspiration to improve capabilities of underwater vehicles. In *17th International Symposium on Unmanned Untethered Submersible Technology (UUST)*, pages 20–31. Newcastle University.
- [Nesteruk et al., 2014] Nesteruk, I., Passoni, G., and Redaelli, A. (2014). Shape of aquatic animals and their swimming efficiency. *Journal of Marine Biology*, 2014.

- [Niu et al., 2012] Niu, C., Zhang, L., Bi, S., and Cai, Y. (2012). Development and depth control of a robotic fish mimicking cownose ray. In *2012 IEEE International Conference on Robotics and Biomimetics (ROBIO)*, pages 814–818. IEEE.
- [Ohlberger et al., 2006] Ohlberger, J., Staaks, G., and Hölker, F. (2006). Swimming efficiency and the influence of morphology on swimming costs in fishes. *Journal of Comparative Physiology B*, 176(1):17–25.
- [Parson et al., 2011] Parson, J. M., Fish, F. E., and Nicastro, A. J. (2011). Turning performance of batoids: limitations of a rigid body. *Journal of experimental marine biology and ecology*, 402(1-2):12–18.
- [Pettersson and Hedenström, 2000] Pettersson, L. B. and Hedenström, A. (2000). Energetics, cost reduction and functional consequences of fish morphology. *Proceedings of the Royal Society of London. Series B: Biological Sciences*, 267(1445):759–764.
- [Phillips et al., 2012a] Phillips, A., Haroutunian, M., Man, S., Murphy, A., Boyd, S., Blake, J., and Griffiths, G. (2012a). Nature in engineering for monitoring the oceans: Comparison of the energetic costs of marine animals and auvs.
- [Phillips et al., 2012b] Phillips, A., Haroutunian, M., Man, S., Murphy, A., Boyd, S., Blake, J., and Griffiths, G. (2012b). Nature in engineering for monitoring the oceans: Comparison of the energetic costs of marine animals and auvs.
- [Phillips et al., 2012c] Phillips, A., Haroutunian, M., Man, S., Murphy, A., Boyd, S., Blake, J., and Griffiths, G. (2012c). Nature in engineering for monitoring the oceans: Comparison of the energetic costs of marine animals and auvs.
- [Rosen and Trites, 2002] Rosen, D. A. and Trites, A. W. (2002). Cost of transport in steller sea lions, *eumetopias jubatus*. *Marine Mammal Science*, 18(2):513–524.
- [Rosenberger, 2001a] Rosenberger, L. J. (2001a). Pectoral fin locomotion in batoid fishes: undulation versus oscillation. *Journal of Experimental Biology*, 204(2):379–394.
- [Rosenberger, 2001b] Rosenberger, L. J. (2001b). Pectoral fin locomotion in batoid fishes: undulation versus oscillation. *Journal of Experimental Biology*, 204(2):379–394.

- [Rosenberger and Westneat, 1999] Rosenberger, L. J. and Westneat, M. W. (1999). Functional morphology of undulatory pectoral fin locomotion in the stingray *taeniura lymma* (chondrichthyes: Dasyatidae). *Journal of Experimental Biology*, 202(24):3523–3539.
- [Salazar et al., 2018a] Salazar, R., Fuentes, V., and Abdelkefi, A. (2018a). Classification of biological and bioinspired aquatic systems: A review. *Ocean Engineering*, 148:75–114.
- [Salazar et al., 2018b] Salazar, R., Fuentes, V., and Abdelkefi, A. (2018b). Classification of biological and bioinspired aquatic systems: A review. *Ocean Engineering*, 148:75–114.
- [Sfakiotakis et al., 1999] Sfakiotakis, M., Lane, D. M., and Davies, J. (1999). Review of fish swimming modes for aquatic locomotion.
- [Smallwood and Whitcomb, 2004] Smallwood, D. A. and Whitcomb, L. L. (2004). Model-based dynamic positioning of underwater robotic vehicles: theory and experiment. *IEEE Journal of Oceanic Engineering*, 29(1):169–186.
- [Stevens et al., 2018] Stevens, G., Fernando, D., and Di Sciara, G. N. (2018). *Guide to the Manta and Devil Rays of the World*. Princeton University Press.
- [Tolkoff, 1999] Tolkoff, S. W. (1999). *Robotics and power measurements of the RoboTuna*. PhD thesis, Massachusetts Institute of Technology.
- [Tucker et al., 1970] Tucker, V. A. et al. (1970). Energetic cost of locomotion in animals. *Comparative Biochemistry and Physiology*, 34:841–846.
- [Videler and Nolet, 1990] Videler, J. and Nolet, B. (1990). Costs of swimming measured at optimum speed: scale effects, differences between swimming styles, taxonomic groups and submerged and surface swimming. *Comparative biochemistry and physiology. A, Comparative physiology*, 97(2):91–99.
- [Videler, 1993] Videler, J. J. (1993). *Fish swimming*, volume 10. Springer Science & Business Media.
- [Vogel, 1994] Vogel, S. (1994). *Life in moving fluids: the physical biology of flow*. Princeton University Press.

- [Webb, 1984] Webb, P. W. (1984). Form and function in fish swimming. *Scientific American*, 251(1):72–83.
- [Webb, 1988a] Webb, P. W. (1988a). Simple physical principles and vertebrate aquatic locomotion. *American zoologist*, 28(2):709–725.
- [Webb, 1988b] Webb, P. W. (1988b). Simple physical principles and vertebrate aquatic locomotion. *American zoologist*, 28(2):709–725.
- [Webb, 1994] Webb, P. W. (1994). The biology of fish swimming. *Mechanics and physiology of animal swimming*, 4562.
- [Webb and Weihs, 1983] Webb, P. W. and Weihs, D. (1983). *Fish biomechanics*. Praeger Publishers.
- [Wynn et al., 2014] Wynn, R. B., Huvenne, V. A., Le Bas, T. P., Murton, B. J., Connelly, D. P., Bett, B. J., Ruhl, H. A., Morris, K. J., Peakall, J., Parsons, D. R., et al. (2014). Autonomous underwater vehicles (auvs): Their past, present and future contributions to the advancement of marine geoscience. *Marine Geology*, 352:451–468.
- [Yu et al., 2009] Yu, S., Ma, S., Li, B., and Wang, Y. (2009). An amphibious snake-like robot: Design and motion experiments on ground and in water. In *2009 International Conference on Information and Automation*, pages 500–505.
- [Zhang et al., 2016] Zhang, S., Qian, Y., Liao, P., Qin, F., and Yang, J. (2016). Design and control of an agile robotic fish with integrative biomimetic mechanisms. *IEEE/ASME Transactions on Mechatronics*, 21(4):1846–1857.